Politecnico di Milano

Graphene Oxide as a cement reinforcing additive

Preliminary study

Candidate

Ambra Romani
ID number
804041

Supervisors

Prof. Paolo Gronchi
Dott. Luigi Brambilla
Ing. Marco Goisis

Ringraziamenti

Desidero ringraziare il Professor Paolo Gronchi, il quale mi ha proposto questo lavoro di tesi mettendomi a disposizione le sue conoscenze e competenze. Una persona che ha saputo incoraggiarmi, motivarmi e sostenermi, consentendomi di lavorare sempre nelle migliori condizioni possibili.

Grazie al Dottor Luigi Brambilla e all'Ingegner Marco Goisis, che hanno saputo consigliarmi e indicarmi la giusta direzione da intraprendere durante il percorso di ricerca e di stesura dell'elaborato finale.

Ringrazio la mia famiglia, che mi ha sostenuto durante tutti i miei studi universitari, ed in particolare Mattia, che mi ha accompagnato in questi anni aiutandomi e supportandomi come solo un fratello può fare.

Contents

List of Figures

List of Tables

Abstract

This work aims to the synthesis of graphene oxide and to investigate its effect on the mechanical resistance of the cement base composites.

Starting from graphite powder we performed a chemical oxidation using sulfuric acid (H_2SO_4), sodium nitrate ($NaNO_3$) and potassium permanganate ($KMnO_4$) following the Hummer's method. The graphene oxide sludge has been washed several times and then sonicated to ensure the complete exfoliation of the platelets. The *GO* has been dried in the oven for 24 hours at 70 $°C$ obtaining black films used for the characterization and for the synthesis of the chemically modified graphene oxide with *Jeffamine M600*. The *GO* has been also subjected to different thermal treatment to observe its thermal stability with increasing temperature. The functionalization of the *GO* with the *Jeffamine M600* (polyetheramine), has been performed using dimethyl sulfoxide (*DMSO*) as solvent, dimethylaminopyridine (*DMAP*) as catalyst and maintaining the solution under stirring and nitrogen. After the purification stage the *GO-Jeffamine M600* has been dried in over for 24 hours at 70 $°C$. The *GO* and the *GO-Jeffamine M600* samples were characterized with several techniques:

- Infrared and Raman spectroscopy: vibrational spectroscopy that provides information at molecular level of the functional groups that are present in the samples;

- Inductively Coupled Plasma Optical Emission Spectrometry and Elemental Analyses: determines the concentration of element present in the analyzed samples;

- X-Ray Diffraction Analyses: gives information about the crystallographic structure of the specimens;

- Thermogravimetric Analyses: changes of physical and chemical properties of the materials are measured as function of the increasing temperature;

- Transmission Electron Microscopy: an image of the samples is formed due to the interaction of the electrons transmitted through the specimens;

- Selected Area Electron Diffraction: provides information about the crystallographic structure.

The preparations of the mortar composites specimens was carried out in a controlled environment, with constant relative humidity and temperature ($20 \pm 2°C$). The specimens was prepared by mixing cement, standard sand, water, superplasticizer (*PCs*) and different amount of *GO*. The mortars samples were tested for the compression and flexural resistance and characterized using:

- Scanning Electron Microscopy: gives information about the morphology of the hydrated crystals;

- Energy Dispersive Spectroscopy: provides the distribution of elements present in the samples.

Sommario

Lo scopo di questo lavoro di tesi è la sintesi di grafene ossido e l'osservazione della sua efficacia come additivo rinforzante in materiali cementizi.

Il grafene ossido è stato sintetizzato attraverso ossidazione chimica di grafite in polvere in presenza di acido solforico (H_2SO_4), nitrato di sodio ($NaNO_3$) e permanganato di potassio ($KMnO_4$) seguendo la procedura messa a punto da Hummer. Il grafene ossido (*GO*), così sintetizzato, è stato lavato diverse volte e trattato con ultrasuoni per assicurarne la completa esfoliazione. Parte della soluzione acquosa contenente il *GO* è stata essiccata in forno per 24 ore a 70 °C, ottenendo dei film di colore nero utilizzati successivamente per la caratterizzazione del *GO* stesso e per la sintesi dell'ossido di grafene chimicamente modificato con una polieterammina (*Jeffammine M600*). Abbiamo sottoposto il *GO* a diversi trattamenti termici per determinare la sua stabilità termica e quella dei gruppi funzionali formatisi dopo l'ossidazione. Il grafene ossido chimicamente modificato è stato ottenuto attraverso una reazione di funzionalizzazione tra il *GO* e la *Jeffammine M600* in presenza di dimetil solfossido (*DMSO*) come solvente e di dimetil amminopiridina (*DMAP*) come catalizzatore. La soluzione è stata mantenuta in agitazione e in atmosfera di azoto per tutto la durata della reazione. Il prodotto ottenuto, *GO-Jeffamine M600*, è stato sottoposto ad una fase di purificazione per poi essere essiccato in forno a 70 °C per 24 ore. Il *GO* ed il *GO-Jeffammine M600* sono stati caratterizzati utilizzando diverse tecniche:

- Spettroscopia Infrarossa e Raman: spettroscopie vibrazionali che forniscono informazioni a livello molecolare dei gruppi funzionali presenti;

- Spettrometria ad Emissione Ottica e Analisi Elementare: utilizzata per determinare la quantità relativa degli elementi presenti nei campioni;

- Diffrattometria a raggi-X: usata al fine di ottenere informazioni sulla struttura cristallografica del materiale;

- Analisi Termogravimetriche: forniscono le variazioni delle proprietà fisiche e chimiche dei campioni in funzione della temperatura;

- Microscopia Elettronica a Trasmissione: permette di ottenere immagini dei provini grazie all'interazione tra gli elettroni e il campione;

- Diffrazione Elettronica: fornisce informazioni sulla struttura cristallografica dei materiali.

La preparazione dei campioni di malta additivata con il *GO* è stata effettuata in ambiente controllato, con umidità relativa e temperatura costante ($20 \pm 2\,^{\circ}C$). I provini sono stati confezionati miscelando il cemento con sabbia, acqua, super fluidificante (*PCs*) e diverse quantità di *GO* per poi essere testati in compressione, in flessione ed analizzati utilizzando:

- Microscopia Elettronica a Scansione: al fine di ottenere informazioni sulla morfologia dei cristalli di cemento;

- Spettroscopia a Dispersione di Energia: per rilevare informazioni sulla distribuzione degli elementi presenti nei campioni.

Introduction

Graphene Oxide (*GO*) has attracted great interest in the scientific word, due to its application as precursor for graphene production and to the presence of different polar groups, which can be modified, allowing the possibility to control the properties of the materials. In fact, the *GO* can be used as raw materials for the syntheses of nanoparticles-graphene composite and several type of polymers-graphene composites using for example epoxy, polystyrene, polyaniline, polyvinyl alcohol, polyurethane. Nowadays, the *GO* is also studied as reinforcing additive for the cement composites (cement paste, mortar and concrete) and many authors reports promising result about it. In particular, in the latest years, in literature appears studies that shows increasing in the compressive strength greater of the 10% and in the flexural strength of 40%, which are, very significant and attired the interest of the cement industries. The mechanism that allow this impressive improvement in the mechanical properties has not been fully comprehended and described. Shengua et al. [1] proposed a regulatory mechanism of *GO* on cement hydration products: they supposed that the grafene oxide induce the formation of more regular crystal structure (flower and polyhedron-like) due to the presence of the oxygen functionalities on the *GO*, that act as nucleation sites for the hydration crystals. The procedure used in this research is not fully described and they do not provide a specific methodology for the study of this problem.

   In this thesis, work the graphene oxide has been synthesized starting from graphite powder and it will be characterized using several techniques: Infrared and Raman Spectroscopy, Inductively Coupled Plasma Optical Emission Spectrometry, Thermogravimetric, Elemental, X-Ray diffraction analyses, Transmission Electron Microscopy and Selective Area Electron

Diffraction technique. The graphene oxide will be used in different concentration as reinforcing additive in mortar samples which will be mechanically characterized (compression and flexural resistance), observed with a Scanning Electron Microscope and analyzed with Energy Dispersive Spectroscopy after 3, 7 and 28 days of curing. The dispersion of the *GO* in cement is a difficult procedure and its addition on the paste determines a decrease in the workability: we will try to functionalize the graphene oxide with a molecule that act as plasticizer for cement base composites. We choose the *Jeffamine M600* and to try to graft it to the graphene oxide carbon backbone with the formation of an amidic bond between the carboxyl groups of the *GO* and the $-NH_2$ terminal of the *Jeffamine*, producing a Chemically Modified Graphene Oxide (*CMGO*). The *CMGO* will be deeply characterized with thermogravimetric analyses and with Infrared spectroscopy to understand if the amidic bond between the *GO* and the *Jeffamine M600* is formed.

This work is a preliminary study whose aim is to investigate: the more suitable materials and procedure for the synthesis of the *GO* and for the preparation of cement carbon composites. Although we intend to identify the best techniques for the *GO* characterization and to understand the mechanism that produce the improvement of the performance of the cement base materials.

This thesis is organized as follows:

Chapter 1 reviews the properties of cement, its weakest points and the current method used nowadays to improve the mechanical properties of concrete;

Chapter 2 reviews the structure and properties of graphene oxide and its use as reinforcing materials in cement matrix composites materials;

Chapter 3 describes the syntheses of graphene oxide and of the chemically modified *GO* together with the preparation of the cement base composites. All the used instrumentations for the characterization are explained in details;

Chapter 4 reports all the obtained results on the graphene oxide, the chemically modified *GO* (*GO-Jeffamine M600*) and the cement base composites;

Chapter 5 presents the conclusions, summarizing the main achievements and outlining possible future developments.

Chapter 1

Cement base composites

Cementitous materials are the most construction materials use word wide, especially the concrete which typically consist of Ordinary Portland Cement (*OPC*), sand, coarse aggregate, water and chemical admixture (accelerators, plasticizers, etc.). However, the major disadvantage of concrete is its brittle nature, which is mainly attributed to its porous structure causing a poor resistance to crack formation, low strain capacities, low bending and low tensile strength. Many attempts have been directed at enhancing the performance of cement based materials by manipulating the properties of cement composites with mineral admixtures (fly ash, silica fume, etc.), supplementary cementitous materials, macro reinforcement such as steel rebar or clay particles and micro reinforcement such as fibers (Fiber Reinforced Concrete, *FRC*). In the last years, the research is moving toward the nanoreinforcement that would delay the nucleation and growth of cracks on the nanoscale. In this Chapter, we will discuss recent studies in developing cement micro and nanocomposites after an introduction on the cement chemistry.

1.1   Cementitous materials

Cement is a binder: a fine powder that, when mixed with water, give rise to a plastic paste, in time sets and hardens, maintaining its dimension and shape. The ASTM C219-14a [2] standard define cementitious material as "inorganic material or a mixture of inorganic materials that sets and develops strength by chemical reaction with water by formation of hydrates

and that is capable of doing so underwater". The most important cement used nowadays is the Ordinary Portland Cement (*OPC*), which is used as a component in the production of mortar (a mixture of cement, sand and water) and of concrete, a combination of cement and an aggregate to form a strong building material whose microstructure is reported in Figure 1.1. Famous concrete structures include the Colosseum (Figure 1.2) and the Pantheon in Rome (Figure 1.3), which is the world's largest unreinforced concrete dome. Today, large concrete structures like dams are usually made with reinforced concrete.
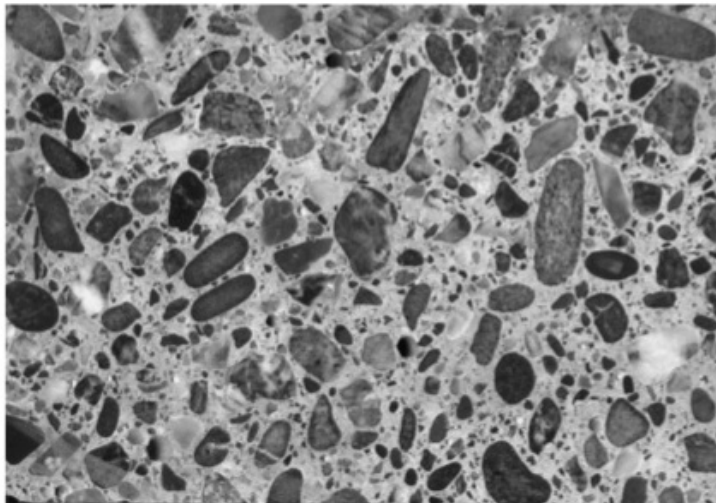
Figure 1.1. Concrete microstructure [3].

Figure 1.2. The Colosseum structure in Rome.
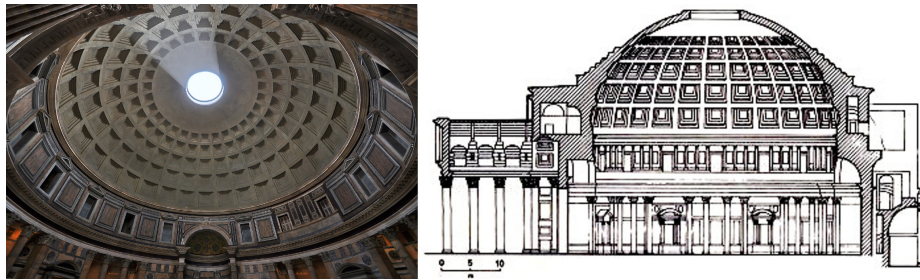
Figure 1.3. The Pantheon dome in Rome.

The *OPC* is define, by the same standard [2] as "hydraulic cement produced by pulverizing clinker, consisting essentially of crystalline hydraulic calcium silicates and usually containing one or more of the following: water, calcium sulfate, up to 5% limestone, and processing additions". The producing cycles of a Portland cement is characterized by different stages: first of all the grinding and mixing of the natural or artificial raw materials such as clay, limestone (a source of calcium) and other component added to control the content of different metal oxide in the mixture (bauxite, siliceous materials, iron oxide, etc.). Once obtained an homogeneous mixture, it is heated in a rotary kiln at high temperature (until $1450°C$) than cooled down obtaining the clinker (lumps or nodules of 3-25 *mm* diameter) which consist of various calcium silicate, calcium aluminate, calcium aluminoferrite and other metal oxide (*MgO, K_2O*, etc.) but in lower content. In Table 1.1 are reported all the different physical and chemical reaction that we can observed in the kiln. The next stage consist in the grinding of the clinker with a little amount of gypsum (5% maximum) as a source of sulfates and different other additives, obtaining a fine powder (90% in weight of the particles have a diameter between 2 and 90 *μm*). If now we add a suitable amount of water to this powder, we obtained the cement paste. Initially it result plastic and workable due to the presence of free water, but in time the hydration process take place, leading to the reduction of workability and to the formation of several hydration product with a complex chemistry and physical structure that nowadays is not totally be understood [4]. The hydration mechanism and the products obtained with this reaction are reported in detail in the next Paragraph.

Table 1.1. Principal chemical and physical reactions taking places in the kiln [4].

T(°C)	Reaction	Description
~ 500	$Al_2O_3 \cdot 2SiO_2 \cdot 2H_2O \longrightarrow Al_2O_3 + 2SiO_2 + 2H_2O$	Clay decomposition
$600 - 950$	$MgCO_3 \longrightarrow MgCO + CO_2$	Carbonate decomposition
	$CaCO_3 \longrightarrow CaO + CO_2$	
$600 - 1000$	$2CaO + SiO_2 \longrightarrow 2CaO \cdot SiO_2$	Reaction between the decomposition product
	$CaO + Al_2O_3 \longrightarrow CaO \cdot Al_2O_3$	
	$2CaO + Fe_2O_3 \longrightarrow 2CaO \cdot Fe_2O_3$	
$1000 - 1200$	$2CaO + CaO \cdot Al_2O_3 \longrightarrow 3CaO \cdot Al_2O_3$	Formation of C_3A and C_2S
	$2CaO + SiO_2 \longrightarrow 2CaO \cdot SiO_2$	
$1200 - 1250$	$2CaO + SiO_2 \longrightarrow 2CaO \cdot SiO_2$	Maximum concentration of C_2S
$1250 - 1450$	$CaO + 2CaO \cdot SiO_2 \longrightarrow 3CaO \cdot SiO_2$	Formation of the liquid phase and of C_3S
Cooling	$Liquidphase \longrightarrow 3CaO \cdot Al_2O_3 + 4CaO \cdot Al_2O_3 \cdot Fe_2O_3$	Formation of C_3A and C_{AF}

1.2 Hydration reaction and products

Cement is mainly constituted of silicates (tricalcium silicate C_3S and dicalcium silicate C_2S) and aluminates (tricalcium aluminate C_3A and tetracalcium aluminoferrite C_4AF), which undergoes hydration simultaneously but for sake of simplicity we will consider the two reaction separately. In Table 1.2 are reported the main constituent of the cement before hydration, so of the clinker [4], [5].

Table 1.2. Principal clinker constituent [4].

Constituents	Chemical formula	Notation	Name
Tricalcium silicate	$3CaO \cdot SiO_2$	C_3S	Alite
Dicalcium silicate	$2CaO \cdot SiO_2$	C_2S	Belite
Tricalcium aluminate	$3CaO \cdot Al_2O_3$	C_3A	Celite
Tetracalcium aluminoferrite	$3CaO \cdot Al_2O_3 \cdot Fe_2O_3$	C_4AF	//

The aluminates hydrates faster respect the silicates and are relevant for the setting and hardening process, but they do not contribute to the mechanical resistance. Instead, the silicates hydration mainly determine the final mechanical resistance of the cement, but does not have any influences on the setting process.

Consider the hydration reaction of the aluminates. The hydration of C_3A is immediate once added the water, it is highly exothermic and produce the same hydration crystal of the C_4AF. The reaction of C_3A with water is so fast that must be slowed down adding gypsum to the mixture: in contact with water it release sulfate ions ($SO_4^=$) and calcium ions (Ca^+) that react with the aluminates ions (Al_4O^-) to form a trisulfate named Ettringite ($3CaO \cdot Al_2O_3 \cdot 3CaSO_4 \cdot 32H_2O$) that tend to transform to the monosulfate form ($3CaO \cdot Al_2O_3 \cdot CaSO_4 \cdot 12H_2O$) [5]. The trisulfate is characterized by a needle-like structure, instead the monosulfate has a plate morphology (Figure 1.4). The Ettringite cover the cement grain that are reacting and slow down the reaction for some hours. The amount of gypsum needed depend on the content either of C_3A and of the silicates: in fact, the sulfate not only delay the hydration of the aluminates but also accelerate the hydration of silicates. The hydration of the C_4AF gives the

same hydrated products (Ettringite) but is not as fast as for the C_3A [3].
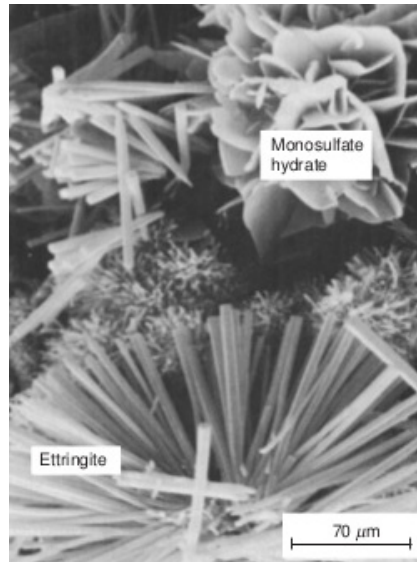
Figure 1.4. *SEM* micrograph of Ettringite [3].

Consider now the hydration of silicates. This reaction give rise to two different products: hexagonal crystals of calcium hydroxide called Portlandite $(Ca(OH)_2)$ and a variety of calcium hydrate product structurally similar but with different composition (different proportion *Si/Ca* and bonded water) called gel *C-S-H* or cement gel. For a giver mass the C_2S produce a higher amount of gel *C-S-H* respect the C_3S, which hydration produce an higher amount of Portlandite, but both contribute to the total amount of Portlandite and of *C-S-H*. The Portlandite crystals are weak and subjected to fracture due to the weaker bond between the layers of its crystals. Otherwise, the *C-S-H* structure has not been fully resolved and there is still ongoing debate over its nanostructure. The comprehension of the structure of the *C-S-H* is fundamental because it represent the 80% of the final volume and the 50% of hardened mass and so, it is responsible of the mechanical resistance of the material. Some example of the models uses for the *C-S-H* will be provided later in the Paragraph 1.2.1. In Table 1.3 is reported a summary for the different hydration reaction and in Figure 1.5 the different hydration stages:

a) cement powder before adding the water;

b) just after the water adding a thin film of Ettringite is formed on the

surface of the cement particle delaying the hydration of the aluminates;

c) the delaying can last some hours but the film is then permeated by the water allowing the formation of the *C-S-H* and of the Portlandite;

d) the hydration continues with decreasing speed because the gel *C-S-H* hinders the diffusion of water toward the nucleus of the cement powder, which can remain not hydrated for years.

Table 1.3. Hydration reaction and products [4].

Clinker constituent	$\xrightarrow{reaction}$	Hydration products
C_2S	$\xrightarrow{fast}$	Gel C-S-H > Portlandite
C_3S	$\xrightarrow{slower}$	Gel C-S-H < Portlandite
C_3A and C_4AF	$\xrightarrow{fastest}$	Ettringite
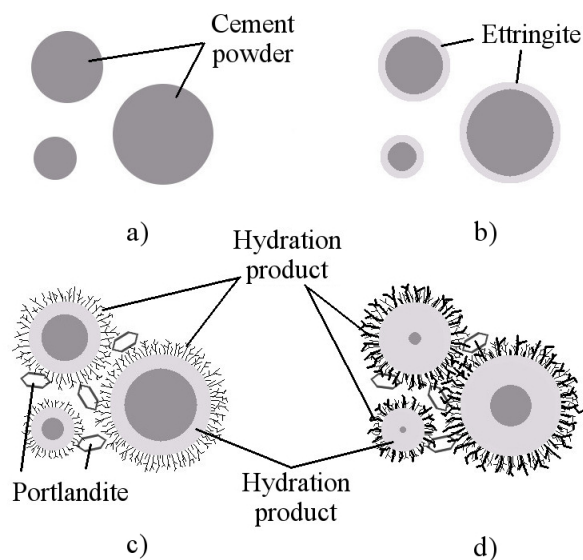
Figure 1.5. Different stages of hydration process [4].

1.2.1   Gel *C-S-H* nanostructure

Henri Le Chatelier [6] in the late 19th and early 20th centuries was one of the first that to try to explain experimentally what is produced during the hydration process of *OPC*. He argue that the hydrated crystals appears in the shape of elongated needles, which have the tendency to group themselves in spherolites. He although supposed that the entanglement of all these crystals is the only cause of the solidity of the mass, so the materials is held together by mechanical forces and not by anything of colloidal. In the 1946, in contrast with Le Chatelier, Powers and Brownyard [7] proposed one of the first physical models for the *C-S-H* structure describing it as a colloidal material held together mainly by van der Waals forces. The interlayer space within the *C-S-H* structure, was called gel porosity and they considered it accessible only by water molecules. Bernal and Taylor [8], in the same period (1952) found with X-Ray studies that the *C-S-H* was nearly amorphous and so the structure characterization was difficult. However, they consider that it was correlated to the *C-S-H* phases observed by Taylor (1950) [9] in dilute suspensions, called calcium silicate hydrates *(I)* and *(II)*, which had low and high *Ca/Si* ratios, respectively. Calcium silicate hydrate *(I)* had a layered structure and shown similarities to tobermorite ($Ca_5Si_6O_{16}(OH)_2 \cdot 4H_2O$), a rare and natural crystalline calcium silicate hydrate. The *C-S-H (II)* is characterized by elements of tobermorite-like structure intermixed with others of jennite-like structure, where the jennite ($Ca_9Si_6O_{18}(OH)_6 \cdot 8H_2O$) is another rare and natural mineral. The tobermorite structure was firstly described by Megaw and Kelsey in 1956 [10]: is a complex layered structure based on a calcium sheet flanked on each side by linear silicate chains of the dreierkette form (silicate chains kinked in such a way as to repeat at an interval of three tetrahedra). Two adjacent tetrahedra coordinate them self to the calcium ions of the layer, while the third bridges the two successive dimers. In Figure 1.6 are reported the schematic structure obtained by Richardson [11] of the tobermorite (Figure 1.6 a) and the jennite (Figure 1.6 b): paired and bridging tetrahedra are labelled as *P* and *B*, respectively.

In the 1968, Feldman and Sereda [12] proposed the well-known quasi-continuum model based on extensive experimental studies on hydrated cement systems. The main feature of this model is the layered nature of the

a) b)
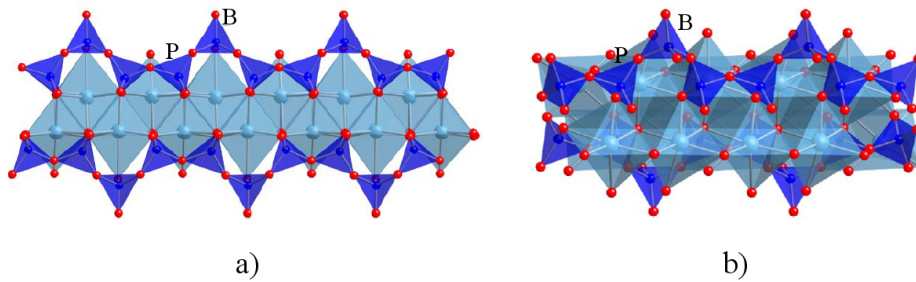
Figure 1.6. Structure of: a) tobermorite and b) jennite [11].

C-S-H which is describe as formed of several lamellae with a tobermorite like structure extremely thin (some nanometer) and long tens of hundreds of nanometers. In Figure 1.7 is reported the Feldman and Sereda model in which is indicated the interlayer and physically adsorbed water.
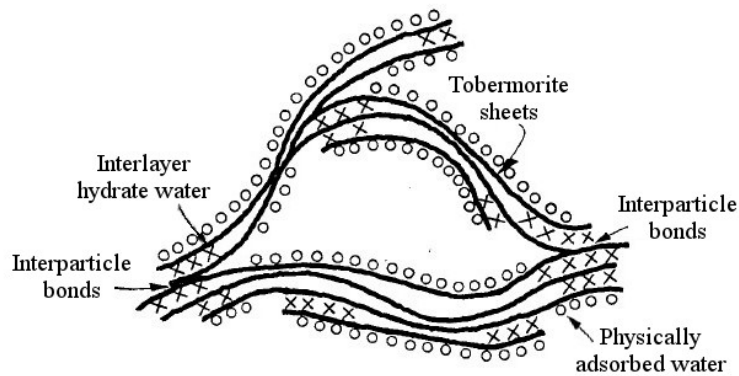
Figure 1.7. Feldman and Sereda model for the gel *C-S-H* structure [12].

Richardson in the 2000 [11], [13] discuss the applicability of the Taylor model for the nanostructure of *C-S-H* in real cement. It comprises a disordered network of semi-crystalline layers of calcium and oxygen atoms with silica tetrahedra attached and interspersed by further calcium ions. He although identifies two water environments: the interlayer water and water in nanoscopic pores between locally aggregated semi-crystalline layers. Also Bonaccorsi and Merlino [14] based their studies on Taylor's, but they focused on the structure of natural jennite because several data indicate that over a period of months and years, the jennite-type structures become increasingly dominant. In the 2000, starting from Powers and Brownyard work, Jegging [15] proposed a new colloidal model for the nanostructure

of hydrated cement paste, refine in a 2004 [16] and in the 2006 [17]. This model is essentially a hybrid between the Feldman-Sereda layered model and the colloidal Powers-Brownyard model: he consider the gel *C-S-H* as formed of colloidal particle, called globules with a characteristic length of at least 5 *nm*, till 30-60 *nm* with a layered substructure considered to be chemically similar to those found in natural minerals like tobermorite and jennite (Figure 1.8). The globules pack together in clusters with two possible packaging densities, termed high and low density *C-S-H*. Jegging also indicate three types of pores:

- intraglobular pores (*IGP*): voids within the globule referred;

- small gel pores (*SGP*): voids trapped between the globules with a diameter of 1-3 *nm*;

- large gel pores (*LGP*) or space created because of the overlap of globules (3-12 *nm* in diameter).
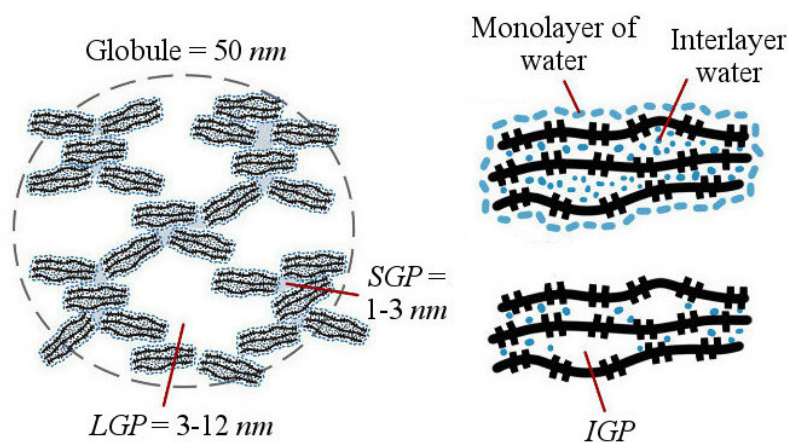
Figure 1.8. Jegging model for the *C-S-H* structure [17].

Nowadays several numerical model have been proposed but there is not a model that can described the whole structure and the nature of the *C-S-H*. All the theory and model proposed until now have something in common: they all supposed the presence of a porous structure with water that can fill these pores. This is going to be discuss in the next Paragraph.

1.3 Factors influencing the mechanical properties

The source of the mechanical properties of the concrete need to be research in the intrinsic porous microstructure of the hydrated cement paste and in the formation of an Interfacial Transition Zone (*ITZ*) between the paste and the coarse aggregates. Cement paste, as a porous material, has air and water permeable properties and this has not only a great influence on strength, but on durability to. Instead, the *ITZ* represent the so-called "weakest link of a chain", and has considered as the strength-limiting phase in concrete. This two factor will be discuss separately.

1.3.1 Pores, voids and water

In construction site, water is often added to the concrete mixture to increase the workability for easy casting, but concrete with added water shows segregation of aggregates and degradation of performance in both strength and durability. Hydration reaction in concrete with larger water content determines a formation of more pores in the cement paste, which lead to reduction of strength and resistance to deterioration. Indeed the main route into concrete for deteriorating agent (water, chlorine ions, carbon dioxide, etc.) is the pores and their connectivity, which are generated during the hydration process and strongly influenced by the amount of water added to the mixture. Many researches [18], [19] have been performed on the effects of the water-cement ratio (*w/c*) on the durability and porosity of cement, demonstrating that the durability, in term of chlorine diffusion, air permeability, saturation and moisture diffusion, decrease for higher *w/c*. The correlation between the strength and the porosity in a solid material, have been studied for a long time: we can in fact affirm, without any doubt that exyst a fundamental inverse relationship between the porosity and the mechanical strength [4]. In particular Powers [7] demonstrate that the compression strength (*R*) of cement paste can be express by this simple equation:

$$R = kx^3 = k\{1 - \frac{V_{pc}}{V_s + V_{pc}}\} \tag{1.1}$$

where V_s is the volume occupy by the solid and V_{pc} is the total volume of capillary pore which can be defined considering another Powers equation

(Eq. 1.2) reported below.

$$V_{pc} = V_{ac} + V_{vc} = \{w/c - 0,36h\} \tag{1.2}$$

In particular:

- V_{pc} is the volume of the capillary pores;

- V_{ac} is the water in the capillary pores;

- V_{vc} is the vacuum in the capillary pores;

- w/c is the water cement mass ratio;

- h is the hydration grade.

Considering this last equation, we can affirm that the volume of the capillary pores decrease with the increasing of the hydration grade (h) and with the decreasing of the water-cement ratio. This is confirmed by the Figure 1.9, in which is reported the effect of the w/c ratio and of the hydration grade on the penetration volume.
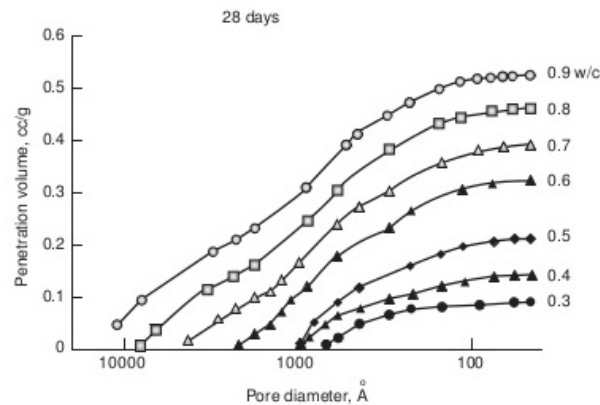
Figure 1.9. Effect of pore dimension on the penetration volume at different w/c ratio [4].

The effect of the w/c ratio on the compressive strength of the concrete, is easily visible considering the Figure 1.10: for a constant curing age, higher w/c means lower compressive strength. This is very evident for 28 days of curing [4].
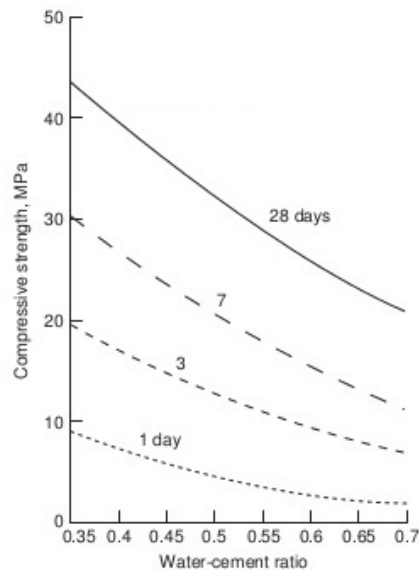
Figure 1.10. Effect of *w/c* over the compressive strength [4].

In Figure 1.11 we report the Feldmann and Sereda model for the *C-S-H* structure. Considering it, we can summarized all the different types of pores, voids and water present in the hydrate cement paste:

- capillary voids: they represent the space not filled by the solid component of the hydrated cement. In a well-hydrated paste (high hydration grade) the capillary voids may have diameter in between of 10 and 50 *nm*, but can reach 3-5 *μm* if the *w/c* is high. Capillary pores larger than 50 *nm* (macropores) are more influential in determining the strength and durability of the structure, whereas voids smaller than 50 *nm* (micropores) play an important role in drying shrinkage and creep;

- interstitial space in the *C-S-H*: voids between the different lamellae of the gel. The dimension of these voids is so small that are in the range of action of the van der Waals forces and the water that is absorbed in these pores (interlayer water) is held by hydrogen bonding. The removal of the interlayer water may contribute to drying shrinkage and creep;

- pores due to the incorporation of air with dimension of some *mm* due to the insufficient compaction or added intentionally with the some additives. Due to their size, can affect negatively the strength;

- adsorbed water on the solid surface of the hydrate product. The loss of adsorbed water is responsible for the shrinkage of the hydrate cement paste [3].
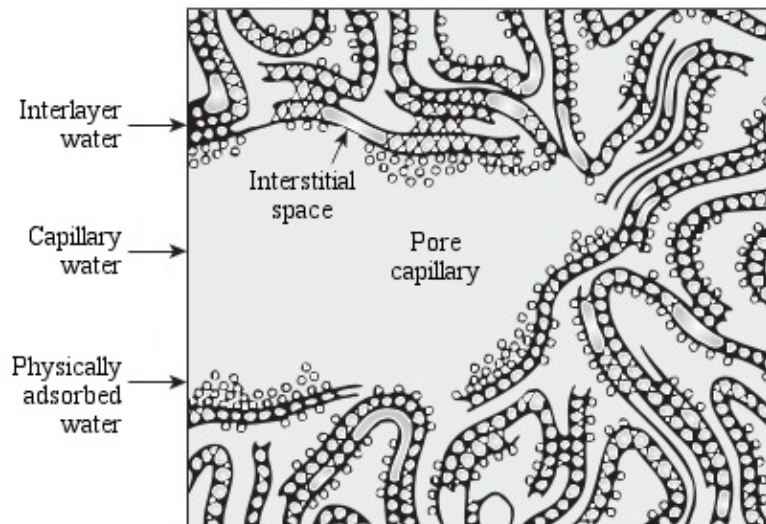
Figure 1.11. Feldman and Sereda model for the *C-S-H* structure [3].

1.3.2 Interfacial Transition Zone

The mechanical properties of concrete are influenced not only by the properties of individual constituents (the cement paste and the aggregate), but also by their contents, as well as their interaction and spatial configuration. This can be graphically illustrated by the comparison of the stress-strain curves for cement paste, aggregates and concrete under compression loading (Figure 1.12). Individually cement paste and aggregates both show brittle nearly linear elastic behavior and a sudden failure. In contrast, concrete shows significant quasi-ductile behavior until reaching the fracture due to the development of multiple micro cracking in the *ITZ* [20].

The presence of an Interfacial Transition Zone (*ITZ*) between cement paste and aggregate has been demonstrated from several authors [21], [22], [23]: it represent the most important interface in concrete [3] and is common viewed as the weak link in concrete. The origin of the *ITZ* lies in the so called "wall effect" of packing of cement grains against the relatively flat and big aggregate surface: the cement particles suspended
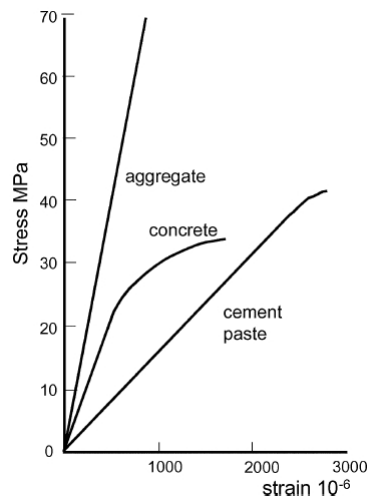
Figure 1.12. Stress-stain curves of cement paste, aggregate and concrete [20].

in water, cannot efficiently pack when they are in the close vicinity of a larger solid aggregate particle. The result, is a narrow region with a thickness of $40 \pm 50 \ \mu m$ around the aggregate particles with fewer cement particles and more water, meaning higher *w/c* and thus, higher porosity, than the bulk paste (Figure 1.13 and 1.14). The structure of *ITZ* is very complex and characterized by large and flat Portlandite crystals ($Ca(OH)_2$) perpendicular to the surface of aggregate grains, favoring the nucleation and propagation under load of micro cracks within this layer [20]. We can so affirm that the adhesion between aggregate and cement paste within the transition zone is one of the factor that governs the concrete final strength. The forces of adhesion of coarse aggregate grains to cement paste are commonly believed to have a twofold nature. On one hand, these are physical forces whose magnitude depends on the topography and shape of the aggregate grains. On the other hand, the adhesion forces can be due to chemical bonds created at the aggregate-cement paste interface. The latter occurs when the aggregate is chemically active towards the cement paste meaning that the composition and structure of the transition zone can be intentionally modified to enhance the strength of the aggregate-cement paste interface. Studies were conducted, including the preconditioning of aggregate grains by coating the grains, increasing grain roughness or the cement paste density [24]. Improvement in the properties of the transition zone can also be achieved adding a proportion of fine particles, such as

silica fume (particles of amorphous silica ranging in size down to 100 *nm*), which can pack closer to the aggregate surface enhancing the adhesion and fills micropores present in the cement paste improving the mechanical properties of the cement paste within the *ITZ*, enhancing the quality of the concrete.
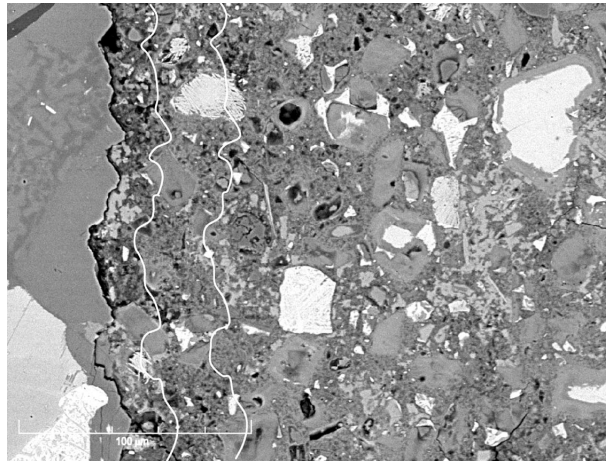
Figure 1.13. Backscattered electron image of concrete, aggregate on left. The white lines indicates distances of 20 and 50 *μm* from interface [20].
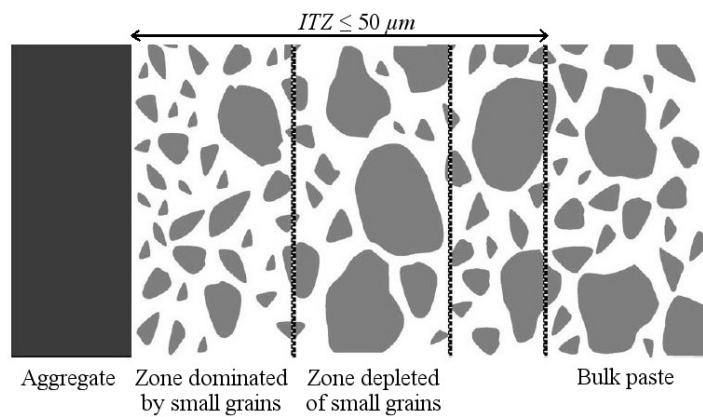
Figure 1.14. Schematic representation of grading of cement grains in the *ITZ* [20].

1.4 Reinforced concrete

The poor compressive and flexural strength of the concrete must be in some ways counteracted to improve the durability of the structure. We can identifies two different approach for the toughening of the concrete:

- inclusion of materials having higher tensile strength and/or ductility: increasing the mechanical resistance of the concrete as a whole without changing the chemistry of the singles components;

- additive: chemical and/or natural admixture that can modify the properties of the cement paste leading to, not only better resistance of the concrete as a whole, but also of the single component of the concrete itself.

The use of chemical additive such as water reduces (plasticizer or superplasticizer additives like the polycarboxylate superplasticizer *PCs*) is common nowadays: they reduce the amount of water that must be added to the mixture without losing the workability of the paste. The concrete obtained with plasticizer has a lower *w/c* ratio resulting in a higher quality concrete, as seen in the Paragraph 1.3.1. Other kind of additives used nowadays are mineral additives such as pozzolanic materials, fly ash or silica fume which determine an improvement in compression resistance and durability but, on the other hand, mineral additives reduce the workability. The beneficial effects of pozzolanic materials are mostly attributed to the pozzolanic reaction: the calcium hydroxide (Portlandite) which do not contribute to the mechanical resistance of the cement paste, is consumed and additional *C-S-H* is produced. Although, the pozzolanic reaction products fill the pore in the structure, leading to a refining of the pore size distribution of the cement paste [4].

The reinforcing approach can be also divided in another way, considering the dimension of the reinforcement material that we use:

- macroscopic level: we talk about steel rebar, which are put inside the concrete in the areas that are expected to be in tension. When the beam of reinforced concrete bends, the concrete supports the compressive loads and the steel bars support the tensile one. However, there are some issues associated with rebar such as corrosion induced

by chloride ions, which diffuse rather easily through the cement paste reaching the internal reinforcement;

- microscopic level: use of microfiber (carbon, glass or polymeric) and micro particles (silica fume, fly ash) to control the nucleation and growth of cracks on the microscale, inducing modification at the microscopic level [4]. ;

- nanoscopic level: nanomaterials such as nanoparticle and nanofibers produce an higher degree of hydration due to the large total surface area and can provide chemical modification at the nanoscale, having so the potential to improve the mechanical properties. Some example are nano-silica (SiO_2) [25], nano-alumina (Al_2O_3), nano-iron (Fe_2O_3) [26], nano-titanium oxide (TiO_2) [26], nano-clay and nano-calcium carbonate particles ($CaCO_3$) [27]) or also carbon nanotubes (*CNTs*) [28] and graphene oxide (*GO*) [29];

In the following Paragraph will be discussed different case of study: the Fiber Reinforced Concrete (*FRC*), the use of nanoparticle and carbon nanotubes as reinforcing material in the cement paste. The use of graphene oxide will be widely discuss in the Chapter 2.

1.4.1   Fiber Reinforced Concrete

Fiber Reinforced Concrete (*FRC*) research, began in the 1960s and still continue nowadays [29], [30], [31]. Currently, *FRC* is commonly used for special applications like bridges, earthquake-resistant structures and precast concrete. The main fibers used nowadays as reinforcement for concrete are:

- steel fibers and microfibers of different shapes and dimensions, used for controlling the cracks related to expansion caused by alkali silica reaction and rebar corrosion (Figure 1.15 a and b);

- glass fibers characterized by 72.4 *GPa* of elastic modulus and 3.45 *MPa* of tensile strength (Figure 1.15 c);

- synthetic fibers: polypropylene, polyethylene and polyolefin, polyvinyl alcohol (*PVA*), polyacrylonitrile (*PAN*), etc;

- carbon fibers with elastic modulus exceeding 200 *MPa* and tensile strength of 3.5 *GPa* (Figure 1.15 d);

- asbestos fibers are no longer used because of health risks [3].

a)

b)

c)

d)
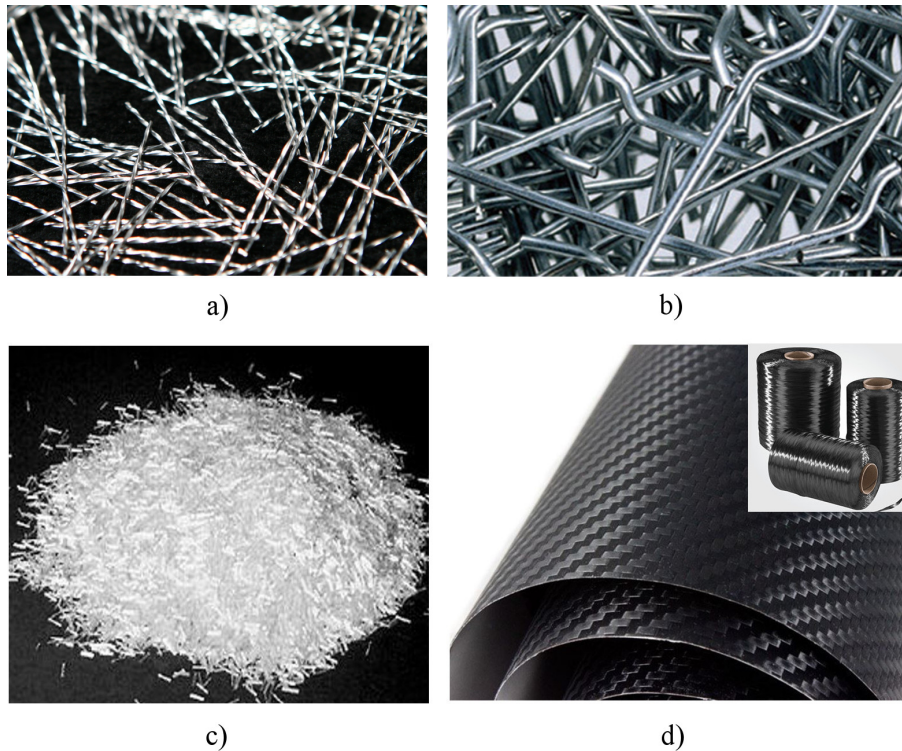
Figure 1.15. Fibers used in reinforced concrete: a-b) steel fibers, c) glass fibers, d) carbon fibers.

The influence of fibers on cracking of cement-based matrix is explained in Figure 1.16: thanks to the fibers, large single cracks are replaced with dense systems of micro cracks, which may be acceptable from both safety and durability viewpoints [30]. In Figure 1.17 is also reported the effect of long and short fibers on the macro and micro cracks. To bridge a large number of micro crack under load, and to avoid large strain localization, it is better to use short fibers, instead the long one are mainly use for the bridging of discrete macro cracks. One of the drawbacks of the addition of fibers, in particular the long ones, is the significant loss of workability of the wet concrete: *FRC* is difficult to mix, pour, and place because the fibers prevent the concrete from flowing easily. Another downside of the uses of fibers in concrete is that rise the total cost of the final product: the *FRC* is

expensive compared to the other reinforced concrete. At the present, *FRC* is used primarily for high-wear applications and for specially applications such as repair patches or for earthquake-resistant structures.
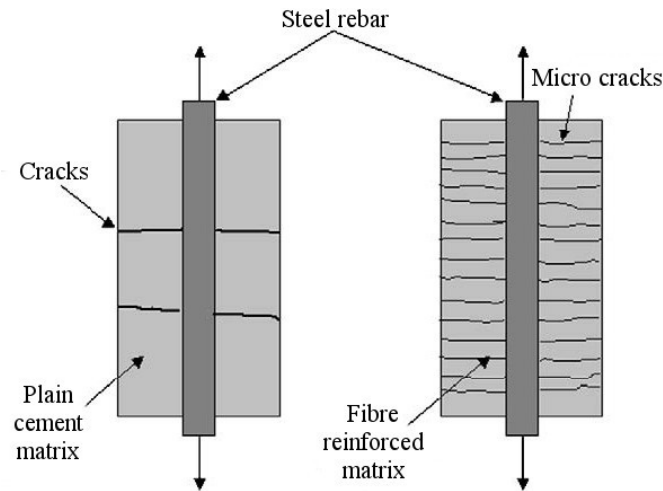
Figure 1.16. Crack pattern in reinforced concrete and fiber reinforced concrete (*FRC*) elements subjected to tension [30].
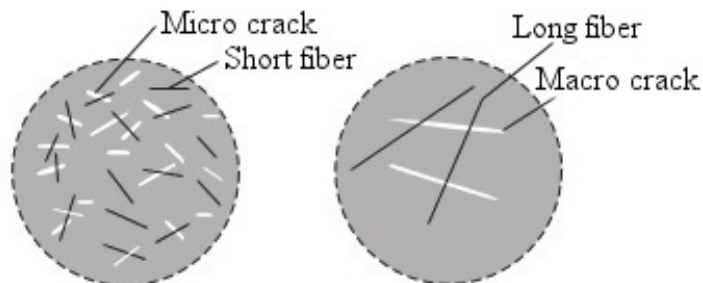
Figure 1.17. Effect of short and long fibers on micro and macro cracks [3].

1.4.2 Nanoparticles Reinforced Concrete

Nanoparticles show unique physical and chemical properties due to their size (10-70 *nm*): in fact nanoparticles has the ability to fill the pore in the cement structure and pozzolanic characteristic allowing the strengthening of the concrete. Several authors observe the effect of different nano-particle in cementitious materials. Byung-Wan Jo [32] studied the effect nano-silica (SiO_2) particles on the compressive strength and on the microstructure

of the *C-S-H* in mortar. In Figure 1.18 is reported the *SEM* image of the nano-silica particles used and Figure 1.19 reported the *SEM* micrograph of the mortar with and without nanoparticles.
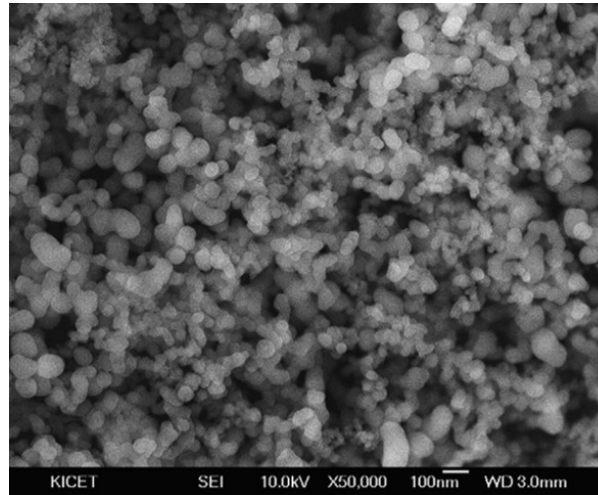
Figure 1.18. *SEM* micrograph of nano-silica particles [32].
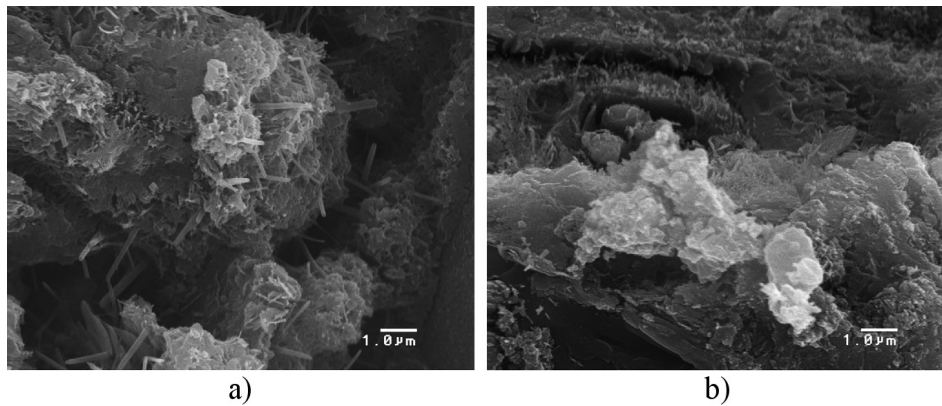
Figure 1.19. *SEM* micrograph of: a) control mortar sample, b) mortar with the admixture of nano-silica particles [32].

The mortar containing nano-silica is denser respect the control sample and characterized by compact hydration products with a reduced number of Portlandite crystals. They also evaluate the compressive strength after 7 and 28 days: in mortar samples, containing nano-silica particles is, in every case, higher than the control sample. This difference in strength can be attributes to the effective pozzolanic reaction of nano-silica particle that consume the

Portlandite and gives an higher amount of *C-S-H*. The compressive strength was found to increase as the nano-silica content increased from 3% to 12%, however, it should be noted that using a high content of nanoparticles must be accompanied by adjustments to the water and superplasticizer dosage in order to ensure that specimens do not suffer of cracking and low workability. Also K. L. Lin [33] study the effect of nano-silica in cement mortar reaching nearly the same conclusion of Byung-Wan Jo: increasing in compressive strength and decreasing in the setting time. Hui Li [34] tests the uses of not only nano-silica but also of nano-iron (Fe_2O_3) in cement mortar: he found a denser and compact texture of hydrate products in presence of the nanoparticles, without big crystals of Portlandite. Although they test not only the compressive strength but also the flexural one, observing also in this case an higher resistance. These studies demonstrate the improvement in strength due to the present of nanoparticles (nano-silica, nano-iron) that allow the reduction of Portlandite with the increasing of the *C-S-H* content due to their pozzolanic characteristic, leading to a more compact and homogeneous structure.

1.4.3   Carbon Nanotubes Reinforced Concrete

Carbon nanotubes (*CNTs*) are one of the carbon allotropes with a cylindrical nanostructure that can be viewed as a single planar sheet of graphene rolled.

The *CNTs* can be divided into two major categories [28]:

- Single-Walled Carbon Nanotubes (*SWCNTs*): tube of a single graphene sheet normally capped at the end (Figure 1.20 a);

- Multi-Walled Carbon Nanotubes (*MWCNTs*): concentric cylindrical graphene tubes made out of *SWMNTs*. *MWCNTs* are easier to be produce (Figure 1.20 b).

Carbon nanotubes, both single and multiwalled, have attracted attention from many researchers because of their exceptional mechanical, chemical, thermal, and electrical properties: are the strongest and stiffest known fibers yet discovered in term of tensile strength and Young's modulus (1.4 *TPa*) as a result of the carbon-carbon sp^2 bonding from which derive also the extremely low electrical resistance.

a)   b)
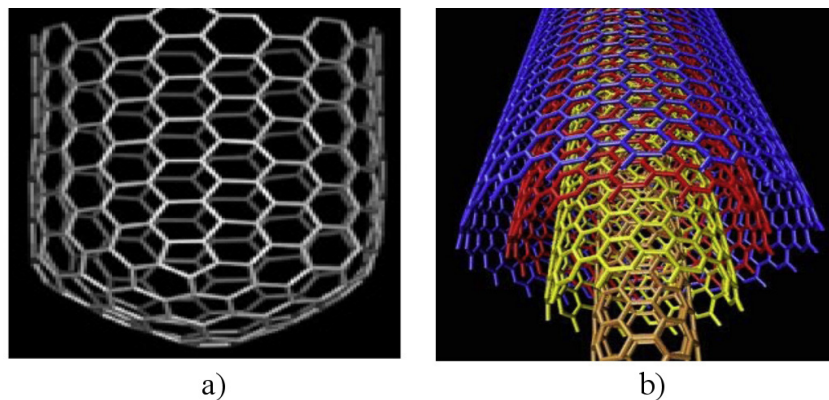
Figure 1.20. a) Single-Walled Carbon Nanotubes; b) Multi-Walled Carbon Nanotubes [28].

Nochaiya and Chaipanich [35] investigated the microstructure properties of *OPC* with *MWCNTs* (Figure 1.21) as an additive material, up to 1% *wt.* of cement. The results showed a good interaction between the hydration products of the cement pastes and multi-walled carbon nanotubes which acts as filler, leading to a denser microstructure and higher strength respect the control sample (Figure 1.22).
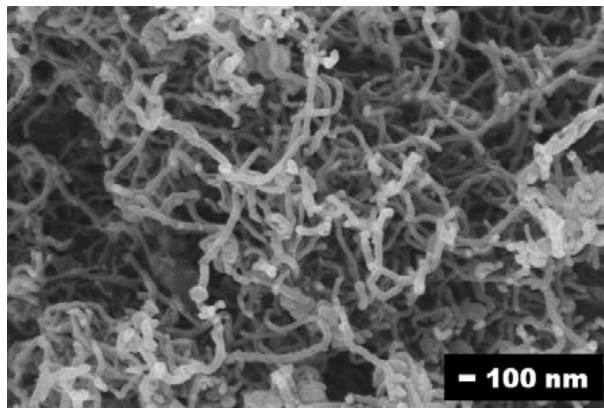
Figure 1.21. *SEM* image of the *MWCNTs* used [35].

Several other authors consider the possibility to use the *CNTs* as reinforced material for concrete: Wang et al. [36] show how *MWCNTs* dispersed by Arabic gum in *OPC*, elevates both the fracture energy and flexural toughness. Konsta-Gdoutos et al. [37] investigated the effect of two different types of *MWCNTs* obtained with the same production method, having the same diameter, but different lengths, designated as short (10-30 μm) and
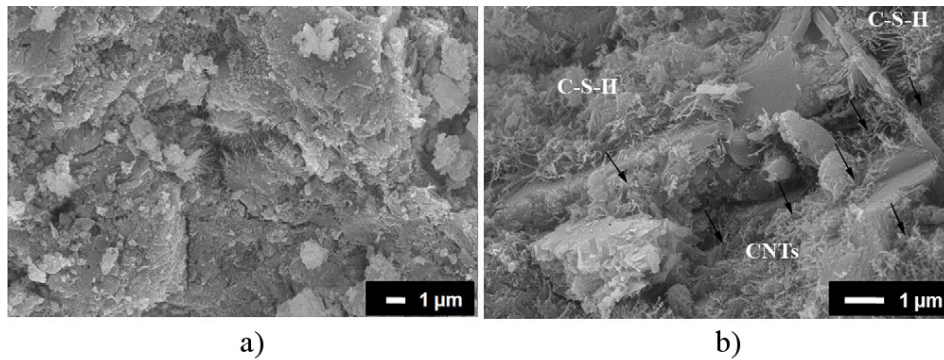
Figure 1.22. *SEM* image of: a) *OPC* used, b) Cement composites with 1% *wt.* of *CNTs* [35].

long (10-100 μm). Short and long fibers were incorporated into the composite at two different concentrations: lower concentration of 0.048% *wt.* and higher concentration of 0.08% *wt.*, respectively. They showed that, in all cases, *MWCNTs* was well dispersed in cement paste and only individual *MWCNTs* can be identified on the fracture surface (Figure 1.23). They also observed that the *CNTs* produce an increasing in flexural strength of the 25% and on the Young modulus of 45% (Figure 1.24).
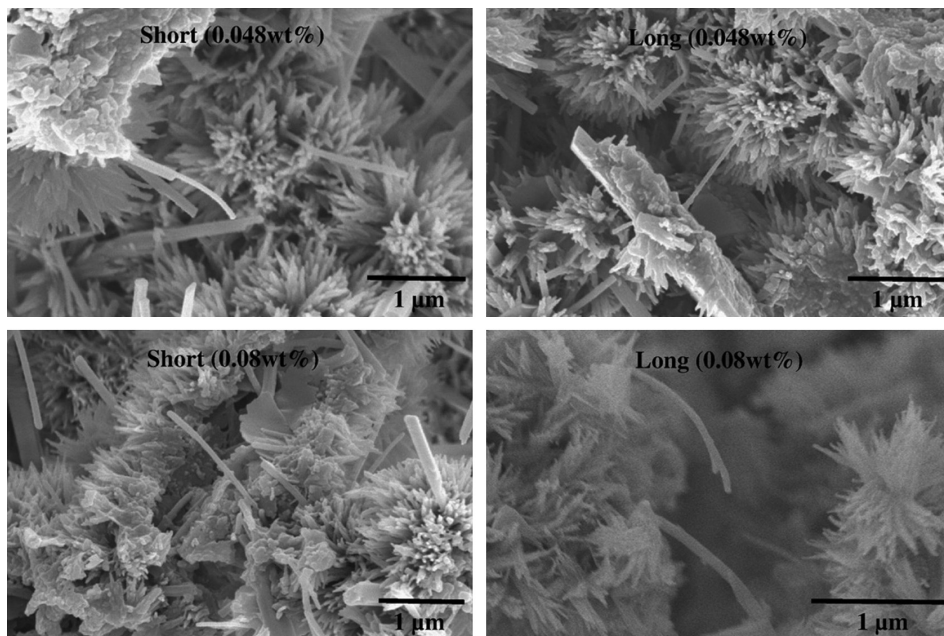
Figure 1.23. Effect of different types of *MWCNTs*, short and long with concentrations of: a) 0.048% *wt.* and b) 0.08% *wt.* in cement paste [35].
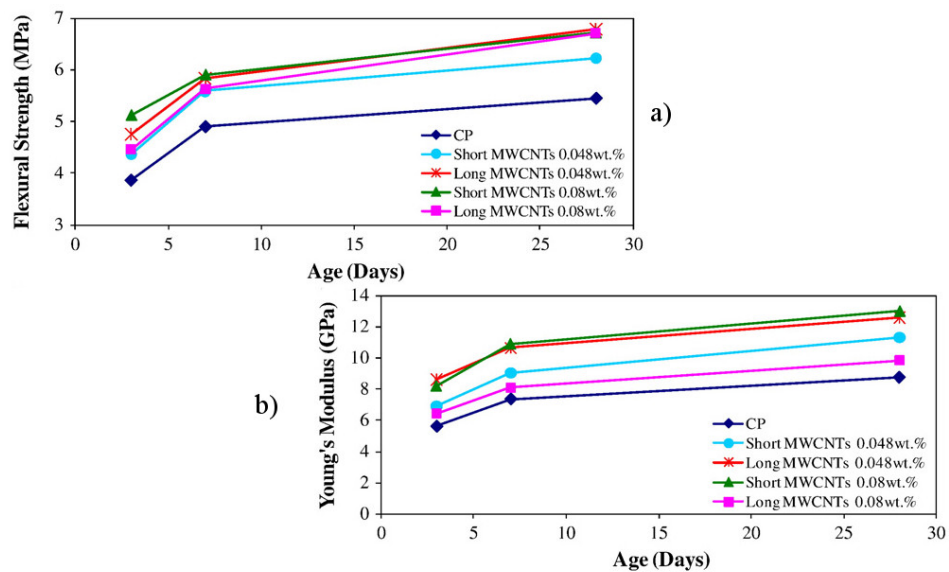
Figure 1.24. Effect of different types of *MWCNTs* and concentration on: a) the flexural strength and b) the Young's modulus of cement paste [35].

The beneficial effect of *CNTs* on the properties of the cement paste are evident but exyst data that clearly show how, under some condition, nanotubes can cross membrane barriers: this means that they can induce harmful effects such as inflammatory and fibrotic reaction in human. Care must be taken in the use of these additives.

Chapter 2

Graphene Oxide and
GO-cement composites

Cement composites are the most important and most abundant building material at the present. The use of reinforcement embedded in the cement paste allow to produce high performance cement composites (Chapter 1) but the inherent limitation of highly brittle materials, associated to the cement paste, remain unchanged. Indeed, almost the toughening methods used widely nowadays, neglects the possibility to regulate the microstructure of the cement. Graphene Oxide (*GO*) represent an opportunities to resolve this problem. In this Chapter, we will discuss the reinforcement of cement composites with graphene oxide after an introduction about the physical and chemical properties of the *GO*.

2.1   Graphene base materials

Graphene is one of the carbon allotropes and represent the basic structural unit of graphite (stack of graphene layers), carbon nanotubes (graphene layers rolled up in a cylinder) and fullerenes (wrapped graphene sheet with the introduction of pentanes on the hexagonal lattice) as the Figure 2.1 shows. Scientists have theorized about graphene for decades, but nothing thinner than 50 to 100 layers was produced before 2004 when Geim et al. successfully obtained and identified a single layer of graphene [38].

Graphene consist of a one-atom thick planar sheet characterized by hexagonal lattice in which each carbon atom has a π-orbital that contributes
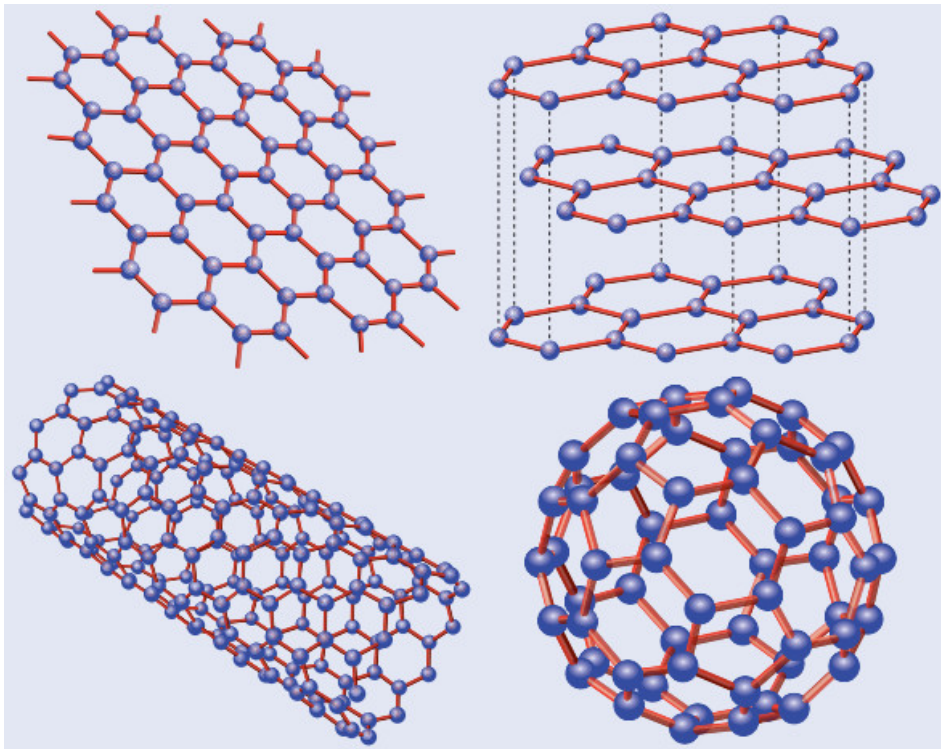
Figure 2.1. Graphene and other carbon allotropes: graphite, carbon nanotubes and fullerenes [39].

to the delocalized network of electrons that feature an extremely high mobility: this high charge carrier mobility determines the exceptional electrical and thermal properties that, combines with the transparency and the mechanical strength, make graphene an highly attractive material for future high-tech applications. All the properties of graphene are influenced by the presence of defects, intrinsic or induced, of the carbon structure that interrupt the conjugation of the system, acting as a limitation for the electron path and so their mobility. In real *3D* space, graphene can be characterized by defects like pentagons, heptagons, vacancies, ad atoms, edges, cracks, adsorbed impurities, and intrinsic ripples. The intrinsic corrugation of the graphene planes has been studies with Monte Carlo simulation [40] and transmission electron microscopy [41]: the corrugations were estimated to have a lateral dimension of about 8 to 10 *nm* and a height displacement of about 0.7 to 1 *nm* (Figure 2.2).
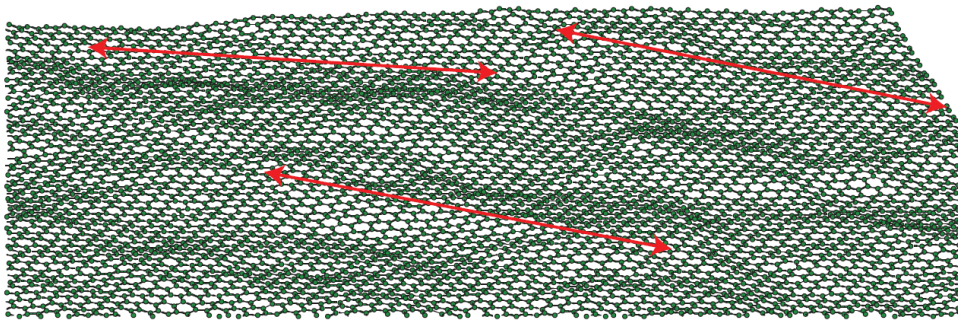
Figure 2.2. *3D* Graphene sheet characterized by intrinsic corrugation [40].

Several production techniques are available for the fabrication of graphene and the most currently used are:

- Micromechanical Cleavage (*MC*): "scotch tape" or "peel-off" method [38];

- Chemical Vapor Deposition (*CVD*): graphene film growth on various substrates (Ni(111), Cu, SiC, etc.) by feeding a source gas containing carbon atoms, like methane or ethane, at a suitable temperature [42];

- Liquid Phase Exfoliation (*LPE*): processes controlled by hydrodynamic shear-forces, associated with cavitation, that allows the exfoliation of graphite via chemical wet dispersion followed by ultrasonication in water and organic solvents [43];

- Graphite Oxide reduction: chemical or thermal treatment that allow to decrease the oxidation state of the graphite oxide and re-establish an electrical and thermal conductivity as close as possible to pristine graphene. Include treatment with hydrazine [44], as well as dehydration [45] or thermal reduction [46], [47].

Considering this last production technique, the graphite oxide can be regarded as precursor materials for the large-scale production of graphene and for Chemically Modified Graphene (*CMG*) materials (graphene sheets bonded covalently or not, with several polymers, biomolecule and nanoparticles [48]).

2.2   Graphene Oxide

On a simple level, graphene oxide can be consider as a single-layer of graphene decorated with different oxygen functionalities mostly in the form of hydroxyl and epoxy groups on the basal plane, with smaller amounts of carboxyl, carbonyl, phenol groups at the sheet edges. *GO* is mainly produced trough chemical oxidation of graphite, with subsequent dispersion and exfoliation in water or in suitable organic solvents. Its excellent solubility in water make graphene oxide an interesting material, which can be applied to numerous devices: flexible displays, transparent conducting films and transistor for large area electronics.

Due to graphene oxide nonstoichiometric composition, its amorphous characters and the inhomogeneous distribution of oxygen groups, the precise atomic structure of *GO* is still uncertain. Despite this, several structural models has been proposed over the years. In the 1939, Hofmann and Holst [49] proposed the first simple model of *GO*: only epoxy groups were bonded on the planar graphene layers (Figure 2.3 a). In 1946, Ruess [50] proposed a variation of Hofmann's model, incorporating hydroxyl groups into the basal plane and ether-oxygen functionalities, randomly distributed on the carbon skeleton. This model altered the basal plane structure to a sp^3 hybridized system, rather than the sp^2 hybridized Hofmann's model but Ruess still assumed the presence of a repeating unit allowing the formation of a regular lattice structure (Figure 2.3 b).

a)   b)
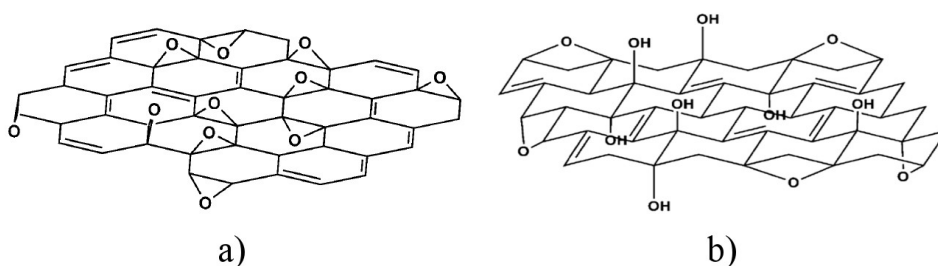
Figure 2.3. a) Hofmann model (1939) [51]; b) Ruess model (1946) [51].

In order to explain the acidic properties of graphite oxide, in the 1957, Hofmann et al. [52] revisited the previous structure incorporating also hydroxyl and carbonyl groups on graphene planes. In 1969, Scholz and Boehm [53] proposed a new structure with corrugated carbon backbone,

over which where bonded only carbonyl and hydroxyl groups. Meanwhile, Nakajima et al. [54], [55] proposed a model in which graphene oxide consist of two carbon layers linked to each other by sp^3 carbon-carbon bonds perpendicular to the layers on which carbonyl and hydroxyl groups were present in relative amounts.
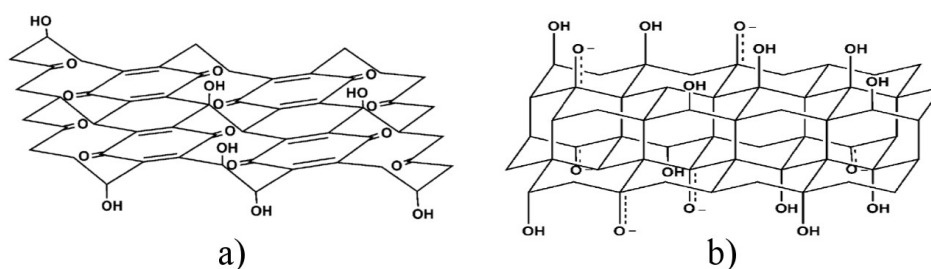
Figure 2.4. a) Scholz model (1969) [51]; b) Nakajima model (1988) [51].

The most well-known model nowadays, is the one proposed by Lerf and Klinowski [56], based on *NMR* studies: he consider a random distribution of flat aromatic regions with not oxidized benzene rings and wrinkled regions of alicyclic six-membered rings bearing hydroxyl groups and ether groups (Figure 2.5). In the 1998 Lerf and Klinowski [57] revisited their previous model, adding carboxyl groups only on the edges of the *GO* sheets.
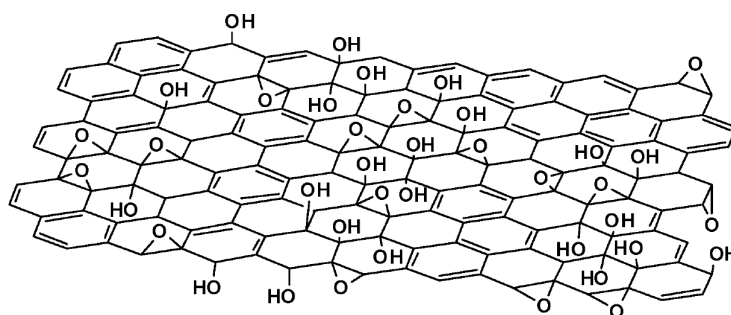
Figure 2.5. Lerf and Klinowski model (1998) [51].

In light of these previous models, Szabo et al. [58] recently proposed a new structural model that involves a carbon network consisting of two kinds of regions: trans-linked cyclohexane chairs and ribbons of flat hexagons with *C=C* bonds as well as functional groups like hydroxyl, ether, carbonyl and phenolic groups (Figure 2.6).
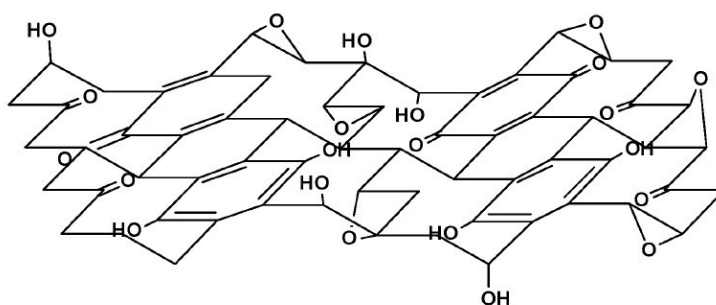
Figure 2.6. Szabo model (2006) [51].

2.2.1 Synthesis of *GO*

Graphite oxide was firstly synthesized in 1859 by the British chemist B. C. Brodie [59]: he was investigating the structure of graphite by the observation of the reactivity of graphite flakes. He performed several reaction and one of them involved the addition of potassium chlorate ($KClO_3$) to a slurry of graphite under fuming nitric acid (HNO_3). The obtained material was composed of carbon, hydrogen, and oxygen, with *C:H:O* composition of (80.13 : 0.58 : 19.29) and a net molecular formula of $C_{5.51}H_{0.48}O_1$. Successive oxidative treatments determined a further increase in the oxygen content with a variation of the *C:H:O* proportion to (61.04 : 1.85 : 37.11) with molecular formula of $C_{2.19}H_{0.80}O_1$. The presence of oxygen made the material to be dispersible in pure or basic water, but not in acidic media, which is why Brodie named the material "graphic acid".

Nearly 40 years after Brodie's discovery, Staudenmaier in the 1898 [60] improved Brodie's protocol by using a mixture of sulfuric and fuming nitric acid followed by the addition of potassium chlorate in multiple aliquots over the course of the reaction. This slight change in the procedure, resulted in an overall extent of oxidation (*C:O*~2:1) similar to what Brodie obtained with multiple oxidation approach, but performed more practically in a single reaction.

Hummers and Hoffman [61], 60 years later Staudenmaier, developed an alternative procedure for the oxidation of graphite involving a mixture of sodium nitrate ($NaNO_3$), potassium permanganate ($KMnO_4$) in concentrated sulfuric acid (H_2SO_4), achieving levels of oxidation similar of those obtain with the previous method.

Figure 2.7. Hummer's method for *GO* production [62].

The Hummer's method has at least three important advantages over previous ones:

- the reaction can be completed within a few hours;

- $KClO_3$ was replaced by $KMnO_4$ to improve the reaction safety, avoiding the evolution of explosive ClO_2;

- the use of $NaNO_3$, instead of fuming nitric acid, eliminates the formation of acid fog.

However, it still has two downside: the oxidation reaction releases toxic gasses (NO_2 and N_2O_4) and the residual Na^+ and NO_3^- ions are difficult to be removed from the waste water formed during the processes [63].

Thereafter, several other authors proposed many oxidation procedures, mainly revisiting and improving the Hummer's method. Malgorzata et al. [64] proposed the uses a mixture of perchloric and nitric acid in presence of potassium chromate (K_2CrO_4) as oxidant agent. Chen et al. [63] instead proposed, an eco-friendly synthesis of *GO*: they demonstrate the possibility to obtain *GO* without using $NaNO_3$, reducing the cost and the environmental duty of *GO* production. Tour et al. [65] suggested a variation of the Hummer's method excluding $NaNO_3$ (less toxic gas evolution) and performing the oxidation of graphite in a 9:1 mixture of concentrated sulfuric and phosphoric acid (H_2SO_4/H_3PO_3) in presence of potassium permanganate. This protocol yield to a materials called *IGO* (Improved Graphene Oxide) which is characterized by an higher oxidation state and a more regular structure respect what can be obtained with the original reaction, leading to also an higher fraction of well-oxidized

hydrophilic material. The most syntheses procedure nowadays is the so called modifies Hummer's method which combine a very long oxidation period with a high controlled purification process and a sonication stage to ensure the complete exfoliation of the graphite oxide in graphene oxide [66].

It has been demonstrated that the products of these reactions shows strong variance, depending not only on the particular oxidants used, but also on the graphite source and reaction conditions [51]. This must be take into account if samples and analyses obtained from different papers must be compared.

2.3 Graphene Oxide characterization

2.3.1 Structural characterization of *GO*

In order to explore the *GO* structural features various techniques has been employed. One of the easiest is the X-ray Diffraction analyses (*XRD*) that several authors [65], [67], [68] used to determine the interlayer distance of graphene oxide nanoplatelets. All of them found a decrease in the diffraction angle (2θ) from 26° (for graphite) to 9.45-10.7° (for the *GO*), variation that depends on the experimental procedure and on the used materials. This correspond to an increase in the interlayer distance from 0.34 to 0.94 *nm*, due to the appearance of oxygen containing functional groups upon the oxidation process. In Figure 2.8 are reported the *XRD* pattern of graphite and *GO* obtained by Roghani-Mamaqani and coworkers [62]: the presence of a small amount of diffuse scattering means that a part of the *GO* exist in the amorphous phase.
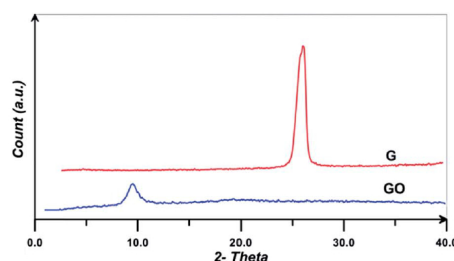
Figure 2.8. XRD pattern of graphene and *GO* [62].

The Selective Area Electron Diffraction (*SAED*) has been used from Wilson [69] for the crystal characterization of single, double and multi-layer *GO*. In Figure 2.9 are reported the SAED pattern obtained for the three different specimens:

a) single layer *GO*: clear diffraction spots characteristic of the hexagonal lattice, are observed. The presence of sharp spots indicate short-range and long-range orientation order meaning that the *GO* is not completely amorphous and maintained the regular structure of the pristine graphite (Figure 2.9 a);

b) double layer *GO*: is a superposition of two hexagonal patterns rotated by 14.5° which is the angle that corresponds to the misorientation between two individual *GO* sheets (Figure 2.9 b);

c) multi layers *GO* (15-20 layers): ring pattern suggests that there are no preferred stacking orientations between the *GO* monolayers and it is characteristic of polycrystalline samples (Figure 2.9 c).
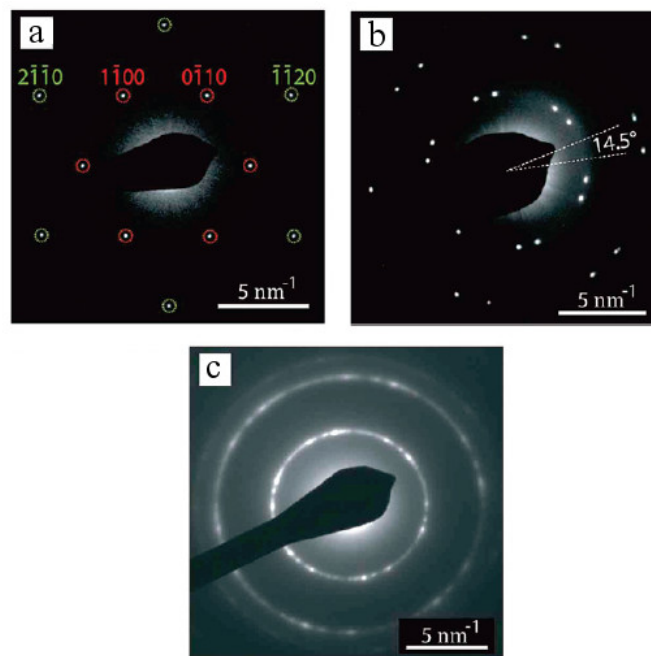
Figure 2.9. *SAED* pattern of: a) single, b) double and c) multi-layer *GO* [69].

The Raman spectroscopy is become one of the most powerful techniques to characterized graphene and related material: is mostly used to observe the degree of order or disorder in the crystal structure [70], [66], [69], [65]. In the Figure 2.10 is reported the Raman spectra of disorder graphite and *GO* obtained by Roghani-Mamaqani [62].
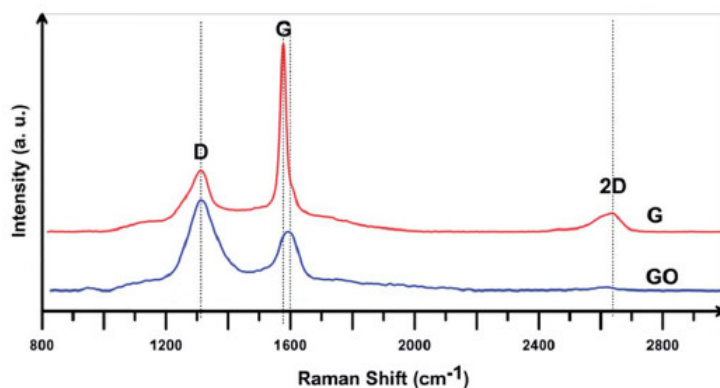
Figure 2.10. Raman spectra for graphite and GO [62].

Three characteristic peaks are individuated in the graphite spectrum:

- *D* band at 1313 cm^{-1}: is associated to the collective breathing mode of aromatic rings and Raman activated in the presence of either disorder, structural defects (holes, sp^3 or sp carbon atoms, etc.) or edges of the graphitic layers;

- *G* band at 1580 cm^{-1}: characteristic of bulk crystalline graphite due to in-plane bond stretching of the sp^2 carbon atoms in the aromatic domains;

- *2D* or *G'* band at 2641 cm^{-1}: originates from the second order vibration of the *D* peak of the nanoplatelets [71].

Considering now the spectrum of graphene oxide (blue line in Figure 2.10) is evident, even in this case the presence of the *D* peak, associates to a disorder structure which is also reflected by the blue-shifted *G* bands (1599 cm^{-1}) respect the same one in the pristine graphite. These Raman spectra confirm that the oxidation process induced the formation of defect and edges in the carbon skeleton, respect the graphitic materials.

2.3.2 Chemical characterization of *GO*

The oxygen functional groups bonded randomly on the *GO* surface, have been identified using various spectroscopic techniques, including Solid-State Nuclear Magnetic Resonance (*SS-NMR*), X-ray photoelectron spectroscopy (*XPS*) and Fourier Transform Infrared spectroscopy (*FT-IR*). *NMR* analyses in particular, were performed mainly by those author that proposed a structural model for the *GO* [56], [57]. Cai et al. [72] synthesized *GO* following the Hummer's method and High-resolution solid-state *NMR* with magic angle spinning (*MAS*) has been used as a primary method to characterized *GO* at the molecular level. In the Figure 2.11 is reported the *1D* and *2D NMR* spectra obtained: it confirm the presence of epoxy (60 *ppm*), hydroxyl (70 *ppm*) and carboxyl group (196 and 169 *ppm*).
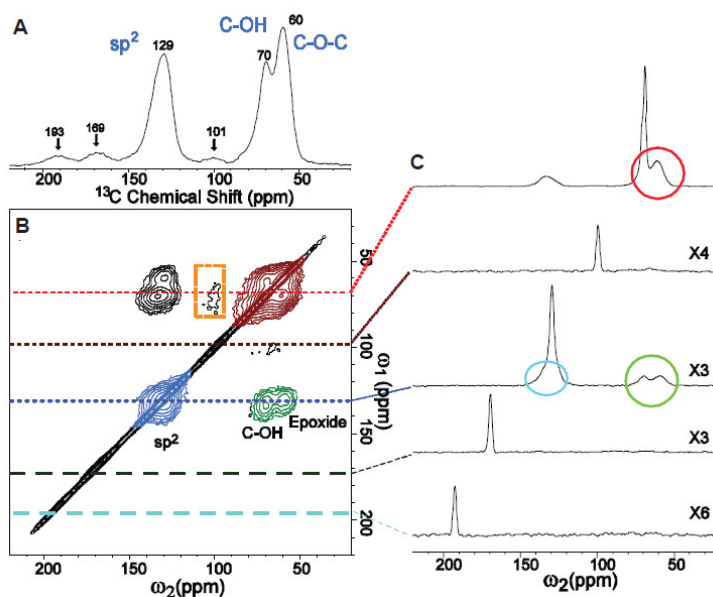
Figure 2.11. a) *1D* ^{13}C *MAS* and b) *2D* $^{13}C/^{13}C$ chemical-shift correlation solid-state NMR spectra of $^{13}C-$labeled graphite oxide with c) slices selected from the *2D* spectrum at the indicated positions (70, 101, 130, 169 and 193 ppm) [72].

The X-ray photoelectron spectroscopy (*XPS)* is used to reveals the nature of the carbon-oxygen bonds in their various states: sp^2 carbon, *CO*, *C=O*, and *COOH* [63], [73]. As an example, in the Figure 2.12 is reported the *XPS* spectrum obtained by Bansal et al. [74].

XPS and *NMR* are very powerful techniques but difficult to performed and with not easy interpretation of the obtained results. Instead, Infrared
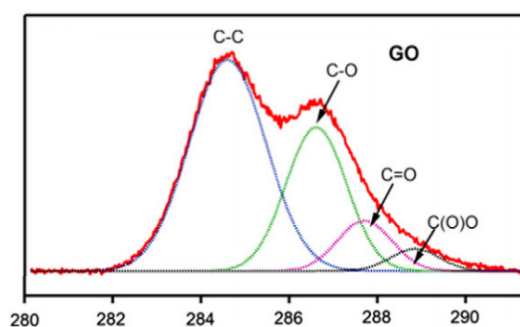
Figure 2.12. X-ray photoelectron spectra of *GO* with peaks deconvolution [74].

spectroscopy is easy, fast and do not involved the preparation of the sample over specific substrate. In Figure 2.13 is reported the transmission infrared-absorbance spectrum of *GO* obtained by Acik et al. [75]. They identifies different contribution: hydroxyl (*C-OH*), ketonic species (*C=O*), carboxyl (*COOH*), sp^2-hybridized *C=C* (in-plane vibrations), epoxide (*C-O-C*) and various *C-O* and *C=O* containing chemical species which are located in the three spectral regions labelled α, β and γ characteristic of ether-like and ketone-like species. In the same Figure is also reported a schematic representation of *GO* and the functional groups identified in the spectrum: epoxide (green), *CO* (red), *COH* (blue), *COOH* (brown), *C=O* (grey) and *C=C* (light blue).
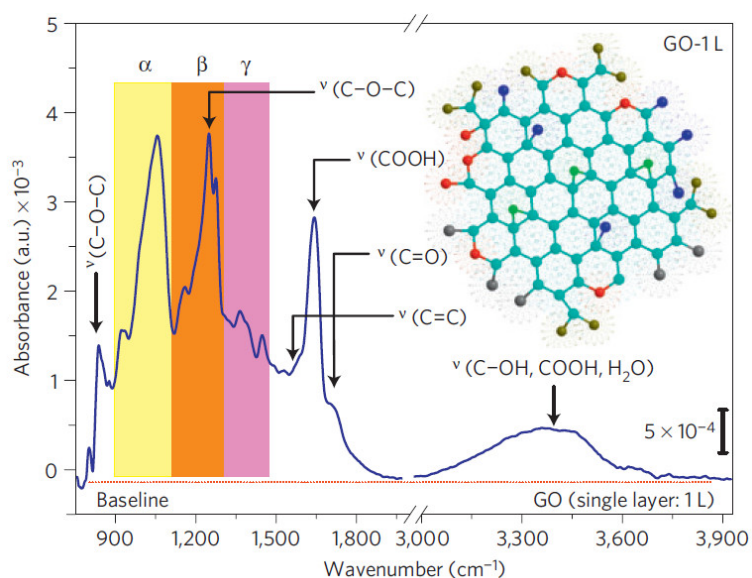
Figure 2.13. *FT-IR* spectra of graphene oxide [75].

2.3.3 Thermal stability of *GO*

The determination of the thermal stability of *GO* is important in particular for technological applications in electronic and in energy storage devices, but nevertheless, has not been fully studied. Considering the structural characterization reported in the previous Paragraph, we can affirm that graphite oxide had a similar structure to that of its precursor (the graphite), except for the higher interlayer distance and the additional functional groups, which were distributed randomly on the carbon backbones. Nowadays it is still not clear how interlayer distance is related to the presence of functional groups or how functional groups react to heat treatment.

Several author used Thermogravimetric Analyses (*TGA*) for the determination of the characteristic decomposition temperature of the *GO* and of the oxygen functionalities bonded over it. Every one observed nearly the same behavior:

- little loss till $100°C$ due to the losing of water;

- between $100°C$ and $300°C$ a loss due to the decomposition of the most labile oxygen groups;

- between $300°C$ and $600°C$ a little loss is sometimes observe due to the decomposition of the most stable oxygen functionalities;

- after $600°C$ we can observe the combustion of the carbon backbone of the *GO*.

In Figure 2.14 a and b, are reported *TGA* analyses observed from Wilson [69] and from Chen [63], respectively: variation can be observed, in the characteristic decomposition temperatures, due to different synthesis approach or reagent used for the preparation of *GO*. Jeong et al. [68] studies in particular the effect of different thermal treatment at $200°C$ for various time (2 *h*, 5 *h*, 6 *h*) on the thermal stability of the oxygen functionalities (Figure 2.15). They observed an evident differences in the *TGA* curves when the *GO* is treated for 6 *h* at $200°C$ before making the analyses: the loss at $236°C$, attributed to the loss of oxygen functionalities, is very little, meaning probably that the thermal treatment induce a non-complete reduction of the *GO* (some oxygen functionalities survived).
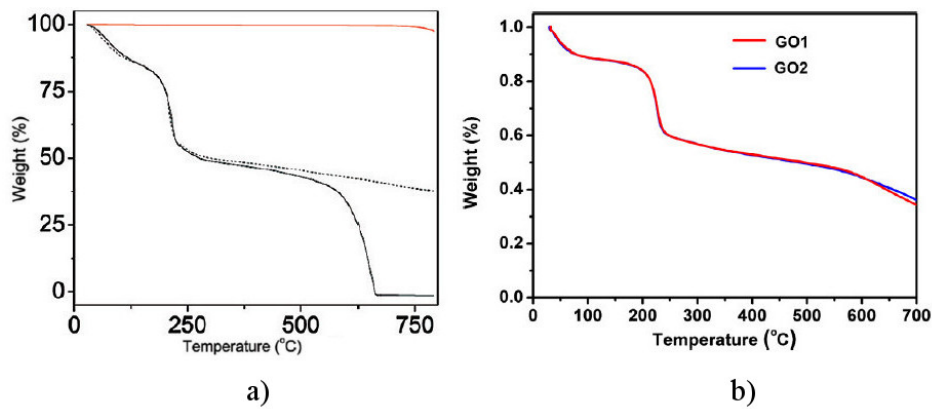
Figure 2.14. a) *TGA* of graphite powder in air (red line), graphene oxide in air (solid black line), and graphene oxide in Ar/H_2 (dashed line) [69]; b) *TGA* curves of two sample: *GO1* and *GO2* [63].
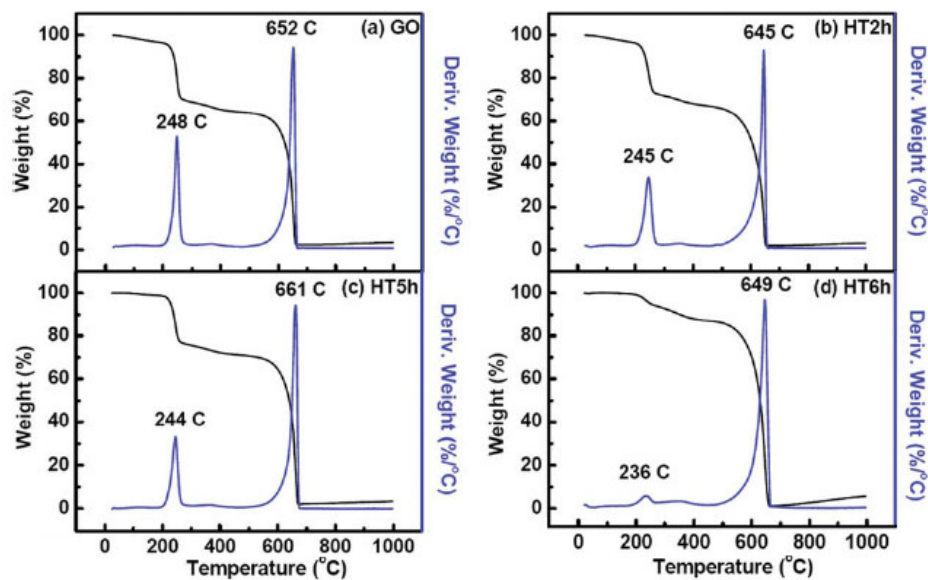
Figure 2.15. *TGA* of: a) *GO*, and *GO* treated at $200°C$ for b) *2 h*, c) *5 h*, and d) *6 h* [68].

Considering these analyses the author confirm the good thermal stability of *GO*, which may be beneficial in future electronics and energy storage device applications.

2.3.4   Morphological characterization of *GO*

Morphological features of *GO* can be observed using several microscopic techniques: Atomic Force Microscopy (*AFM)*, Scanning Tunneling Microscopy (*STM*), Transmission and Scanning Electron Microscopy (*TEM* and *SEM*). The *AFM* gives the thickness of *GO* as well as the number of layers: Stankovich et al. [44] observed that the thickness of an exfoliated sample of *GO* is uniform and nearly 1 *nm* (Figure 2.16).
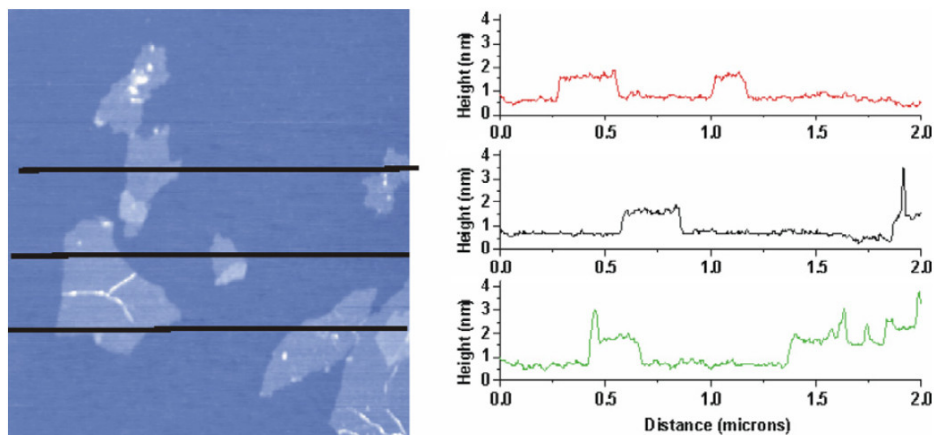
Figure 2.16. A non-contact mode *AFM* image of exfoliated *GO* sheets with three height profiles acquired in different locations [44].

Gomez and Navarro [76] in the 2007, synthesized graphite oxide via the Hummer's method, exfoliated it and then deposited onto different substrate (*Si/SiO$_2$* and highly oriented pyrolytic graphite *HOPG*). *AFM* analyses (Figure 2.17 a-b) revealed that *GO* sheets has lateral dimensions of 100-5000 *nm* and heights in the range of 1.1-1.5 *nm*, in agreement with the study of Stankovich [44]. Gomez and Navarro [76] also performed an STM analyses of a *GO* monolayer deposited over the *HOPG* substrate (Figure 2.17 d): the *GO* sheets are distinguishable from pristine graphene by the appearance of bright spots/regions (marked in green) due to a lacking in order of the lattice which arise from the presence of oxygen functional groups, but the hexagonal lattice of graphite is partially preserved.

One of the most used technique for the morphologies characterization of *GO* is the Scanning Electron Microscopy and has been used from several authors. In the 2014, Shahriary [66] and coworkers observed that the synthesized *GO*, exhibit a layered structure, formed of ultrathin film that
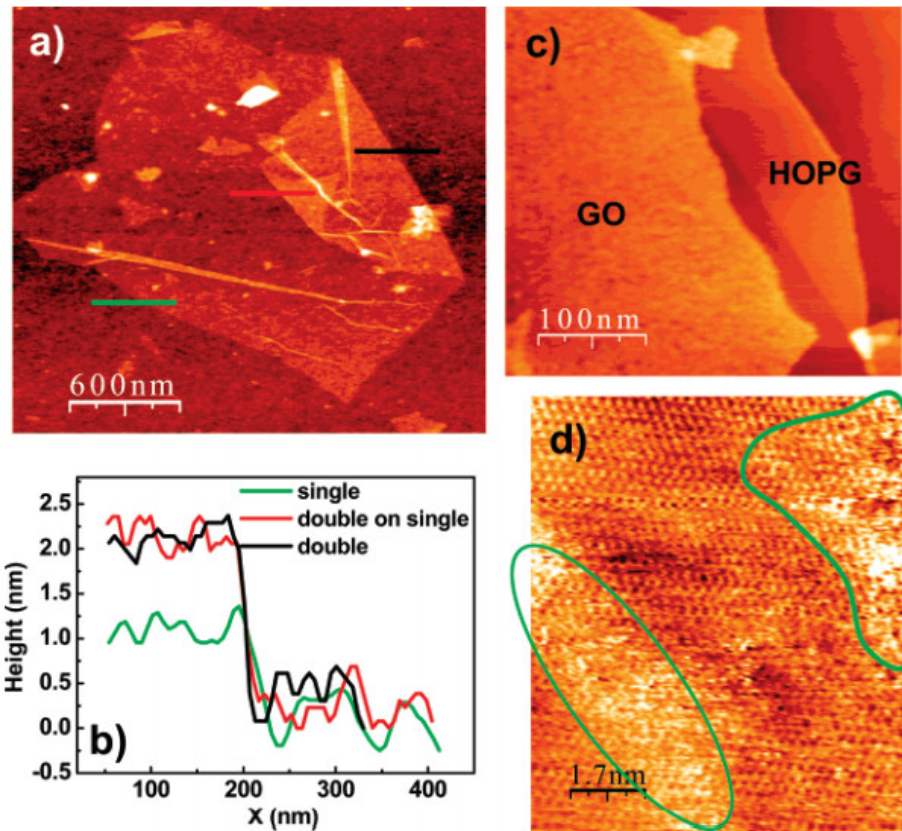
Figure 2.17. (a) *AFM* image of a *GO* monolayer deposited on a *SiO₂* substrate, showing a back-folded edge. (b) AFM section profiles along the three different lines in panel (a), revealing a mono-, bi-, and tri-layer structure. (c) *AFM* image acquired from a *GO* monolayer on a *HOPG* substrate. (d) *STM* image of a *GO* monolayer on a *HOPG* substrate, taken under ambient conditions [76].

folds in space (Figure 2.18). The same analyses has been performed by Mamaqani et al. [62] on a graphene sample and then on *GO* (Figure 2.19): bare and flat surface of graphene nanoplatelets without any curvature is clearly observed (Figure 2.19 a), instead *GO* result in packed nanoplatelets in which the oxygen-containing functional groups determine an high surface roughness. Mamaqani et al. [62] also performed *TEM* analyses on the these samples (Figure 2.20): the size of individual nanosheets of graphene extends from several hundred nanometers to ten micrometers and appears more transparent in comparison with the nanoplatelets after oxidation, which are wrinkled because of the presence of oxygen functional groups.
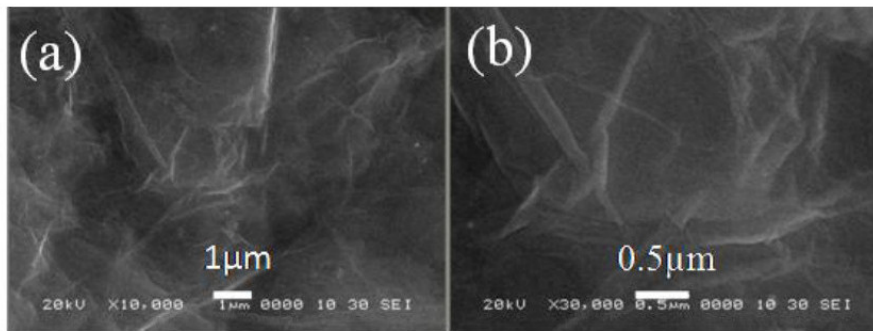
Figure 2.18. *SEM* micrograph of graphene oxide [66].
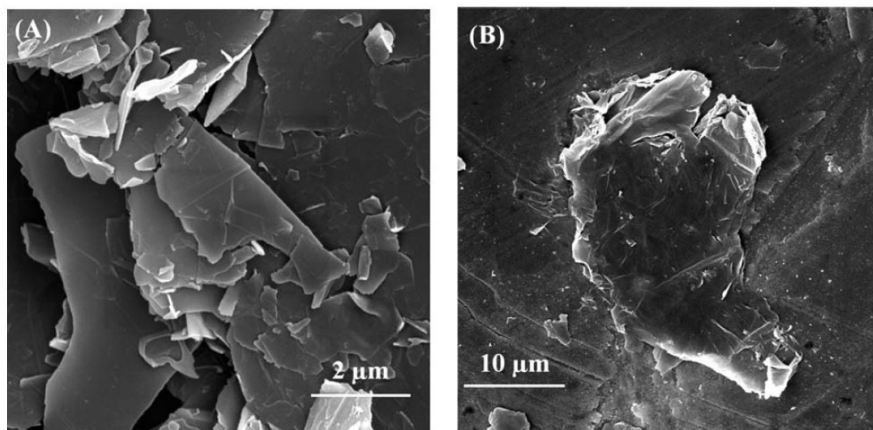
Figure 2.19. *SEM* micrograph of: a) graphene; b) graphene oxide [62].
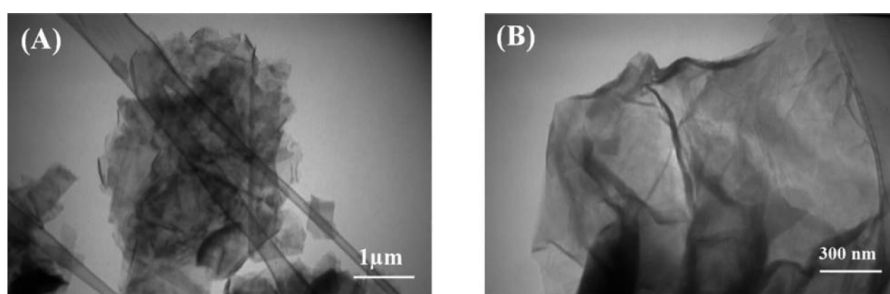
Figure 2.20. *TEM* micrograph of: a) graphene; b) graphene oxide [62].

Recently, Erickson et al. [77] use High Resolution Transmission Electron Microscopy (*HR-TEM*) to direct imaging the lattice and the topological defect of a monolayer of *GO*. The materials comprise three major regions: holes, graphitic regions, and high contrast disordered regions with approx-

imate area percentages of 2%, 16%, and 82%, respectively. The authors proposed that the holes in *GO* lattice are formed due to the release of CO and CO_2 during the oxidation and exfoliation. They also suggest that the graphitic regions (honeycomb structure) are due to the incomplete oxidation of the basal plane, while the disordered regions consist of a high-density region of oxygen functionalities. In Figure 2.21 is reported the *TEM* obtained image: we can identify region with a high degree of oxidative functionalities (Figure 2.21 a), dynamics anomalies indicating isolated mobile oxygen functionalities (Figure 2.21 b) and graphitic regions (Figure 2.21 c).
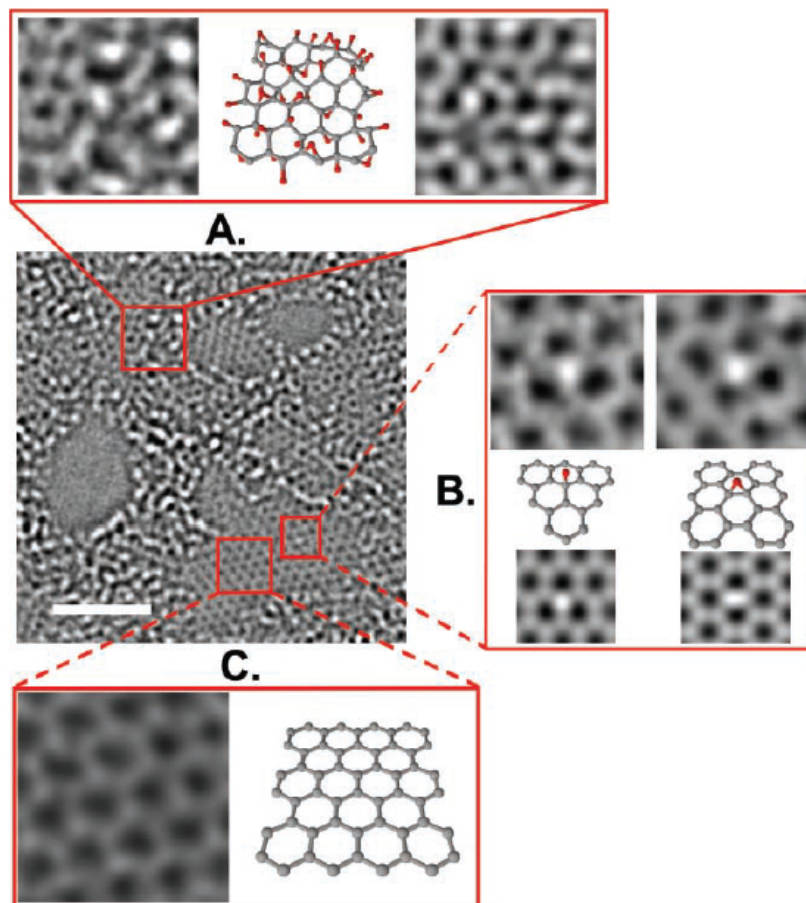
Figure 2.21. *HR-TEM* micrograph of graphene oxide [77].

2.4 Chemically Modified Graphene

Chemical Modified Graphene (*CMG*) has been studied for many applications like energy-related materials, sensors, field-effect transistors and biomedical applications due to its excellent electrical, mechanical, and thermal properties. The *CMG* is obtained using *GO* as a precursor: the different oxygen functionalities act as possible bonding points for molecules and polymers, that we decided to attached to the graphene nanoplatelets [48], [78]. Although, the *CMG* can be used to overcame one of main problem of graphene obtained with *GO* reduction: it tend to precipitate just after the addition of hydrazine and formed aggregate that could not be re-dispersed, even after a prolonged ultrasonic treatment in water and in the presence of surfactants. If the reduction is carried out in the presence of polymer or polymeric anions, the results is a stable polymer-grafted dispersion of graphene, which is a chemically modified graphene, obtained with the non-covalent approach [79].

The covalent approach for the preparation of *CMG* is the most used nowadays: several authors reports the possibility to bonds. on graphene oxide surface, different organic amines [80], [81] and polymers (polystyrene [82], [62], polyvinyl alcohol [83], polyethylene [84], polyethylene glycol [85] and epoxy [86]). The polymers chain attached on the graphene oxide surface reduce its hydrophilic characteristic by the consumption of carboxyl and hydroxyl group and formation of amide and ester bonds. In Figure 2.22 are reported different possible functionalization approach summarized by Loh et al. [87]. One of the simplest method for the functionalization of graphene oxide is the esterification of carboxylic acid, indicated in the previous Figure as (*VII*). This reaction was first described by Wolfgang Steglich in 1978 [88]: he consider the esterification of carboxylic acid in presence of dicyclohexylcarbodiimide (*DCC*) as a coupling agent, 4-dimethylaminopyridine (*DMAP*) as a catalyst and dichloromethane (Cl_2CH_2) or the dimethyl sulfoxide (*DMSO*) as suitable solvent. In Figure 2.23 is reported the mechanism of this esterification reaction which is characterized by the formation of the dicyclohexylurea (*DHU*).
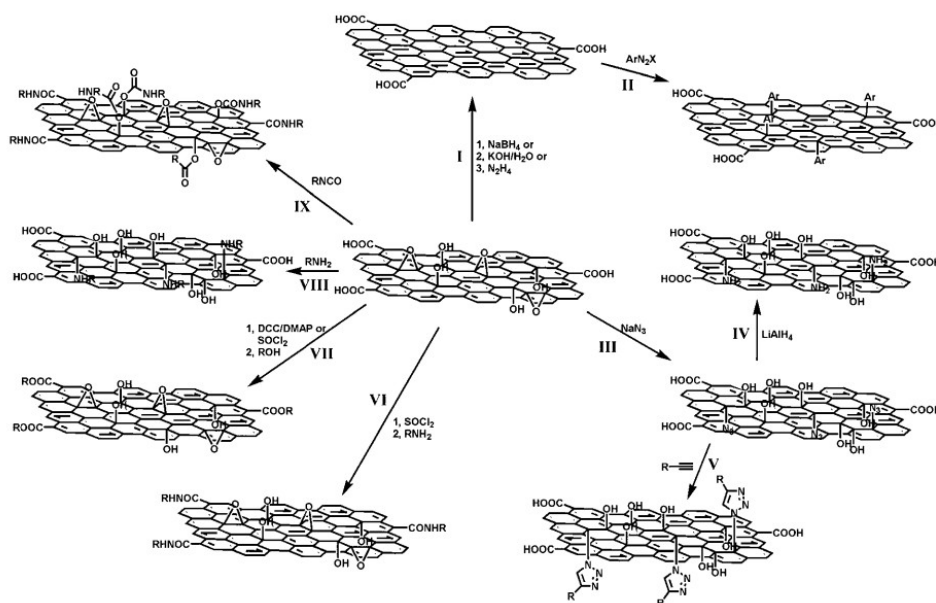
Figure 2.22. Several functionalization approach [87].
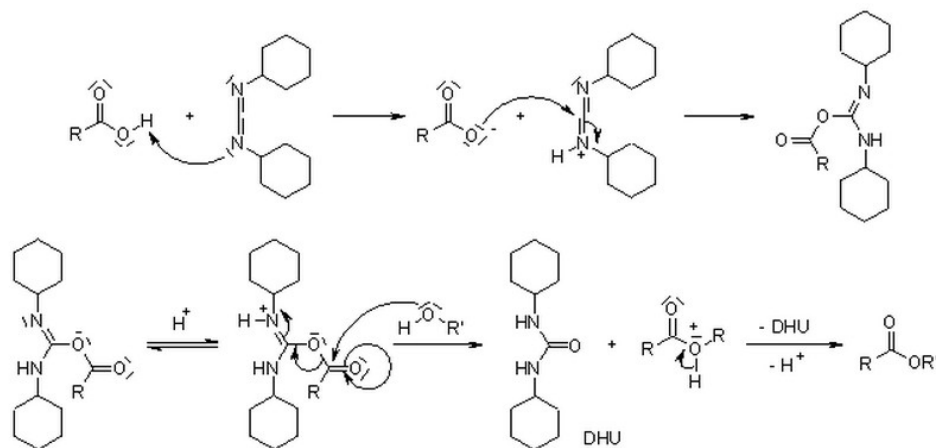
Figure 2.23. Steglich esterification [89].

Nearly all most of the covalent functionalization are performed following this procedure: the big advantages, is that generally, takes place at room temperature but there is the possibility that the *DHU* remain bonded to the graphene oxide. This is why we will performed the functionalization with *Jeffamine* without the uses of *DCC*.

2.5 Graphene Oxide cement-base composites

In the Chapter 1, we reported several studies about the possibility to rein-
force the concrete using micro and nanomaterials like fibers, nanoparticles
and carbon nanotubes. The graphene oxide, due to its unique features of a
two-dimensional materials, with several oxygen groups spread over it sur-
face, seems interesting not only for electronic industries but also for cement
application, as reinforcement additive [29]. The patent WO 2013096990 A1,
published in the 2013 by the Monash University [90], regulate the addition
of *GO* in cement mortar: it report that introducing small quantities of *GO*
(0.05% *wt.*) the compressive and flexural strength increases of 15-33% and
41-59%, respectively. Babak et al. [67] in the 2014, observed the effect of
different content of *GO* (0.1, 0.3, 0.5, 1, 1.5 and 2% *wt.*) in cement mortar, in
presence of a polycarboxylate super plasticizer (0.5% *wt.* of cement). They
report that the optimal percentage of *GO* nanoplatelets is 1.5% *wt.*, because
determine an increase in the tensile strength of 48% respect the control
sample. Observation of the fracture surface of the samples containing 1.5%
wt. GO with the Scanning Electron Microscopy (Figure 2.24) revealed that
the *GO* nanoplatelets were well dispersed and no *GO* agglomerates were
seen in the matrix.
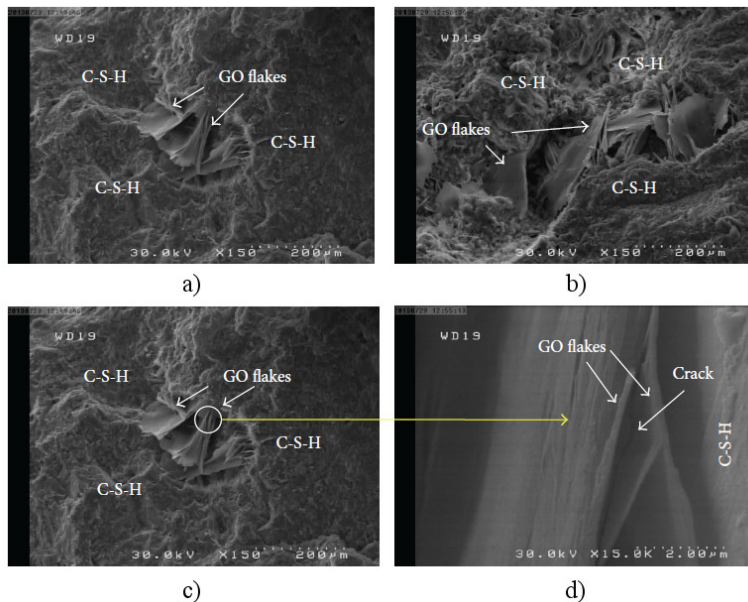
Figure 2.24. *SEM* micrograph of *GO*-cement composites [67].

In several studies, Shenghua et al. [1], [91], [92] observed the effect of the admixture of graphene oxide in several concentration (0.01, 0.02, 0.03, 0.04, 0.05 and 0.06% *wt.*) and with different dimension, in cement paste and mortar.

First of all, they found that the *GO* has an important effect on the pore structure of the hardened cement paste: it reduce the total pore area, median pore diameter and the porosity (Table 2.1). This results suggest that *GO* could help to produce more regular hydration crystals in the holes and in cracks of hardened cement paste, occupying space that although remain empty [91].

Table 2.1. Pore structures of the hardened cement pastes with different *GO* contents at 28 days [91].

GO (% *wt.*)	Total pore area (m^2/g)	Median pore diameter (*nm*)	Porosity (%)
0.00	17.40	25.80	22.61
0.01	16.32	23.58	19.78
0.02	13.35	19.26	16.20
0.03	12.33	15.35	14.67
0.04	10.12	10.60	11.94
0.05	9.41	8.72	10.78
0.06	7.34	6.51	10.75

Secondly, they observed the effect of different *GO* content on the shape of the hydration crystals with Scanning Electron Microscopy (Figure 2.25). Observing the obtained *SEM* micrograph, they make some assumptions:

- flower-like hydration product can be observed considering a low *GO* content (0.01% - 0.04% *wt.*). These hydration crystals consist of needle and rod-like product, which became thicker with higher curing age;

- as the amount of *GO* increase ($\geq$0.05%), the crystals are characterized by an irregular polyhedron-like structure.

These results indicate that *GO* can promote the production of rod-like and needle-like hydration products and their assembly into regular flower-like or polyhedron-like structure, leading to a more compact microstructure.
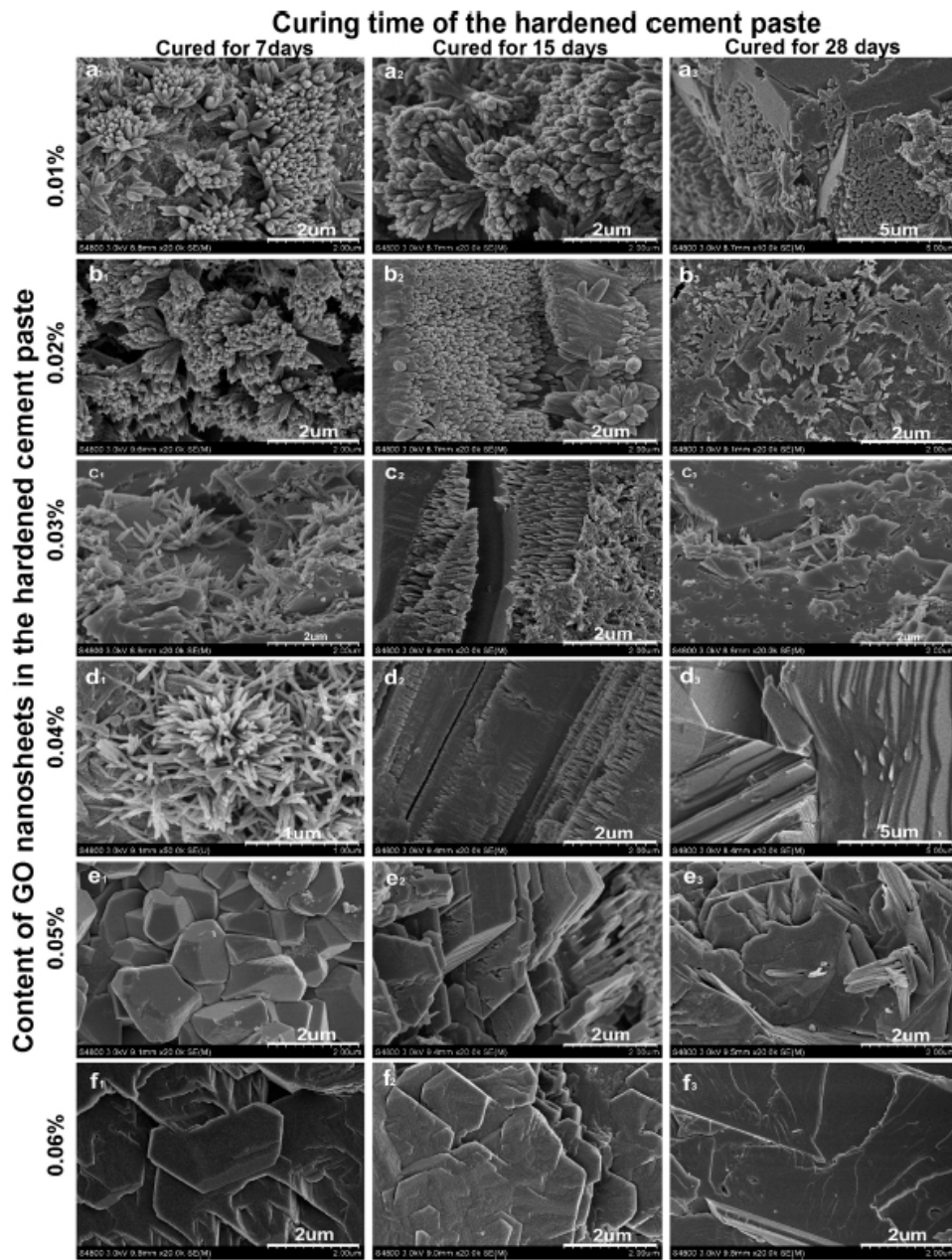
Figure 2.25. SEM images of the hardened cement pastes with different *GO* contents (a) 0.01%; b) 0.02%; c) 0.03%; d) 0.04%; e) 0.05% and f) 0.06% *bwoc* at 7 days, 15 days and 28 days: [1].

Starting from these data, Shenghua et al. proposed a regulatory mechanism of *GO* on cement hydration products: the reactive oxygen functionalities on the *GO* surface react preferentially with C_3S, C_2S and C_3A, acting as

nucleation sites for the hydration products. Although, they hypothesized that if the *GO* content is in between of 0.01% and 0.04%, a flower-like structure is obtained, instead if the *GO* content is 0.05% or 0.06%, polyhedron crystal are observed.
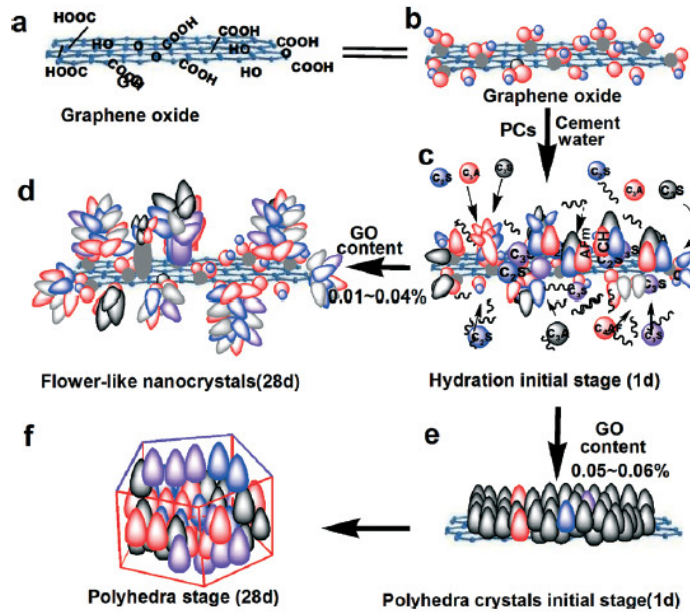
Figure 2.26. Schematic diagram of the regulatory mechanism of *GO* nanosheets on cement hydration crystals [1].

In Table 2.2 are reported the value of compressive and flexural strength at 28 days of curing obtained for all the samples analyzed before with SEM:

- the compressive strength increases with increasing *GO* content, reaching a maximum at 0.05% *bwoc*, with a maximum increase of 57.4% at 28 days respect the reference samples.

- the flexural strength increases with increasing *GO* content, reaching a maximum at 0.04% *bwoc*, after which it decreases with further increases in *GO* content. The maximum increase is of the 67.1% respect the control sample, at 28 days.

Table 2.2. Flexural and compressive strength of hardened cement pastes with different *GO* contents at 28 days of curing [91].

GO (% *wt.*)	Compressive strength (*MPa*)	Flexural strength (*MPa*)
0.00	59.31	8.84
0.01	69.65	12.34
0.02	77.82	13.68
0.03	86.62	14.72
0.04	92.36	14.74
0.05	93.38	13.53
0.06	94.26	12.63

These last results clearly indicate that *GO* nanosheets enhance the strength and toughness of hardened cement paste by regulating the morphology of the cement hydration products, obtaining a more compact and denser microstructure.

In another paper, Shenghua and co-workers [91] also investigate the microstructure of cement paste in presence of *GO* characterized by different average size: 430 *nm*, 180 *nm* and 72 *nm*. In the following Figure (2.27, 2.28, 2.29, 2.30) all the *SEM* micrographs obtained are reported: as the size of the *GO* nanoplatelets decrease, the hydrated crystal became denser and compact leading to a less porous microstructure, but they determine that the flexural and compressive strength in realty is not so influenced by the dimension of the nanoplatelets, observing the same increase reported in Table 2.2.

The overall results indicate that *GO* nanosheets can significantly enhance the strength and toughness of cement by regulating the microstructure of the cement hydration crystals, and therefore have great potential for practical application in the production of cement-based materials.
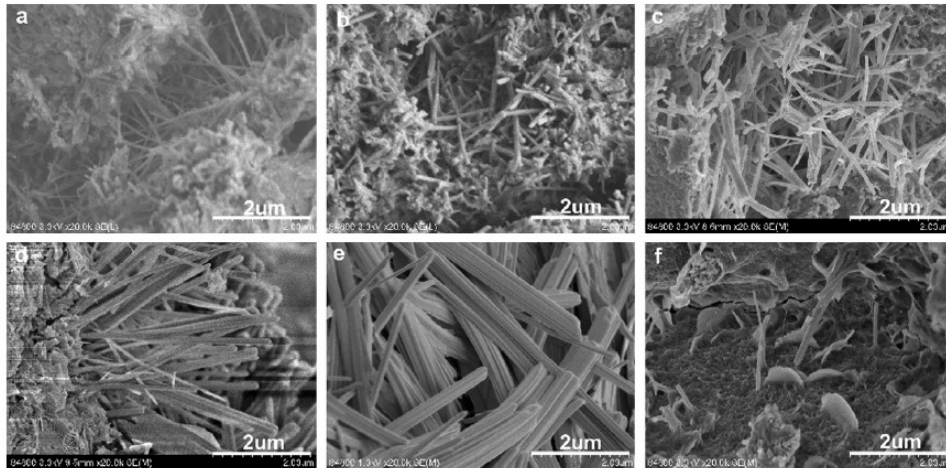
Figure 2.27. *SEM* images of hardened cement paste at 28 days: a and b without *PCs*; from c to f *PCs* 0.2% *bwoc* [91].
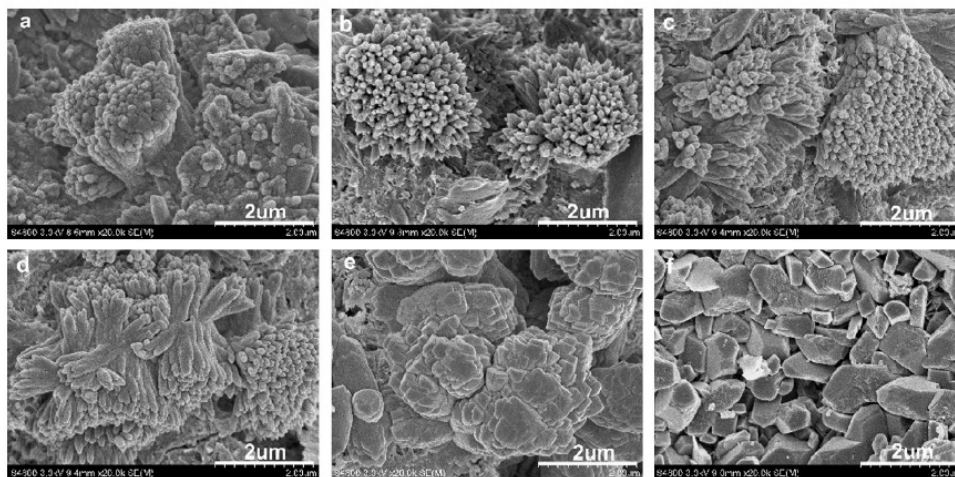
Figure 2.28. *SEM* images of hardened cement paste mixed with different dosages of *GO* nanosheets (a) 0.01%; b) 0.02%; c) 0.03%; d) 0.04%; e) 0.05% and f) 0.06% *bwoc* with average thickness 27.6 *nm* and average size 430 *nm* at 28 days [91].
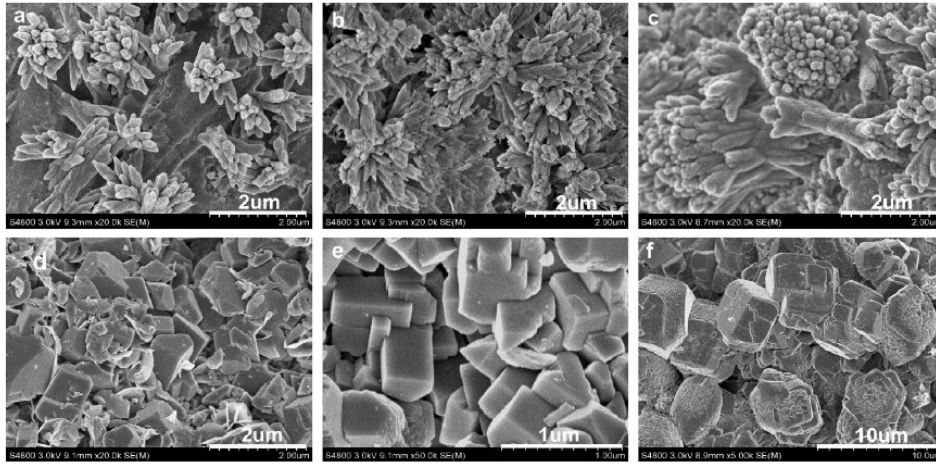
Figure 2.29. *SEM* images of hardened cement paste mixed with different dosages of *GO* nanosheets (a) 0.01%; b) 0.02%; c) 0.03%; d) 0.04%; e) 0.05% and f) 0.06% *bwoc* with average thickness 9.5 *nm* and average size 180 *nm* at 28 days [91].
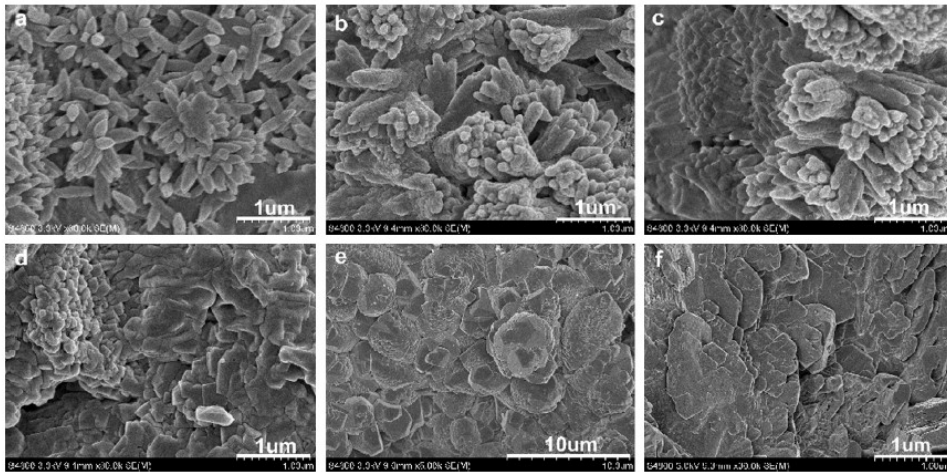
Figure 2.30. *SEM* images of hardened cement paste mixed with different dosages of *GO* nanosheets (a) 0.01%; b) 0.02%; c) 0.03%; d) 0.04%; e) 0.05% and f) 0.06% *bwoc* with average thickness 3.1 *nm* and average size 72 *nm* at 28 days [91].

Chapter 3

Materials and Experimental Procedures

This chapter reports the materials and the experimental procedures used to synthesize and characterize the graphene oxide (*GO*), the functionalized *GO* and cement base *GO* composites.

3.1 Materials

For the syntheses of graphene oxide, we performed the oxidation reaction following the known Hummer's method, described in the Chapter 2, using:

- graphite powder ($\leq 150\,\mu m$, 99.99%, Sigma-Aldrich);

- sulfuric acid, H_2SO_4 (95-97%, Sigma-Aldrich);

- sodium nitrate, $NaNO_3$ ($\geq$ 99%, Sigma-Aldrich);

- potassium permanganate, $KMnO_4$ (99% *min*, Baker Analyzed Reagent);

- hydrogen peroxide, H_2O_2 (35% *wt.* in water, Sigma-Aldrich).

Once obtained the graphene oxide we functionalized it with the *Jeffamine M600* (Huntsman) which is a polyetheramine, where the letter *M* signifies a monoamine and the number represents the approximate molecular weight. The *Jeffamine M600* is prepared by reaction of a mono-alcohol initiator with ethylene oxide (*EO*) and/or propylene oxide (*PO*), followed by conversion of the resulting terminal hydroxyl groups to amines, in particular the

Jeffamine M600 is predominately-polypropylene glycol (*PPG*) based. The Figure 3.1 report the chemical structure of this polyetheramine.
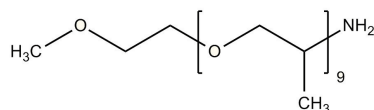
Figure 3.1. Chemical structure of *Jeffamine M600*.

For the functionalization of *GO* with *Jeffamine M600* we used different reagent (Figure 3.2):

- dimethyl sulfoxide, *DMSO* (99.8% Carlo Erba reagent) as solvent;

- dimethyl amminopiridine, *DMAP* (*RPE*, Carlo Erba reagent) as catalyst;

- acetone ($\geq$ 99%, Sigma-Aldrich) for the purification stage.

a   b
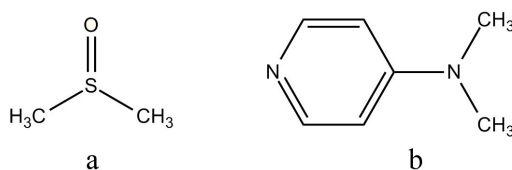
Figure 3.2. Chemical structure of: a) *DMSO*; b) *DMAP*.

The used cement for the mortar samples was a type I cement 52.5 R of Italcementi which composition, chemical and physical properties are reported in Table 3.1. For the preparation of the mortar, we used standard sand (grain dimension of 0.08-2 *mm*) and a polycarboxylate superplasticizer (*PCs*) which is an indispensably admixture for cement composites: its main function is to reduce the water consumption without losing fluidity of the cement pastes.

Table 3.1. Typical chemical and physical properties of the cement used for mortar samples.

Mineralogical composition (% *bwoc*)		Oxide composition (% *bwoc*)	
C_3S (monoclinic form)	66.6	SiO_2	19.86
βC_2S	8.6	Al_2O_3	4.7
C_3A (cubic form)	4.6	Fe_2O_3	2.5
C_3A (orthorhombic form)	3.0	CaO	62.1
C_4AF	7.2	MgO	3.9
CaO (free)	0.5	SO_3	3.4
MgO (periclase)	2.6	Na_2O	0.3
$Ca(OH)_2$ (portlandite)	0.6	K_2O	0.9
$CaSO_4 \cdot 2H_2O$ (gypsum)	2.3	TiO_2	2.3
$CaSO_4 \cdot 1/2H_2O$ (bassanite)	1.0	P_2O_5	0.1
$CaSO_4$ (anhydrite)	0.8	Mn_2O_3	0.1
$K_3Na(SO_4)_2$ (aftitalite)	1.6	SrO	0.1
K_2SO_4 (arcanite)	0.6	Cr	≤ 150 *ppm*
Tot.	100	Zn	≤ 200 *ppm*

Loss of ignition (*LOI*)	1.4 % *bwoc*
Insoluble residue	0.2 % *bwoc*
Clorides	≤ 0.05 % *bwoc*
Fineness (blaine)	5000 cm^2/g
Specific gravity	3.12 g/cm^3

3.2 Syntheses of *GO* and *GO-Jeffamine M600*

Aqueous solution of graphene oxide was prepared following the Hummer's method: in a three-necked flash were mixed together under magnetic stirring, 1 *g* of graphite, 0.5 *g* of sodium nitrate ($NaNO_3$) and 23 *mL* of concentrated sulfuric acid (H_2SO_4) obtaining a black slurry (Figure 3.3). After one hour, we added slowly and gradually, 3 *g* of potassium permanganate ($KMnO_4$) to the above solution while keeping the temperature less than $20°C$ using an ice bath to prevent overheating and explosion. The mixture was than maintained at $35°C$ under stirring for 12 and 24 hours to obtain *GO* samples with different content of oxygen (*GO 12h* and *GO 24h* respectively).
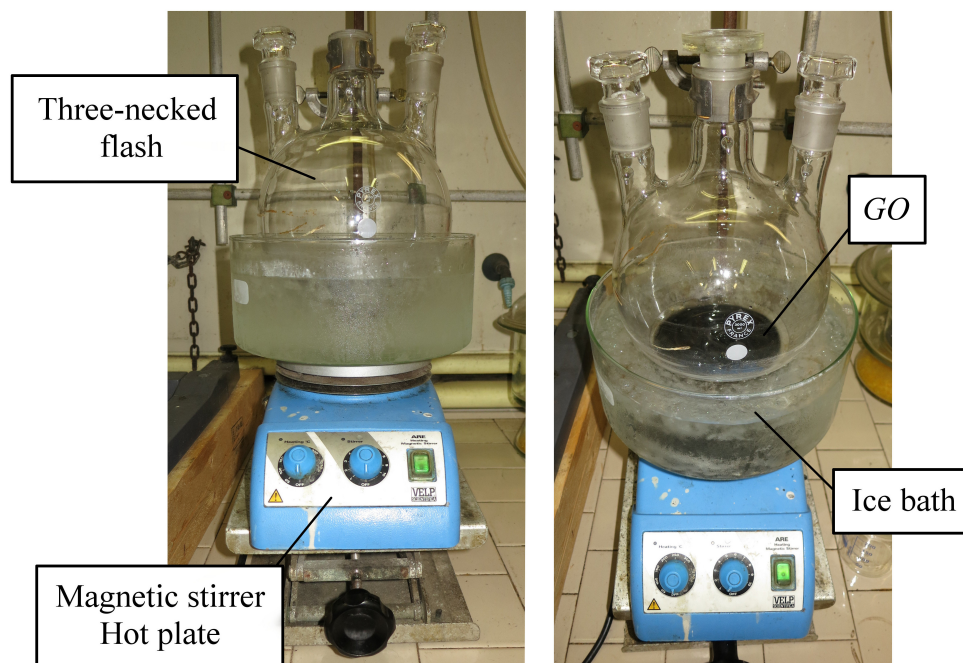
Figure 3.3. Instrumentation used for the synthesis of *GO*.

Finally, we diluted the solution by the addition of 500 *mL* of distilled water under vigorous stirring. To ensure the termination of the oxidation reaction, the solution was further treated with 5 *mL* of 30% of hydrogen peroxide solution (H_2O_2). After repeated centrifugations (15-20 times; 5000 *rpm* for 30 minutes each) and washing with distilled water, we controlled that the pH of the solution was nearly seven using a pH-meter, meaning that

we removed all the sulfuric acid. To be sure, we also performed the barium chloride (*BaCl$_2$*) test for sulfate ions: we diluted a part of our *GO* solution in water (need to be nearly transparent), added hydrochloric acid (some drops to ensure that we are in acidic environment) and methyl orange. The result is a pink solution in which we putted the barium chloride. If some sulfate ions were still in the solution, these would precipitate as barium sulfate. After the purification stage, to ensure the complete exfoliation of graphene oxide sheets we sonicated the solution for one hour and then part of the aqueous solution has been dried in an oven at 70°*C* for 24 hours which is enough to eliminate all the water but not to degraded the *GO*. What we obtain from this thermal treatment is a black film of graphene oxide that we used for the characterization and for the functionalization process.

For the reaction with the *Jeffamine M600* we putted in a three-necked flash 20 *mL* of *DMSO* which is the solvent of the reaction, 40 *mg* of solid graphene oxide and 9 g of *Jeffamine M600* and maintained the solution at 70°*C* for three days under stirring and under nitrogen. After that we added 0.135 *g* of *DMAP* and maintain the solution again under stirring and nitrogen for other three days. The Figure 3.4 reports reaction of functionalization that lead to the formation of an amidic bond. Once that the reaction is over, to allow the separation of the product we added 40 *mL* of acetone and then started the purification stage (filtering over paper filter with vacuum and washing with deionize water several time).
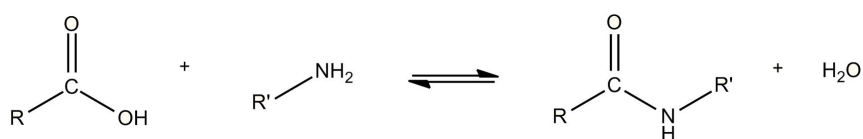
Figure 3.4. Condensation reaction and formation of the amidic bond.

After this stage, we putted the product in water solution for the storage and a part of it, has been dried in the oven at 70°*C* for 24 hours obtaining a black powder for the characterization.

3.3 Preparation of cement base composites sample

The preparations of the mortar composites specimens was carried out in a controlled environment, with a constant temperature ($20 \pm 2°C$) and constant relative humidity (not less than 50%) following the standard UNI EN 196-1 [93]. The cement powder, the water, the sand, the *PCs*, the *GO* solution and all the instrumentation must be located in the same conditions of temperature and humidity: must be thermostated for at least 24 hours before their use. The cement composite was prepared by mixing 450 *g* of cement, 1350 *g* of standard sand, 207 *g* of water, 0.8 *g* of *PCs* and different amount of *GO*. We prepared two different aqueous solution of *GO*: solution 1, which contained *GO 24h*, and solution 2 made of *GO 12h*. In Table 3.2 are reported the *GO* dosage and the different maturation time of the cement base composites samples.

Table 3.2. *GO* dosage in the mortar samples and maturation time for the specimens.

GO dosage (% *bwoc*)				Maturation time (days)		
0.02	0.04	0.06		3	7	28

Once we prepared and weighted all the component of the composites, we can proceed with the packaging of the samples following the UNI EN 196-1 standard. Firstly, we drop the standard sand in the in the hopper of the mixer and then pour the water with the additive (*GO* and *PCs*) and the cement into the tray, immediately after installing the bowl and blade to the mixer (Figure 3.5). Now we can start the cycle of mixing:

- first stage characterized by mixing at slow speed for 30 *s* after which we introduce the sand and mixed slowly for other 30 *s*;

- second stage of maximum speed for 30 *s*;

- last stage of mixing at maximum speed for 60 *s*.

Once obtained the mixture, we molded the paste into a rectangle box with a size of 40 *mm* x 40 *mm* x 160 *mm* (Figure 3.6) to obtained the specimens for the flexural and compressive test. Three samples were prepared for each measuring.
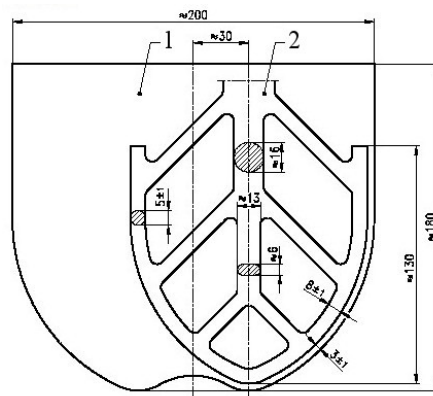
Figure 3.5. Tray (1) and the blade (2) of the mixer. Dimension indicated in *mm* [93].
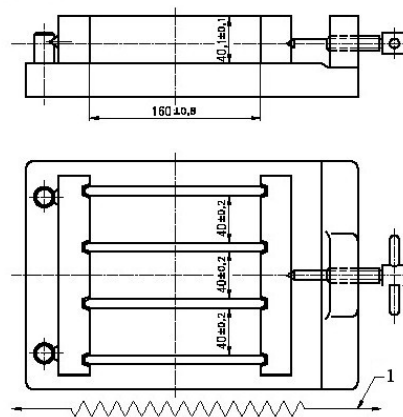
Figure 3.6. Mold used for the preparation of the specimen and is indicated the (1) metal ruler. Dimension indicated in *mm* [93].

Firstly, the mold were half fill and then we let the paste to settle. After that, we filled the entire mold, removed the excess mortar with a metal ruler, smoothed the surface and then we covered the mold with a metal plate suitably labeled for the recognition of the different samples. Now the molds containing the specimens are placed in an environment with a controlled humidity (*RU* of 100%) for 24 hours after which we remove the armor of the mold. In our study, we performed compressive and flexural test after 3, 7 and 28 day of maturation. After the mechanical characterization, we pulverized the sample and putted in acetone to stop the maturation of the hydration products.

3.4 Characterization of *GO* and *GO-JeffamineM600*

Graphene oxide and graphene oxide functionalized with *Jeffamine M600* were characterized using several methods such as *XRD*, *TGA*, compositional analysis, Infrared and Raman spectroscopy. We also performed Transmission Electron Microscopy imaging and electron diffraction.

3.4.1 Infrared and Raman Analyses

Infrared and Raman spectroscopy are fast and non-destructive characterization methods that unlike other techniques, does not require any sample preparation or specific substrates. These spectroscopic techniques are based on the radiation-matter interaction: Raman deals with scattering process of monochromatic light (laser) in the visible region of electromagnetic spectrum (*EMS*); *IR* spectroscopy concerns absorption of radiation in the infrared region of the *EMS*. In general, the vibrational spectrum, gives information at molecular level of the functional groups that are present in the sample. In our case we used the *FT-IR* spectroscopy to gain information about the specific oxygen group formed during the oxidation stage of graphite and to control if the purification stage was well performed. *FT-IR* spectra of *GO* and *GO-Jeffamine M600* samples were recorded using two different configuration: in transmission mode with Diamond Anvil Cell (*DAC*), and for some samples in specular reflection configuration using gold as reflection reference (Figure 3.7). We decide to used the *DAC* for the transmission mode, instead of *KBr* pellets, to eliminates the possible interference of water and of humidity.
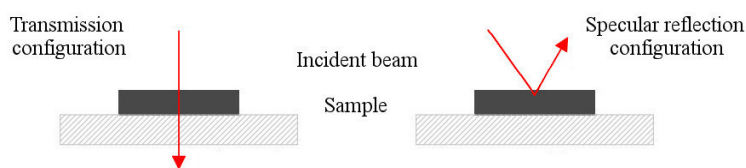
Figure 3.7. Different configuration used for the *FT-IR* spectra.

In the first condition (absorption spectra), we obtain information about the bulk of the sample, instead in specular reflection, we took information about the changes of the refraction index (*n*) of the system from a region close to the surface. The spectra obtained with these two different config-

uration are different and not comparable each other, unless we apply the Kramers-Kroning relation (*KK* spectra) which convert the spectra obtained in specular reflection, in units comparable to the absorbance. *FT-IR* spectra of *GO* and *GO-Jeffamine* samples were recorded on a FT-IR Nexus Nicolet coupled with a Microscope Continu*µm* Thermo Electronic Component (Figure 3.8) using a Diamond Anvil Cell (*DAC*) for the transmission configuration. All the *FT-IR* spectra reported in this work have been baseline corrected and normalized to the *C=O* vibrational band that seems stable for all the analyses condition.

Figure 3.8. *FT-IR* instrumentation with the Diamond Anvil Cell used for the analyses.

Raman spectra were recorded by using a Horiba Jobin Yvone Labram HR800 dispersive Raman spectrometer equipped with Olympus BX41 microscope and a 50X objective (Figure 3.9). We used an Ar^+ laser at 514.15 *nm* which was kept at 2 *mW* in order to prevent possible degradation of the samples. The spectra were obtained as the average of 4 acquisition, with a scan time of 20 second for each one and a spectral resolution of 2 cm^{-1}.
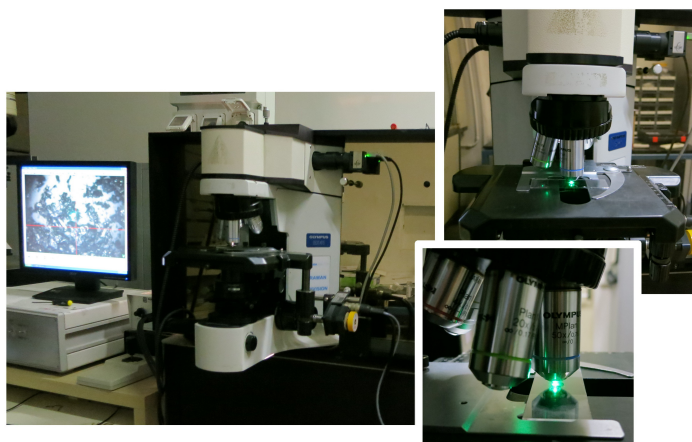
Figure 3.9. Raman instrumentation used for the analyses.

3.4.2 Compositional Analyses

Inductively Coupled Plasma Optical Emission Spectrometry

For the detection of trace metals, we performed an Inductively Coupled Plasma Optical Emission Spectrometry (*ICP-OES*) which is a type of emission spectroscopy that uses the inductively coupled plasma to produce excited atoms and ions that emit electromagnetic radiation at wavelengths characteristic of a particular element. The intensity of this emission is indicative of the concentration of that element within the sample.

In our case, we used an *ICP-OES* Perkin Elmer, Mod. Optimia 7000 DV (Figure 3.10) to detect the amount of Sodium (*Na*), Potassium (*K*) and Manganese (*Mn*) that could remain in our product after the purification stage. To do so the sample must be prepared to ensure the complete depletion of the organic part (mineralization or digestion process): we putted the solid sample of *GO* in a beaker over a hot plate with a mixture 1:1 of sulfuric ($\geq 95 - 97\%$, Sigma-Aldrich) and nitric acid ($\geq 65\%$, Sigma-Aldrich). The first one is a very strong oxidant agent and the second one is used to break all the chemical bonds allowing the mineralization process. As the system started to boil, we added more nitric acid until the black sludge became a transparent light yellow liquid.

Figure 3.10. *ICP-OES* instrumentation used.

Once obtained these kind of specimens we performed the *ICP-OES* analyses using:

- - two different water solution as reference for the sulfuric (5% H_2SO_4) and nitric acid (5% HNO_3);

- - three different standard solution with different concentration (0.5 *ppm*, 1 *ppm*, 2 *ppm*) for each metal that we want to detect (Multielement standard solution 1 for *ICP*, Fluka Analytical).

Elemental Analysis

We also performed a C H N S elemental analysis using an elemental analyzer Costech ECS. Mod. 4010. These instrument allows us to obtain contemporary the amount of *C*, *H*, *N*, *S* and for difference the amount of oxygen present in the samples.

3.4.3 X-Ray Diffraction Analyses

X-ray diffraction analysis is used for the identification of the atomic and molecular structure of a crystal: an X-ray beam collide with the sample and due to the presence of the atoms in a regular array, the beams is

diffracted in many specific direction. By measuring the angles and the intensities of these diffracted beams, we can obtain information about the crystallographic structure of the specimens. Using this technique we obtained information about the distance between the different sheets of graphite and graphene oxide using the Bragg's law (Figure 3.11) where n is the diffraction order, λ is the wavelength of the incident radiation, d is the distance between two adjacent plane and θ is the incident angle. We collect *XRD* data using a Bruker D8 Advance X-ray diffractometer (Figure 3.11) with monochromatic *CuKα* radiation ($\lambda = 1.5406\ \text{Å}$) at $25°C$ from $3°$ to $40°$, with a scan step of $0.020°$ and a step time of $1.2\ s$.
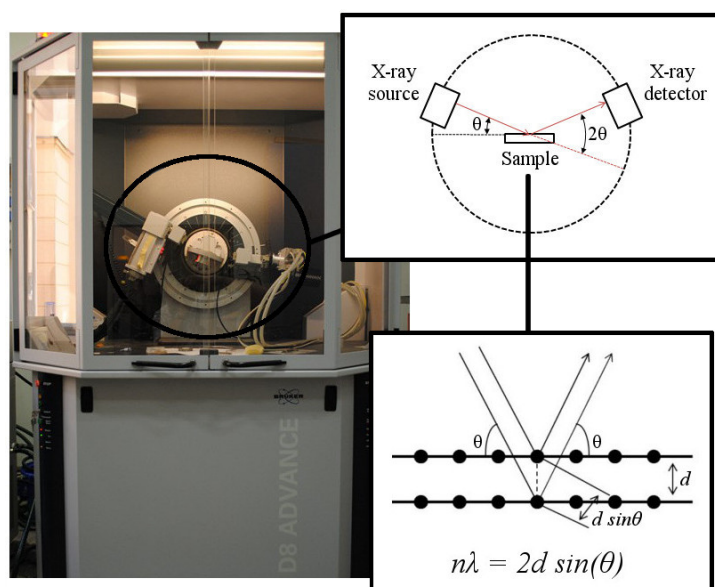
Figure 3.11. Bruker D8 Advance X-ray diffractometer.

3.4.4 Thermogravimetric Analyses

The Thermogravimetric Analysis (*TGA*) is a destructive method in which changes in physical and chemical properties of the materials, such as weight loss, are measured as a function of increasing temperature with constant heating rate. *TGA* can provide information about different chemical phenomena including chemisorption, desolvation (especially dehydration), decomposition, combustion and solid-gas reactions (oxidation, reduction, nitruration, etc.). In our specific case we used a Seiko Exstar 6000 TG/DTA

6300 thermal analyzer with two alumina (Al_2O_3) melting pots: one used as reference and one loaded with some *mg* of the samples (Figure 3.12).
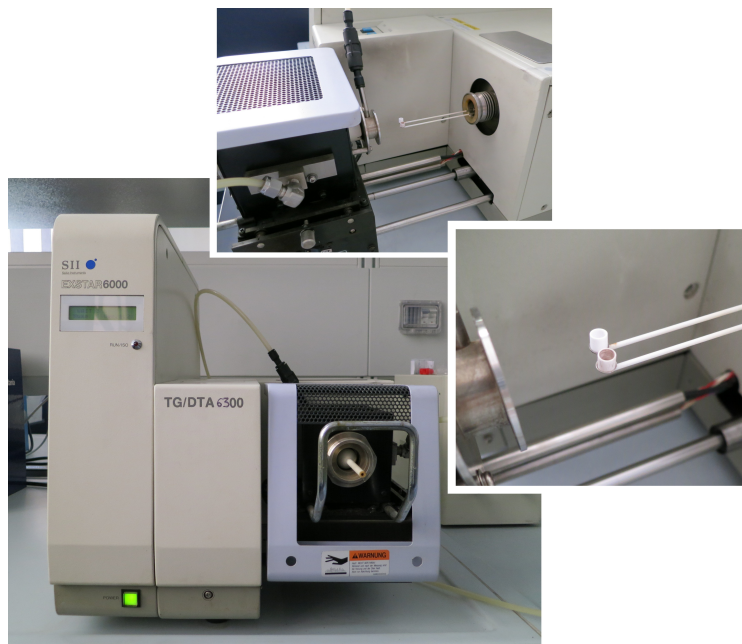
Figure 3.12. Thermogravimetric analyzer and alumina melting pots used.

For each specimen we performed the same analyses in air and under nitrogen, starting from $25°C$ to $800°C$ with constant heating rate ($10°C/min$).

3.4.5   Transmission Electron Microscopy with Selected Area Electron Diffraction

Transmission Electron Microscopy

Transmission Electron Microscopy (*TEM*) is a microscopy technique in which a beam of electrons is transmitted through an ultra-thin specimen and an image is formed from the interaction of the electrons transmitted through the specimen itself. We performed these analyses using a CM200 Field Emission Gun using an operating voltage of 200 *kV* (Figure 3.13). The samples were prepared depositing a drop of *GO* solution on a copper grid (200 mesh) with holey carbon films deposited over it. To ensure the total evaporation of the water we waited one night after the drop deposition before making the analyses.

Figure 3.13. Transmission electron microscopy used.

Selected Area Electron Diffraction

Using the same samples and instrumentation used for the *TEM* analyses, we performed a Selected Area Electron Diffraction (*SAED*) which is a crystallographic experimental technique that can be performed inside a *TEM*. The electrons are treated as wave-like and the atoms of the sample act as a diffraction grating to the electrons beam which, in part is diffracted/scattered to particular angles determinate by the crystal structure and the remain continue, passing through the sample. As a result, the *SAED* patterns are characterized by a series of spots, each one corresponding to a satisfied diffraction condition of the samples crystal structure.

3.5 Characterization of cement base composites

3.5.1 Mechanical Characterization

For the test of bending resistance, we use the three-point configuration reporter in Figure 3.14: the faces of the specimen subjected to load must be those, which have been in direct contact with the mold, to ensure flatness and parallelism. During flexion, the specimens are broken into two halves and for each specimen the dynamometer returns a value of mechanical strength in *MPa*.
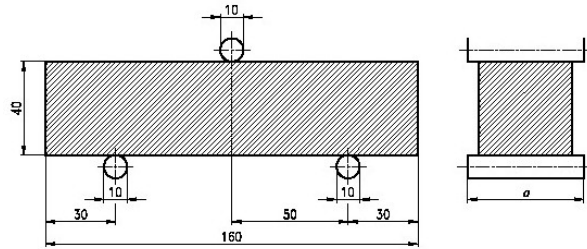
Figure 3.14. Three-points bending test. Dimension indicated in *mm* [93].

The flexural strength (R_f) is returned by the dynamometer using the relationship reported in the following equation were:

$$R_f = \frac{1,2 \cdot F_f \cdot l}{b^3} \tag{3.1}$$

- b is the length of the square section of the specimen (*mm*);

- l the distance between the supports (*mm*);

- F_f the breaking load applied to the center of the specimens (*N*).

For the determination of the compressive strength, we use half of the broken specimen during the previous test. Even in this case the faces of the specimen subjected to load must be those, which were in contact with the metal of the mold, to ensure flatness and parallelism. Similarly, to the first test, once reached the breaking load the dynamometer returns the values of mechanical strength in *MPa*. We obtained the compressive strength (R_c) according to the equation reported below in which:

$$R_c = \frac{F_c}{1600} \tag{3.2}$$

- F_c is the maximum load reached (*N*);

- 1600 is the area (*mm²*) of the plates over which we applied the load to the specimen (40 *mm* x 40 *mm*).

In the Figure 3.15 we report the instrumentation used. We can identify: (1) ball bearings, (2) sliding assembly, (3) a return spring (4) spherical support of the machine, (5) top plate of the machine, (6) spherical support of the press, (7) upper plate of the press, (8) prismatic specimen, (9) lower plate of the instrument, (10) lower plate of the press and (11) the lower plate of the machine.
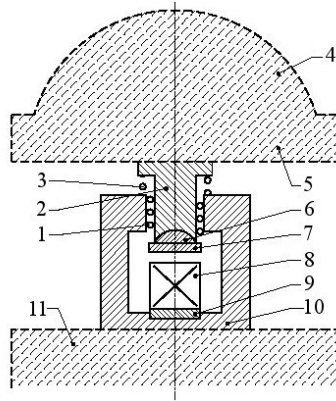
Figure 3.15. Instrumentation used for the compressive test. Dimension indicated in *mm* [93].

3.5.2 Scanning Electron Microscopy with Energy Dispersive Spectroscopy

Scanning Electron Microscopy

A Scanning Electron Microscope (*SEM*) is a type of electron microscope that produces images of a sample by a focused beam of electrons. The electrons interact with atoms in the sample, producing various signals that can be detected and that contain information about the sample's morphology and composition. In our case we observed the morphology of the hydration products of hardened mortar using a SEM Zeiss EVO 50 EP (extended pressure) equipped with a Lanthanum Hexaboride (*LaB₆*) crystal (Figure 3.16). We collected both secondary electrons and backscattered

electrons, depending on the samples, using two different detectors. In each *SEM* images, we indicated the operating condition (current, pressure, etc.) and the kind of detector used (*SE1* for secondary electron and *QBSD* for the backscattered electrons). The pulverized mortar is metalized to an aluminum stub using a graphite adhesive and that putted in the chamber of the *SEM* for the analyses.
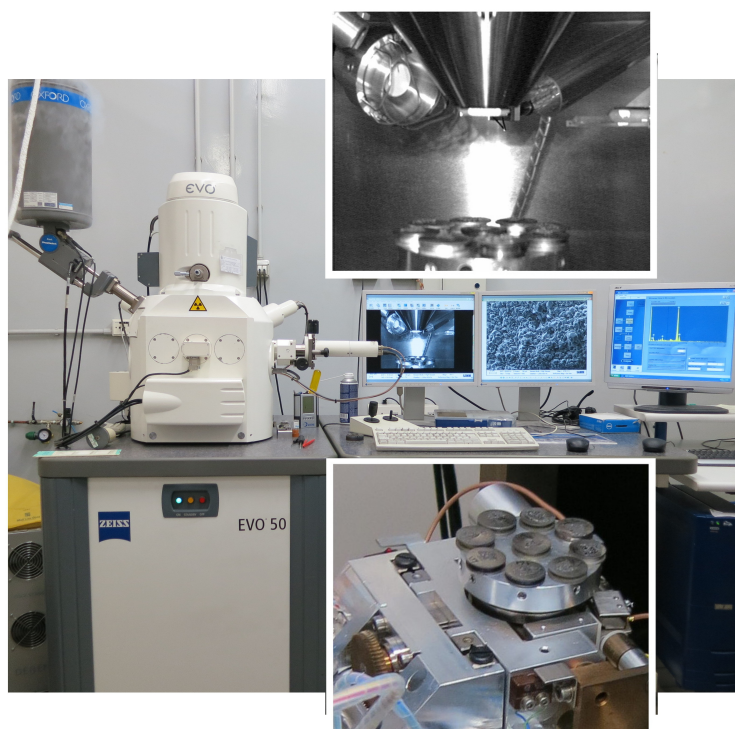
Figure 3.16. Scanning Electron Microscope used.

Energy Dispersive Spectroscopy

Energy Dispersive Spectroscopy (*EDS*) is an analytical technique used for the elemental analysis or chemical characterization of a sample. We used the *EDS* to obtain the distribution of carbon in our samples, to control although if the *GO* sheets are homogeneously dispersed in the mortar matrix.

Chapter 4

Results and discussion

In the first section of this Chapter, we report the analyses done on the graphene oxide synthesized following the process described in the Chapter 3. In particular, we report the Infrared and Raman spectra, compositional analyses, *TGA*, *TEM* images, *XRD* and *SAED* patterns. Once the *GO* has been characterized we performed the functionalization with the *Jeffamine M600* and in the second part of this Chapter we report the analyses done on these samples (*IR* spectra and *TGA*). The two different specimens (*GO* and *GO-Jeffamine M600*) will be compared and an explanation of the different properties of them will be provided. In the third part, we discuss the result of the mechanical and morphological characterization (*SEM* images) of the cement base composites.

4.1   Graphene Oxide characterization

4.1.1   Infrared spectroscopy: graphene oxide markers bands

First of all, we recorded the *FT-IR* spectrum of the raw graphite used for the oxidation: in this case, it was impossible to obtain the spectrum in transmission configuration because the surfaces of the specimens, pressed inside the Diamond Anvil Cell, were very bright and reflective so the *IR* radiation was not transmitted through it. This means that it was necessary to use the specular reflection configuration. The spectrum obtained in specular reflection can be transformed in units comparable to the absorbance using the Kramer-Kronig relation (*KK*).

The spectrum recorded (blue line) and the *KK* transformed (red line) are reported in Figure 4.1, only two spectral features can be observed at:

- 1590 cm^{-1} which is the characteristic peak of graphite and graphene materials assigned to E_{iu} *IR* active mode of collective *CC* stretching vibration [94];

- 2350 cm^{-1} due to the CO_2 in the air.
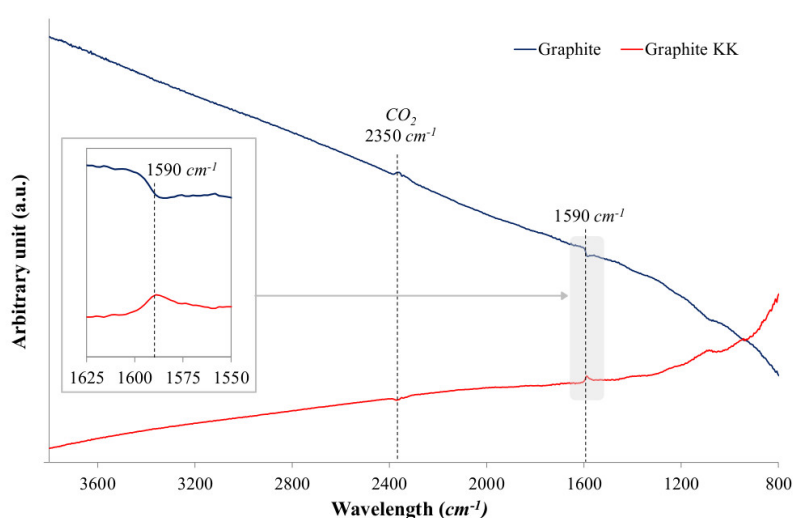
Figure 4.1. *FT-IR* spectra of raw graphite obtained in specular reflection (blue line) and the transformed one with the Kramer-Kronig relation (red line).

Once obtained the graphene oxide (*GO*) in water solution we observed that the majority of *GO* tends to separate at the bottom of the beaker and the other remain in solution. We withdrawn two sample from the same batch, one from the segregated material (*GO DOWN*) and one from the supernatant (*GO UP*) and made *FT-IR* analyses for each one in transmission configuration. At first, we supposed that the segregated part was mainly composed by the non-reacted graphite platelets that did not remain in solution.

However, observing the Figure 4.2 we rejected this hypothesis: the two spectra shown very similar spectral patterns with some differences in the relative intensities of some bands.
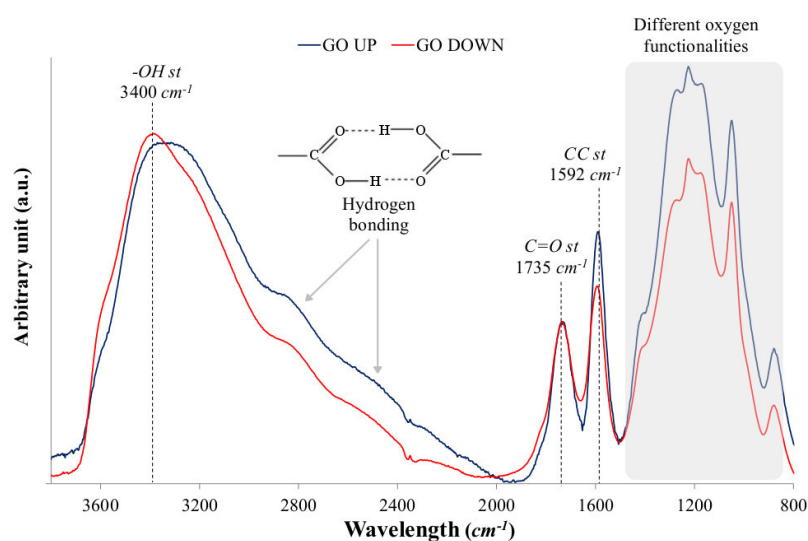
Figure 4.2. *FT-IR* spectra of *GO DOWN* and *GO UP*.

In particular, we are able to identify peaks for both samples at:

- the strong and broad absorption of 3400 cm^{-1} due to -*OH* stretching modes of hydroxyl groups bonded on the carbon backbone;

- 2400 cm^{-1} and 2900 cm^{-1} two small and broad absorption that can be assigned to the presence of dimers of hydrogen bonded carboxyl groups;

- 1735 cm^{-1} *C=O* stretching of the carboxyl groups bonded on the edges of graphene sheets as reported in the Chapter 2;

- 1592 cm^{-1} associated to the *CC* stretching of the sp^2 carbon backbone;

- 1279 cm^{-1} and 880 cm^{-1} region where overlapped bands of *C-O-C* and *C-O* stretching are present, due to the oxygen functionalities bonded on the carbon backbone.

In Figure 4.3 is reported a magnification of the spectra between 800 cm^{-1} and 1500 cm^{-1} that allow to easily identifying the peaks of the different oxygen functionalities presents in the samples.

Now we can state that both the *GO DOWN* and *GO UP* are oxidized. The *GO UP* show higher relative intensity in the region between 800 cm^{-1}
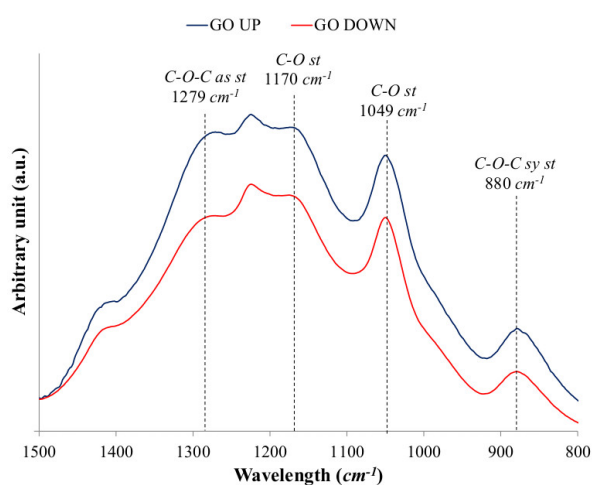
Figure 4.3. Magnification of a part of the *FT-IR* spectra of *GO DOWN* and *GO UP*.

and 1500 cm^{-1}, suggesting that this sample is characterized by an higher amount of oxygen functionalities with respect the *GO DOWN*. Indeed the *GO DOWN* platelets maybe be bigger and less exfoliated and tend to separate from the solution.

4.1.2 Infrared spectroscopy: stability of *GO* in water

One of our objectives was to investigate the stability of *GO* in water, because once the purification stage is over the materials remain in water solution for all the storage time. We left for two month at rest a part of the *GO* initial solution, from which we withdrawn the *GO UP* and *GO DOWN* samples, after which the solution appears more homogeneous. We withdrawn a specimen (*GO OLD*) from this batch and drying it for 24 *h* in the oven at 70°C before doing the *FT-IR* analysis. In Figure 4.4 are reported the *FT-IR* spectra of the *GO UP*, *GO DOWN* and *GO OLD*. At a first glance, the spectra seem to show similar patterns.

We identify peaks at:

- 3400 cm^{-1} assigned to -*OH* stretching;

- 2400 cm^{-1} and 2900 cm^{-1} dimers of hydrogen bonded carboxyl groups;
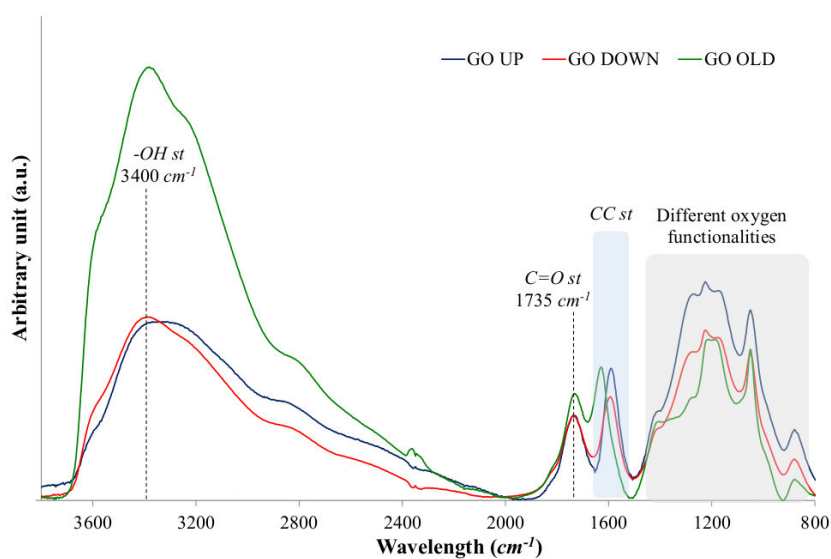
Figure 4.4. *FT-IR* spectra of *GO DOWN*, *GO UP* and *GO OLD*.

- 1735 cm^{-1} assigned to *C=O* stretching;

- 1638 cm^{-1} for the *GO OLD* and at 1592 cm^{-1} for both the *GO UP* and *DOWN* assigned to the *CC* stretching;

- peaks in the region between 800cm^{-1} and 1500 cm^{-1} of the oxygen functionalities (Figure 4.5).
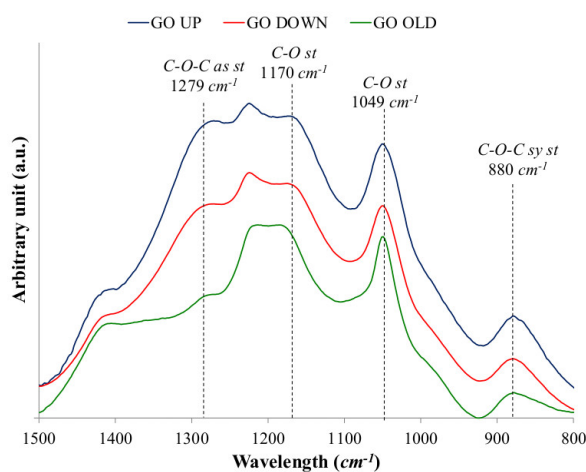
Figure 4.5. Magnification of parts of the *FT-IR* spectra of *GO DOWN*, *GO UP* and *GO OLD*.

Considering again the Figure 4.4 we can observe that the broaden peak at 3400 cm^{-1} is characterized by an higher relative intensity for the *GO OLD* with respect to the *GO UP* and *GO DOWN* samples suggesting that a certain amount of water has been adsorbed during the storage.

The most significant difference among the three spectra is related to the frequency of the *CC* stretching peaks: for *GO UP* and *GO DOWN* it is located at 1592 cm^{-1}, while for *GO OLD* it is blue shifted at 1628 cm^{-1}. A possible explanation of this behavior is that the water molecules adsorbed by the *GO* during the two month of storage, contribute with a strong *H-O-H* bending vibration near 1640 cm^{-1} that shadows the signal of the *CC* peak at 1592 cm^{-1}, still visible as a very weak shoulder (Figure 4.6).
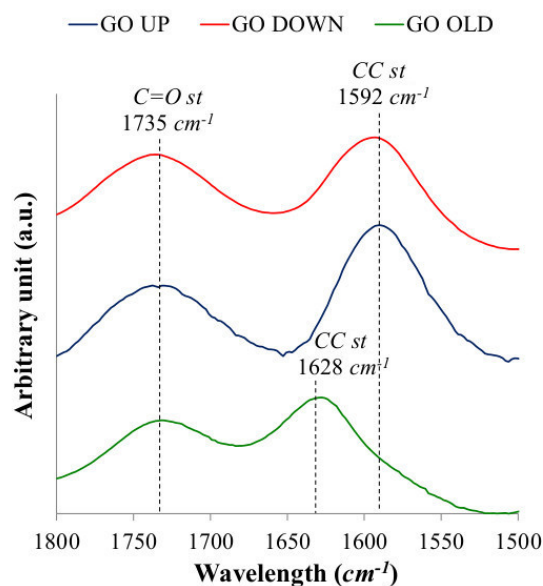
Figure 4.6. Magnification of parts of the *FT-IR* spectra of *GO DOWN, GO UP* and *GO OLD*.

To summarized, in Figure 4.7 are reported the *FT-IR* spectra of *GO UP, GO OLD* and water, which was collected as reference in our laboratory: it is clear, observing this spectra the effect of the storage in water on the *GO*.
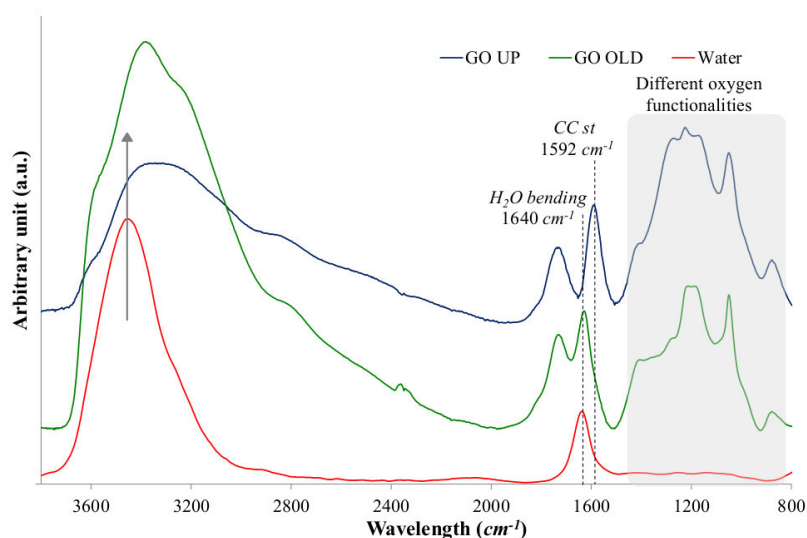
Figure 4.7. *FT-IR* spectra of *GO UP*, *GO OLD* and water.

From literature (Chapter 2) the water adsorbed can be eliminated applying thermal treatment on the *GO* causing also, for very high temperature a reduction of the samples, with the elimination of the oxygen groups. Starting from this, we performed *FT-IR* spectra on thermal treated *GO OLD* at $40°C$ (*GO 40*), $70°C$ (*GO 70*) and $140°C$ (*GO 140*), reported in Figure 4.8. It's clear that the *-OH* stretching at 3400 cm^{-1} band is progressively reduced in intensity as the applied temperature increase while the peak at 1735 cm^{-1} of the *C=O* stretching does not change. Another effect of the thermal treatment is evident from the Figure 4.9 which is a magnification between 800 cm^{-1} and 1800 cm^{-1} of the spectra reported before. The *GO OLD*, *GO 40* and *GO 70* are characterized by the same spectral pattern meaning that for temperature lower that $70°C$ the oxygen functionalities are nearly stable and the *GO* is not reduced. On the contrary the spectrum of the *GO* treated at $140°C$ shows a very different spectral pattern with respect the others, characterized by only two strong peaks are at 1590 cm^{-1} and 1240 cm^{-1}. All the peaks associated to the oxygen functionalities disappeared, or are characterized by weak signals submerged by the strong peak at 1240 cm^{-1}. The key point is to understand the evolution of the peaks in the *CC* stretching region. Considering the Figure 4.9 we can observe that the *CC* peak for *GO OLD*, *GO 40* and *GO 70* is composed mainly by two contributions: one is the peak associated to the water at 1640 cm^{-1} and the

other is the real *CC* stretching at 1590 cm^{-1}. As the temperature increase the water evaporate reducing the relative intensity of the H_2O bending peak making the *CC* one, more evident.
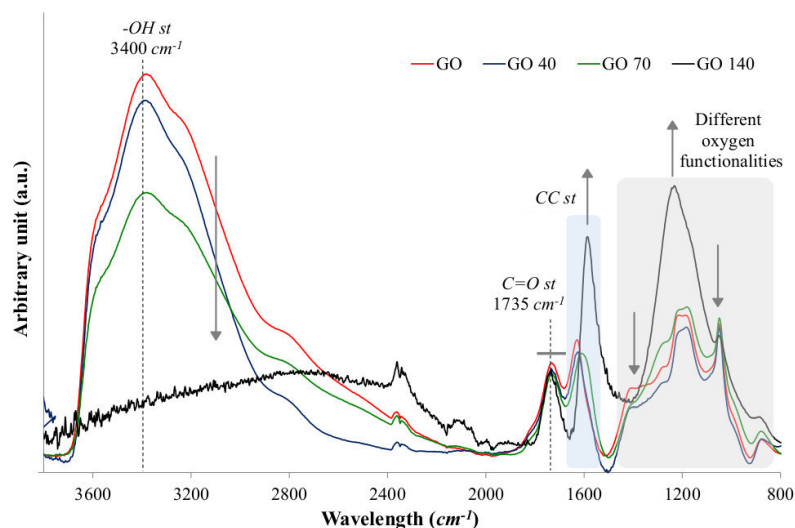
Figure 4.8. *FT-IR* spectra of *GO OLD* and the *GO* thermal treated at $40°C$, $70°C$ and $140°C$.
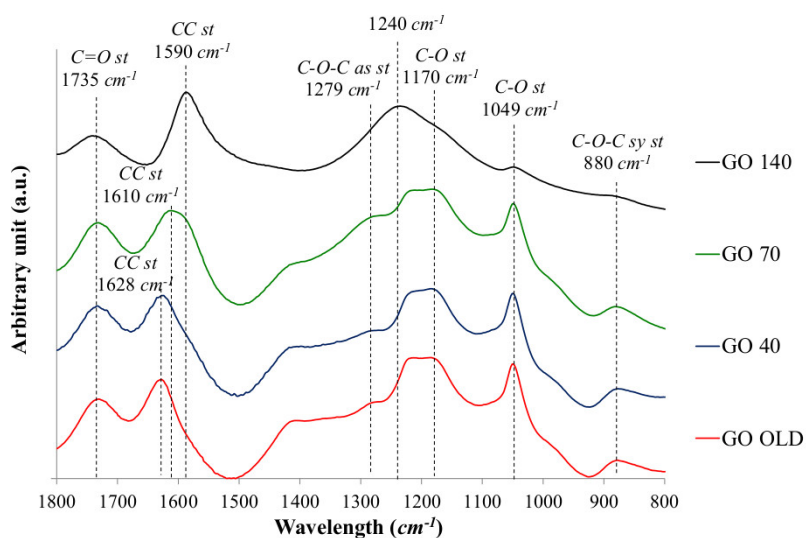
Figure 4.9. Magnification of a part of the *FT-IR* spectra of *GO OLD*, *GO 40*, *GO 70* and *GO 140*.

The bigger differences observed in the *GO 140* spectrum can be attributed to the effect of the reduction: elimination of the oxygen functionality and a partial reconstruction of the sp^2 carbon backbone. This could explain the presence of the two strong bands at 1590 cm^{-1} and 1240 cm^{-1} of the *GO 140* assigned to the *G* and *D* peaks respectively, *IR* activated by the presence of the *C=O* group that polarized the partially reconstructed sp^2 carbon backbone (Figure 4.10).
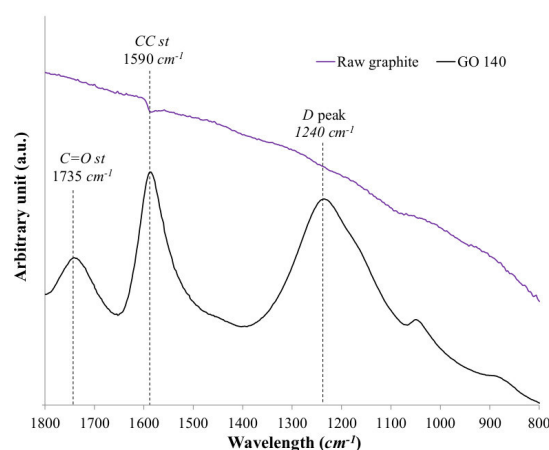
Figure 4.10. Magnification of a part of the *FT-IR* spectra of *GO 140* and of the raw graphite.

4.1.3 Infrared spectroscopy: different oxidation time

The specimens analyzed till now are all obtained following the procedure described in the Paragraph 3.2, considering a time of oxidation of 24 hours (*GO UP*, *GO OLD*, etc.), but we also performed a synthesis with an oxidation stage of 12 hours (*GO 12h*). We expected to see some difference in the oxygen functionalities between the *GO 12h* and the *GO OLD* sample.

The Figure 4.11 reports the *GO OLD* and the *GO 12h* spectra in this case we can find:

- similar *-OH* stretching peak at 3400 cm^{-1};

- the same *C=O* stretching peak at 1735 cm^{-1} and *CC* stretching at 1590 cm^{-1};

- different relative intensity of the peaks between 800 cm^{-1} and 1500 cm^{-1}

(see Figure 4.12) associated to the different oxygen functionalities as expected.

This confirm that the time of oxidation rules the formation of different oxygen groups, allowing the possibility to control the oxidation of the graphite in order to change the properties of graphene oxide.
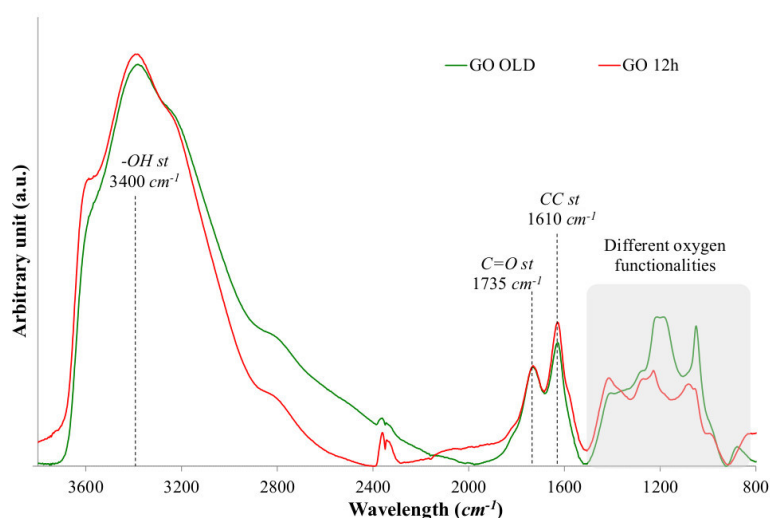
Figure 4.11. *FT-IR* spectra of *GO OLD* and *GO 12h*.
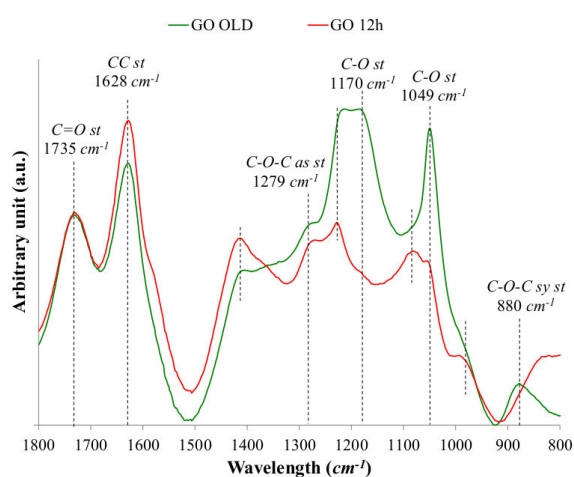
Figure 4.12. Magnification of two parts of the *FT-IR* spectra of *GO OLD* and *GO 12h*.

4.1.4 Raman spectroscopy

Raman spectroscopy has become a powerful non-invasive method to characterize graphite, graphene and related materials such as the graphene oxide. All the Raman spectra reported are obtained using a Laser source of 514.5 *nm* and 2 *mW* of power. First, we collected the Raman spectrum of the raw graphite (Figure 4.13). We can identify:

- the strong and sharp *G* peak at 1583 cm^{-1} due to a collective *CC* stretching vibration of crystalline graphite;

- a very weak *D* peak at 1362 cm^{-1} which is Raman active only in presence of edges and/or defect of the sp^2 carbon system and is associated to a collective breathing mode of the aromatic rings;

- a shoulder assigned to *D'* peak at 1610 cm^{-1} due to the presence of edges;

- the *2D* peaks at 2725 cm^{-1} and 2693 cm^{-1} due to first overtone of *D* vibration;

- the *2G* peak 3246 cm^{-1}.
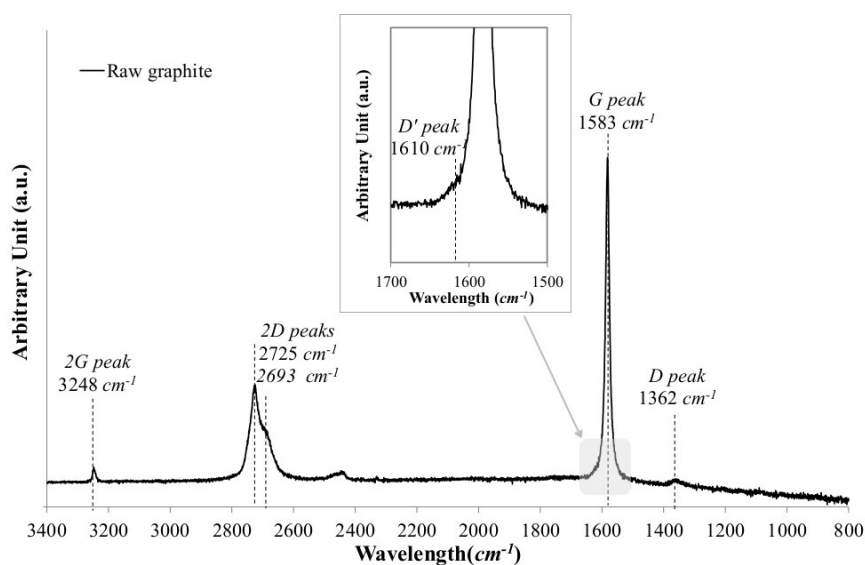
Figure 4.13. Raman spectrum of the raw graphite.

In Figure 4.14 are reported the Raman spectra of the *GO OLD* compared to one of the raw graphite. The characteristic peaks of graphene oxide are:

- a broad *G* peak at 1610 cm^{-1};

- a broad *D* peak at 1362 cm^{-1};

- very weak *2D* peaks at 2725 cm^{-1} and 2693 cm^{-1}.

As reported by Ferrari [71] the disorder in graphitic materials can be monitored with the *D* peak and with the intensity ratio between the *D* and *G* peak (I_D/I_G): as the disorder increase the ratio I_D/I_G increases.
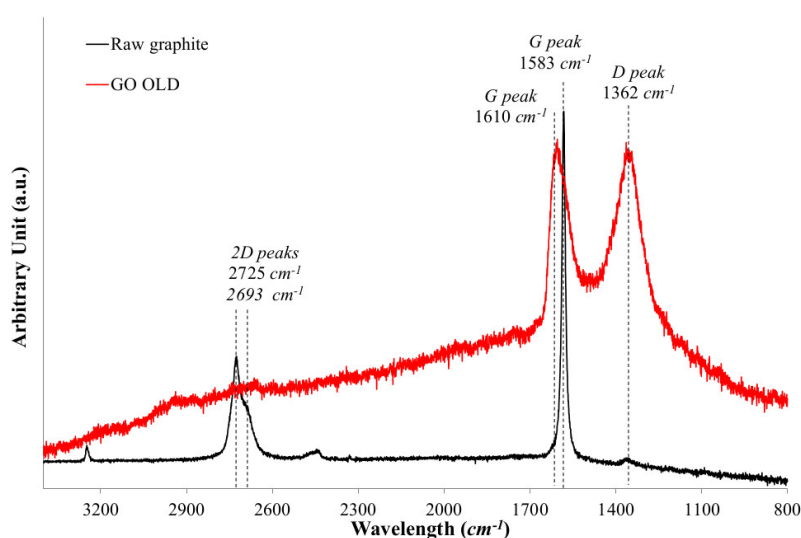
Figure 4.14. Raman spectra of the raw graphite and the *GO OLD*.

It's clear, observing the Figure 4.14, that the I_D/I_G ratio is higher for the *GO* sample respect the one of the starting graphite: this means that the oxidation of graphite produces an highly disordered sp^2 carbon system.

In Figure 4.15 are reported the Raman spectra of the *GO OLD* and of the specimens treated thermally (*GO 40*, *GO 70* and *GO 140*). The characteristic spectral pattern remain the same and we can identify:

- a broad *G* peak at 1610 cm^{-1};

- a broad *D* peak at 1362 cm^{-1};

- the peak at 2950 cm^{-1} which is the combination level of the *D* and *G* peaks;

- the overtone of the *D* and *G* peaks respectively at 2723 cm^{-1} and at 3200 cm^{-1}.
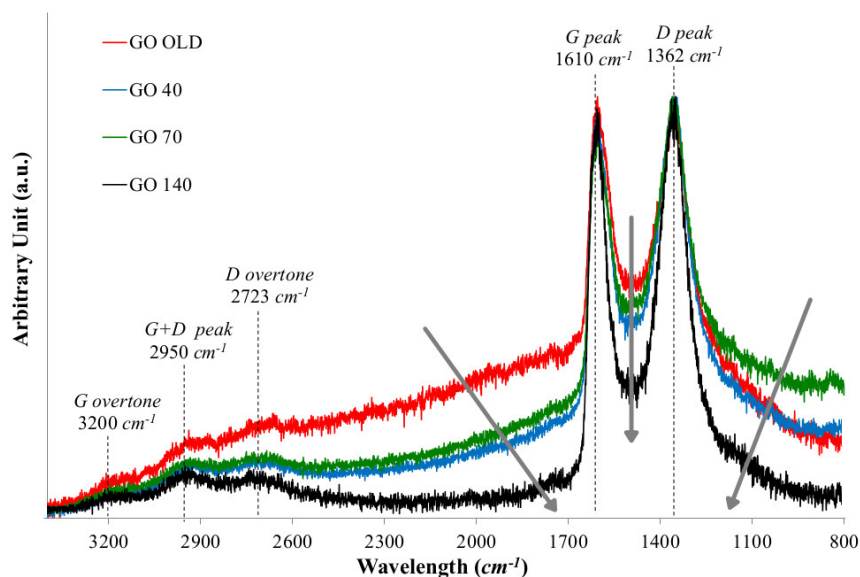
Figure 4.15. Raman spectra of the *GO OLD*, *GO 40*, *GO 70* and *GO 140*.

The effects of the thermal treatments are the progressively lowering of the base line and a decreases of the Raman signal placed between the *D* and the *G* peaks, which is associated to amorphous sp^3 carbon structures [95]. The Raman spectra of the *GO OLD* and *GO 140*, after the baseline correction, reported in the Figure 4.16, show that: the broad component of the Raman signal between *D* and *G* lines is reduced by the thermal treatment and the *G* peak becomes sharper for the *GO 140*. This observation suggests that reduction processes preferentially starts on the sp^3 carbon fraction of the *GO* promoting a partial reconstruction of the sp^2 carbon system. Indeed the I_D/I_G ratios turns out to be 1.59 and 1.41 for GO OLD and GO 140 reflectively.

In Figure 4.17 we reported the Raman spectra of the *GO OLD* and *GO 12h* to show the effect of the oxidation time on the carbon backbone.

Some differences can be observed on the shape of the *G* and *D* peaks, suggesting that both the oxygen functionalities (as demonstrated by the infrared measure, Paragraph 4.1.3) and the carbon structure are influenced by the time of oxidation. Further study must be performed to better characterize this behavior.
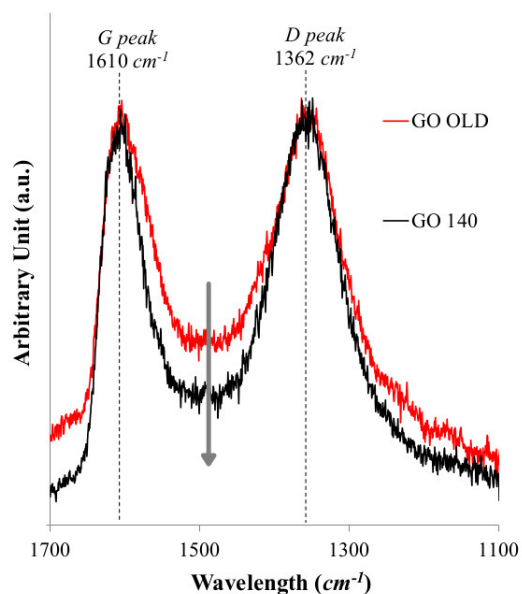
Figure 4.16. Raman spectra of the *GO OLD* and *GO 140*.
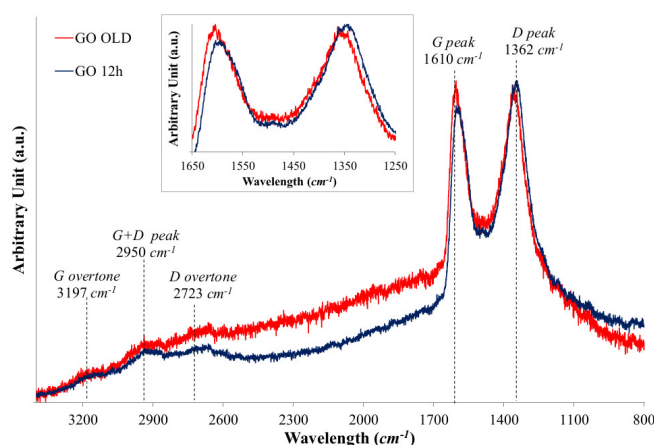
Figure 4.17. Magnification of the Raman spectra of the *GO OLD* and *GO 12h*.

4.1.5 Compositional analyses

To control the proportion of carbon and oxygen present in the *GO* sample we performed elemental analyses as described in the Paragraph 3.4.2. We analyzed three sample obtained with the same procedure:

- two sample obtained after 24 hours of oxidation time (*GO 24h 1* and *GO 24h 2*);

- the third obtained considering an oxidation time of 12 hours (*GO 12h*).

In Table 4.1 the obtained values are reported: the content of *C* element in the *GO* sheet was between 41 and 49%, depending on the samples.

Table 4.1. Elemental analyses performed on three different sample.

Sample	*C*		*H*		*N*		*S*		*O*
	%wt.	dev%	*%wt.*	dev%	*%wt.*	dev%	*%wt.*	dev%	% *wt.*
GO 24h 1	44.32	±0.5	1.69	±0.1	0.28	±0.05	//	//	53.71
GO 24h 2	41.95	±0.5	1.87	±0.1	0.22	±0.05	1.58	±0.1	54.38
GO 12h	49.8	±0.5	1.3	±0.1	//	//	//	//	48.9

Considering the Table 4.1 we are also able to asses that the kinetic of the oxidation reaction is very quickly, in fact we obtain only 5% less oxygen in the *GO 12h* respect the other two sample, i.e. halving the reaction time. The presence of a little amount of nitrogen is due to the sodium nitrate used in the synthesis and the sulfur content in the *GO 24h 2* is due to a not complete elimination of the sulfuric acid during the purification stage.

To control the amount of residual metal remain in solution, we performed an *ICP-OES* analyses and the result are reported in Table 4.2

Table 4.2. Residual metal present in the sample, obtained with *ICP-OES* analyses.

Potassium (*K*)	Sodium (*Na*)	Manganese (*Mn*)
3600 *ppm*	70 *ppm*	720 *ppm*

The amount of residual metal is not so high to persuade us to continue the washing process.

4.1.6 *XRD* analyses

We performed the *XRD* analyses to determine the average crystalline properties of the graphene oxide. In Figure 4.18 are reported the *XRD* pattern obtained for the graphite powder, *GO UP* and *GO DOWN*.
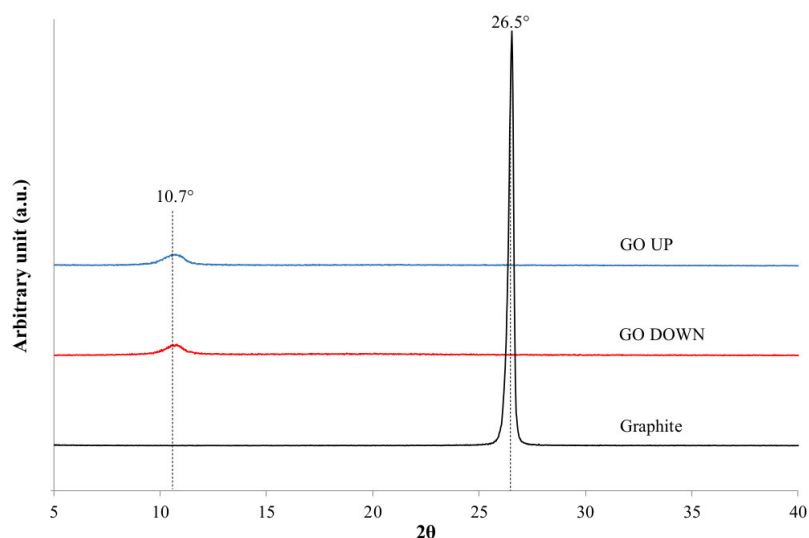
Figure 4.18. *XRD* patterns of the raw graphite, the *GO DOWN* and the *GO UP*.

The *XRD* pattern of the raw graphite show a very strong peak at 26.5° which is typical of the graphitic structure with a layer spacing of 3.4 $\mathring{A}$. After the oxidation, this peak disappears and a new one appears at 10.7°, in accordance with the literature, for both the samples, meaning that the interlayer distance increase (nearly 8.1 $\mathring{A}$) and the structure is modified due to the appearance of oxygen containing functional group upon the oxidation process. In Figure 4.19 is reported the same *XRD* pattern of Figure 4.18, related to the *GO UP* and the *GO DOWN*: the presence of a small amount of diffuse scattering implying the onset of a coexistent amorphous phase of *GO*. In Figure 4.20 are reported the *XRD* pattern of several specimens: the raw graphite, *GO DOWN* and the graphene oxide treated thermally with different temperature: 40°*C*, 70°*C* and 140°*C*. The peaks at 10.7° does not change even if at high temperature meaning that the system does not undergoes the complete reduction, in fact the graphitic peak at 26.5° is not present.
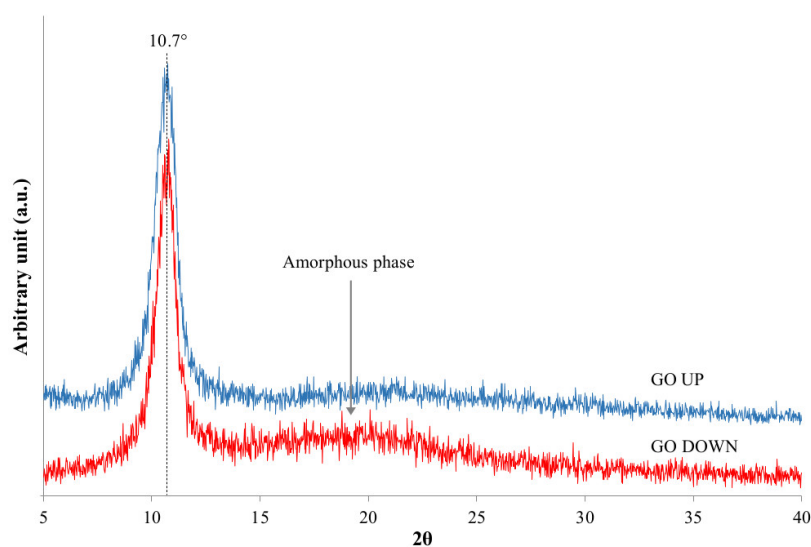
Figure 4.19. *XRD* patterns of the *GO DOWN* and the *GO UP*.
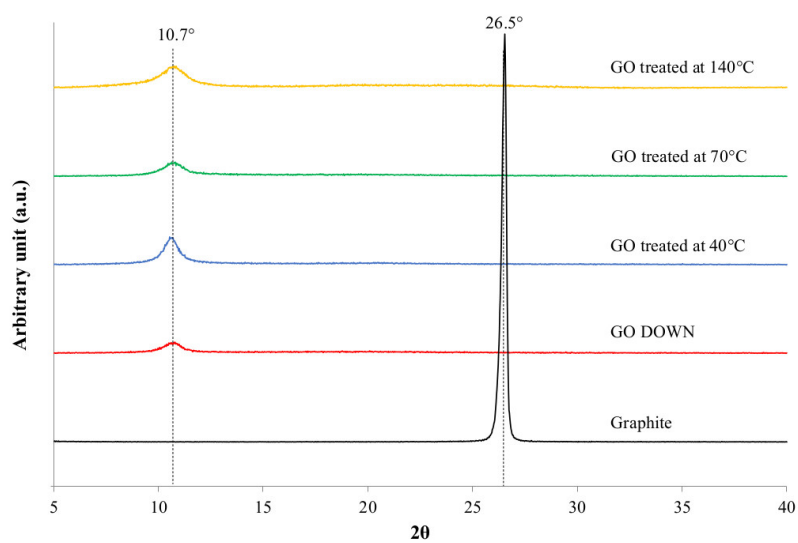
Figure 4.20. *XRD* patterns of the raw graphite, the *GO DOWN* and the *GO* thermally treated.

In Table 4.3 are reported all the diffraction angles and the entire relative spacing between the graphene planes for each sample analyzed with this technique.

Table 4.3. Interlayer distances obtained with *XRD* analyses.

Samples	2θ	Spacing ($\mathring{A}$)
Graphite	26.5	3.4
GO DOWN	10.7	8.2
GO UP	10.7	8.2
GO treated at $40°C$	10.6	8.2
GO treated at $70°C$	10.9	8.1
GO treated at $140°C$	10.8	8.1

4.1.7 *TG* Analyses

Thermogravimetric analyses was conducted to test and evaluate the thermal stability of *GO* sheets. In Figure 4.21 is reported the *TGA* diagram obtained, both in air and in nitrogen atmosphere, for the raw graphite. The material is stable until nearly $700°C$ after which, starts the combustion only for the sample tested in air obviously. In Figure 4.22 are reported the *TGA* diagram obtain for the *GO UP*, *GO DOWN* and of the raw graphite.
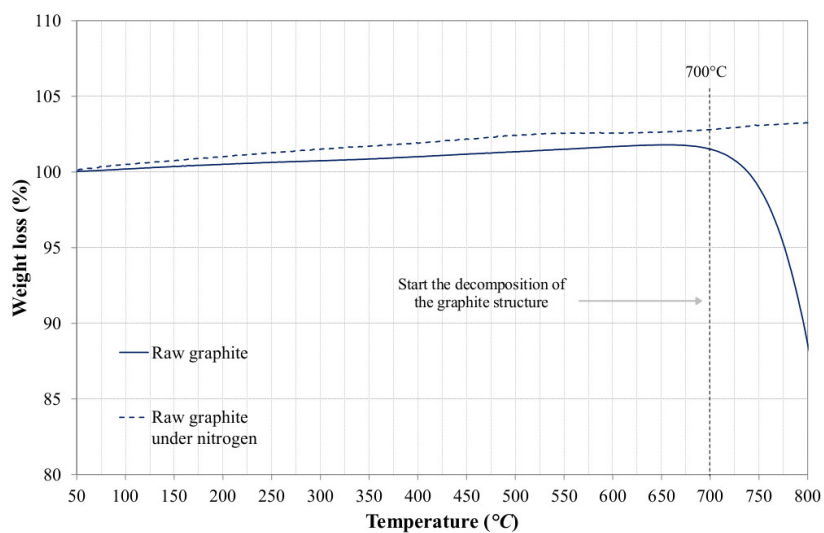
Figure 4.21. *TGA* diagram of raw graphite obtained in air and under nitrogen.

Four stages were observed for both the oxidized samples:

- a little loss (10%) occurred till 100°C, primarily due to the loss of H_2O molecules adsorbed between the *GO* layer with steam released;

- thermal decomposition of the most labile oxygen functional groups showed a roughly 30% quality loss, occurring at a temperature between 100 and 200°C;

- between 200 and 375°C a slower mass loss (15%) that can be attributes by the removal of more stable functionalities;

- from 450°C start the decomposition of the graphitic backbone of the samples (combustion of the carbon skeleton).
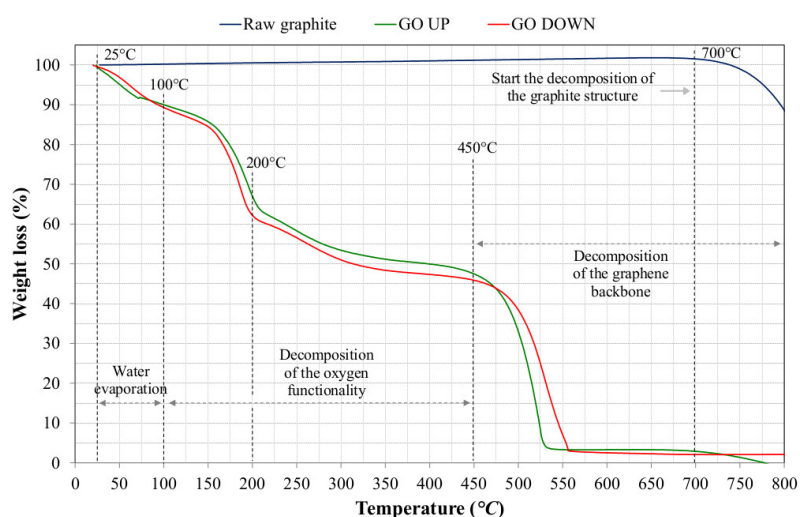
Figure 4.22. *TGA diagram obtained for the GO DOWN, GO UP and raw graphite in air.*

The analyses results, indicate the good thermal stability of the *GO* sheets. The *TGA* diagram of the raw graphite is reported in this Figure to observe how the oxidation process act on the carbon skeleton: for the raw graphite the combustion starts at 700°C instead for the *GO* sample starts before (450°C) as a signal of the formation of defects in the structure as observed with *FT-IR* and Raman spectra.

In Figure 4.23 are reported the *TGA* diagrams of the *GO UP* and *GO DOWN*, obtained also under nitrogen. The only difference between the

diagram obtained under air and under nitrogen is, obviously, the absence in the second case of the combustion of the carbon skeleton. In Figure 4.24 is reported the *TGA* diagram of *GO DOWN, GO UP* and *GO OLD*: the amount of water adsorbed by the sample of the *GO OLD* cause a higher weight loss in the first area which is a confirm of what assessed until now.
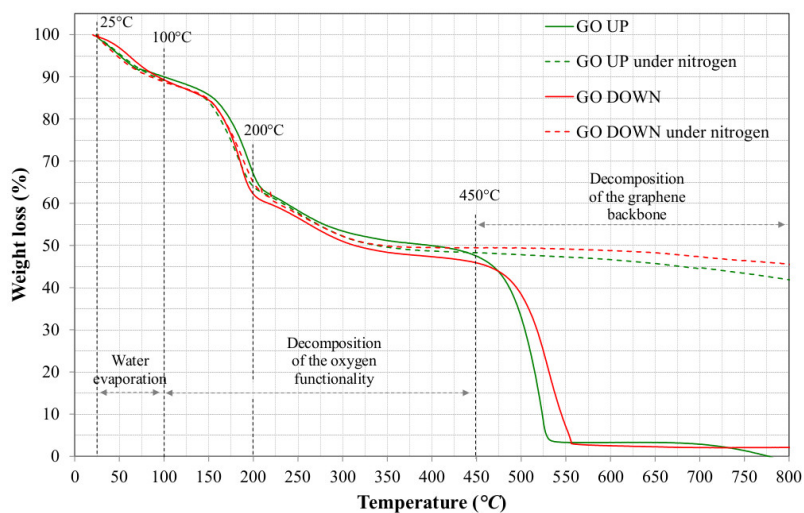
Figure 4.23. *TGA* diagram obtained for the *GO DOWN* and *GO UP* in air and under nitrogen.
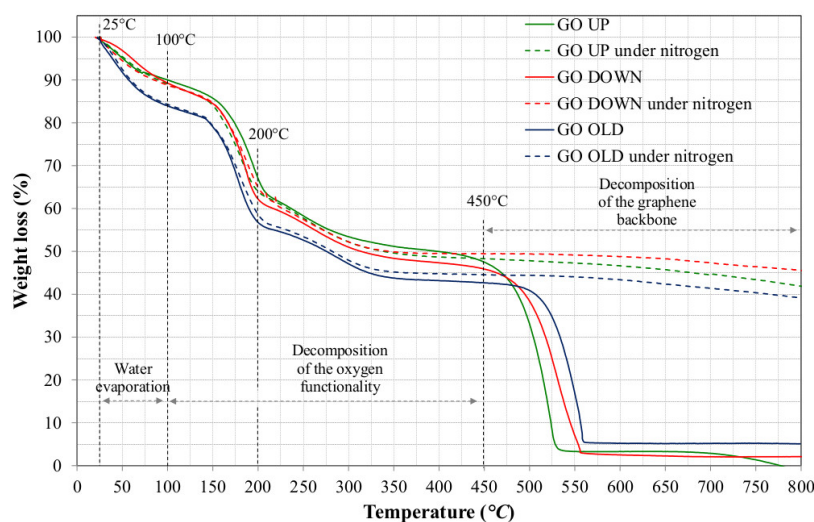
Figure 4.24. *TGA* diagram obtained for the *GO DOWN, GO UP* and *GO OLD* in air and under nitrogen.

We also performed the *TGA* on the samples thermally treated: *GO 40*, *GO 70* and *GO 140* (Figure 4.25). As the applied temperature was increased, the amount of weight loss associated to the water evaporation decreases, in particular for the *GO 140* which is characterized by a loss ≤5% respect 15% of loss in the *GO OLD* diagram. In the Figure 4.26 the same *TGA* diagram of the Figure 4.25 were reported with the ones obtained under nitrogen: the differences are exactly as the other, there is not the combustion of the carbon skeleton.
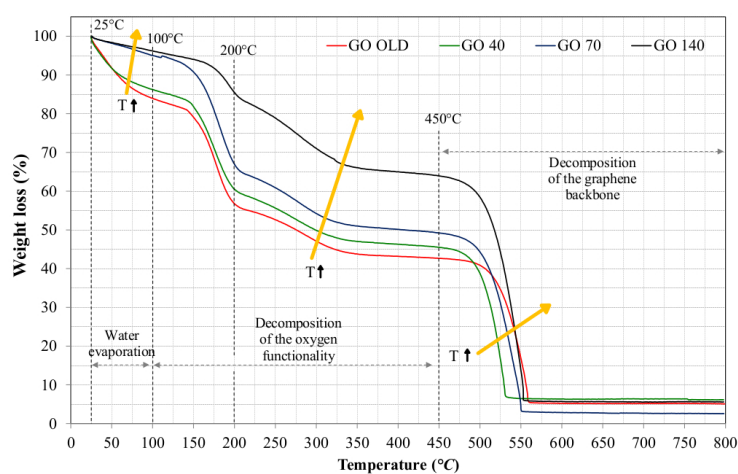
Figure 4.25. *TGA* diagram obtained for the *GO 40*, *GO 70*, *GO 140* and *GO OLD* in air.
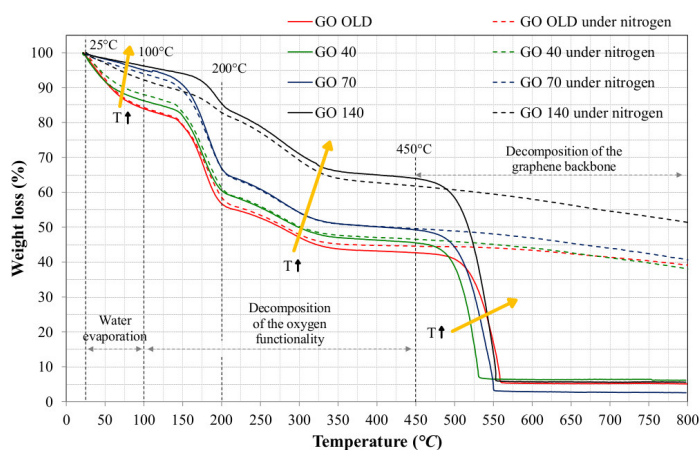
Figure 4.26. *TGA* diagram obtained for the *GO 40*, *GO 70*, *GO 140* and *GO OLD* in air and under nitrogen.

4.1.8 *TEM* and *SAED*

With the Transmission Electron Microscopy, we are able to observe the effect of sonication stage and control the exfoliation the material. We used two sample of *GO* for this analysis, both prepared following the process described in the Paragraph 3.2, but only the first one undergoes the sonication stages. In Figure 4.27 we reported the *TEM* images obtain for the first sample of *GO*: it appears to be well exfoliated but not reaching the condition of single sheet of graphene, which was not our objective.
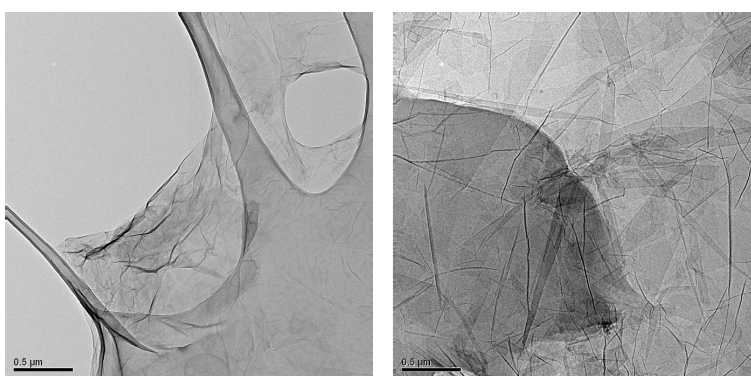
Figure 4.27. *TEM* images of the same sample of *GO* that has been sonicated after the purification stage.

instead observing the Figure 4.28 it is easy to see the difference respect the first sample: the *GO* sheets appears more packed, meaning that the sonication stage is fundamental to allow a good exfoliation of the system.
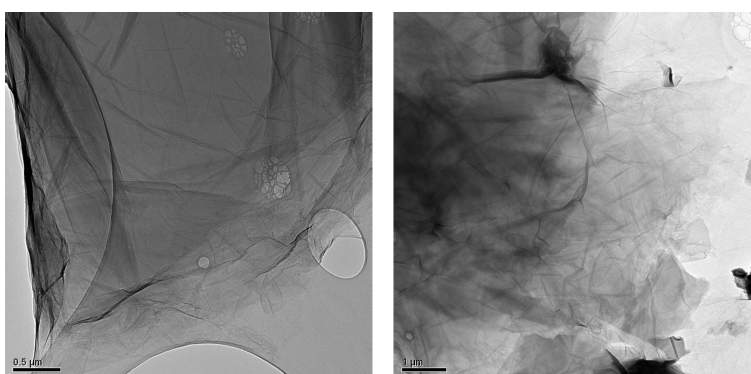
Figure 4.28. *TEM* images of the same sample of *GO* that has not been sonicated after the purification stage.

In the Figure 4.29 are reported the *SAED* pattern with the Miller index, obtained for the two samples used for the *TEM* images. The first one on the left (Figure 4.29 a) is the *SAED* pattern of the sonicated sample instead the second one on the right (Figure 4.29 b) is the pattern of the non-sonicated specimen. In the first case we able to identify some bright spots meaning that the *GO* sheets are not completely amorphous. Individual spots are barely visible suggesting that there are no preferential stacking orientations between the *GO* sheets. Instead in the second case we can observed a ring pattern characteristic of a polycrystalline sample which confirm the necessary role of the sonication stage for the exfoliation.

a)   b)
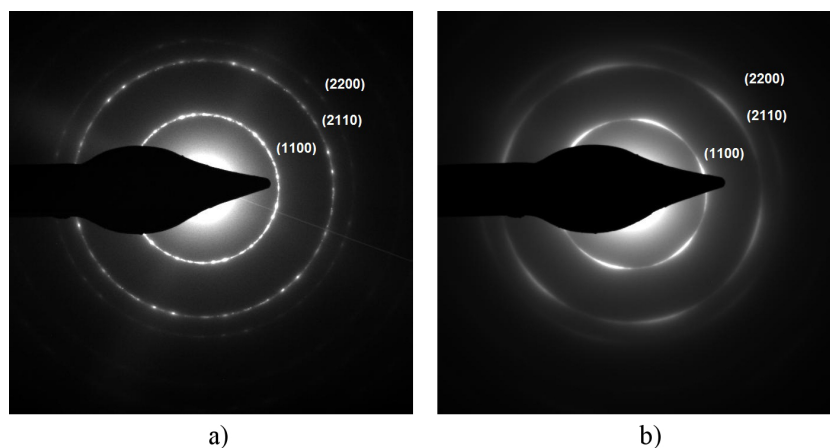
Figure 4.29. *SAED* pattern of two different sample: a) sonicated *GO*; b) not sonicated *GO*.

4.2 *GO-Jeffamine M600* characterization

The characterization of the chemically modified graphene oxide (*GO-Jeffamine M600*) will be discussed considering Thermogravimetric analyses and Infrared spectroscopy. Firstly, we performed the *TGA* analyses of the *Jeffamine M600* in air and under nitrogen, obtaining the diagram reported in Figure 4.30. The *Jeffamine M600* is thermally stable until 200 °C, after which start to decompose.
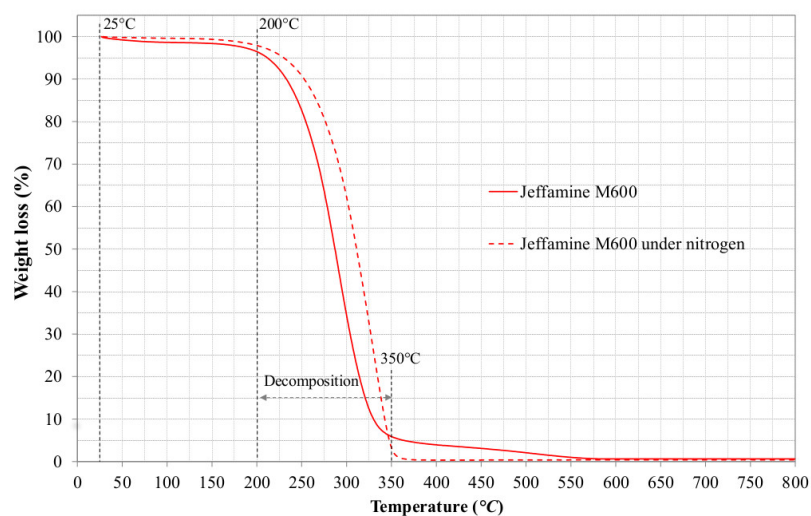
Figure 4.30. *TGA* diagram of the *Jeffamine M600* obtained in air and under nitrogen.

In Figure 4.31 are reported the *TGA* diagram of the *GO-Jeffamine M600* together with the one of *Jeffamine M600* and of *GO OLD*, as references. We can identify three regions:

- until 225°*C* we observed a loss due to the evaporation of the water and to the decomposition of the most labile oxygen functionalities that remains on the *GO* after the functionalization;

- between 225°*C* and 425°*C* a bigger loss mainly attributed to the decomposition of the *Jeffamine M600*;

- after 425°*C* the decomposition of the graphitic backbone is achieved.

In Figure 4.32 are reported the *TGA* diagram of the *GO-Jeffamine M600* obtained in air and under nitrogen: obviously the combustion of the graphitic backbone of the *GO* does not take place under nitrogen. We can affirm that the *Jeffamine M600* is present in the sample but we are not able to specify if it is chemically bonded on the *GO* surface or, if a physical mixture with the *GO* is formed. To understand if the amidic bond between the *Jeffamine M600* and the *GO* is formed, we performed *FT-IR* analyses. In Figure 4.33 we reported the *FT-IR* spectra of *GO-Jeffamine M600* together with the spectra of the *GO OLD* (already discussed in the Paragraph 4.1.2) and the *Jeffamine M600*.
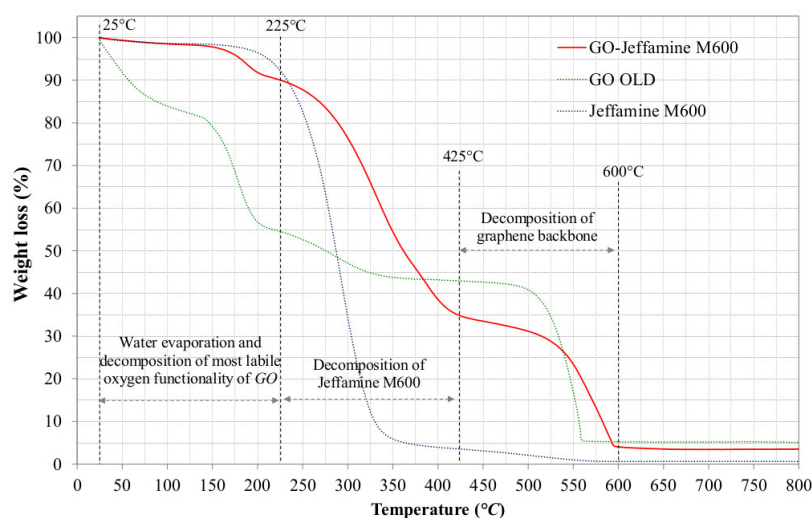
Figure 4.31. *TGA* diagram of the *GO-Jeffamine M600*, *GO OLD* and *Jeffamine M600* obtained in air.
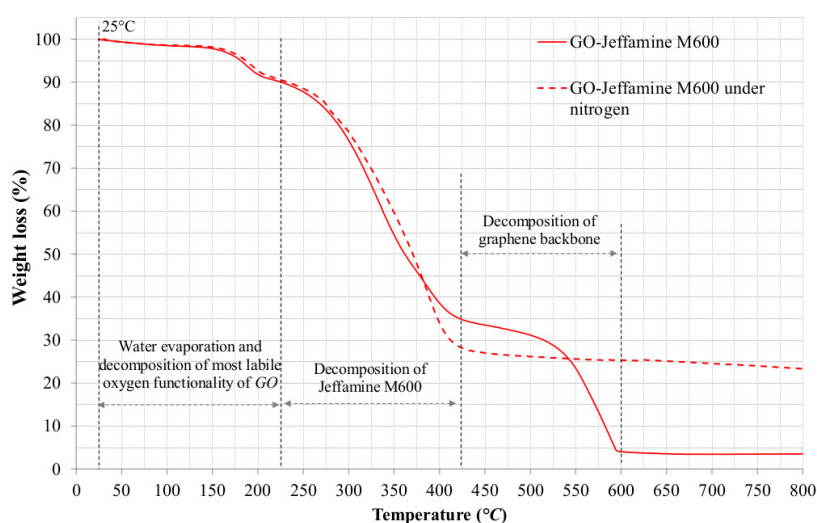
Figure 4.32. *TGA* diagram of the *GO-Jeffamine M600* and *GO-Jeffamine M600* obtained in air and under nitrogen.

Considering the spectrum of the *Jeffamine M600*, we can identify:

- *N-H* stretching at 3369 cm^{-1} and 3297 cm^{-1};

- *C-H* stretching in the region 3000 cm^{-1} and 2800 cm^{-1}

- peaks assigned to vibration of the *Jeffamine* chain in the region 1500 cm^{-1} and 800 cm^{-1} and strong *C-O-C* stretching at 1110 cm^{-1}.
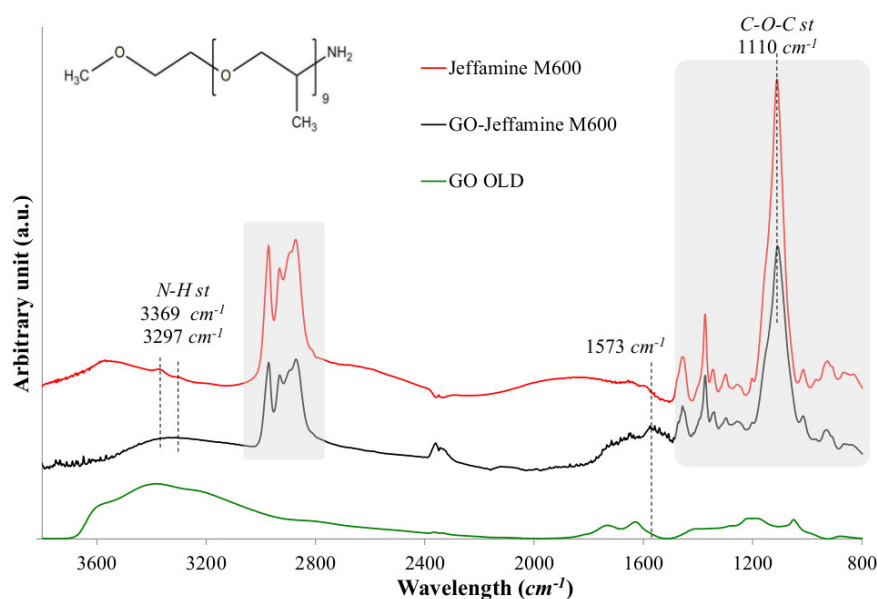
Figure 4.33. *FT-IR* spectra of *Jeffamine M600*, *GO-Jeffamine M600* and *GO OLD*.

Considering the spectrum of the *GO-Jeffamine M600* (Figure 4.33), no evidence of the formation of the amidic bond (strong band between 1695-1630 cm^{-1} [96]) can be found. Comparing the spectra of Figure 4.33 we can make some consideration:

- the peaks in the region 1500 cm^{-1} and 800 cm^{-1}, associated to the vibration of *Jeffamine M600* chain, are not affected by the reaction;

- the peaks of *N-H* stretching of *Jeffamine M600* at 3369 cm^{-1} and 3297 cm^{-1} disappear;

- the *-OH* stretching region at 3400 cm^{-1} slightly changes with respect to the *GO* case;

- all the bands in the region previously associated to the oxygen functionalities in the region 1500 cm^{-1} and 800 cm^{-1} are shadowed by the strong absorption of *Jeffamine*;

- new peak at 1573 cm^{-1} cannot be associated neither to the *GO* and nor to the *Jeffamine M600*.

The reaction of functionalization with *Jeffamine M600* does not produced the expected chemically modified graphene oxide with amidic bonds, but

we can affirm that the product obtained is not a physical mixture of *GO* and *Jeffamine M600*. Further studies should be performed to characterize the products of this reaction.

4.3 Cement base composites characterization

In this section the characterization of the mortar samples containing the *GO*, is reported. Firstly, we performed the mechanical analyses to obtain the compressive and flexural resistance, than the specimens has been observed with the Scanning Electron Microscopy and analyzed with the Energy Dispersive Spectroscopy.

4.3.1 Mechanical characterization

The mechanical characterization of the cement base composites has been performed following the procedure described in the Paragraph 3.5.1. The mean compressive resistance obtained for the mortar samples containing the solution 1 and solution 2 are reported respectively in Table 4.4 and 4.5, instead the mean flexural resistance is reported in Table 4.6 for the specimens containing the solution 1 and in Table 4.7 for the samples containing the solution 2.

Table 4.4. Mean compression resistance of the mortar samples containing the solution 1.

	3 days		7 days		28 days	
GO (%)	*MPa*	*dev%*	*MPa*	*dev%*	*MPa*	*dev%*
0	54.1	± 1.2	61.8	± 2.2	72.6	± 2.2
0.02	52.2	± 2.0	59.2	± 2.0	71.0	± 3.1
0.04	51.5	± 1.8	61.1	± 1.8	68.9	± 2.7
0.06	51.0	± 1.7	59.9	± 1.6	69.9	± 2.2

Table 4.5. Mean compression resistance of the mortar samples containing the solution 2.

GO (%)	3 days		7 days		28 days	
	MPa	*dev%*	*MPa*	*dev%*	*MPa*	*dev%*
0	54.1	± 1.2	61.8	± 2.2	72.6	± 2.2
0.02	51.8	± 1.4	58.8	± 1.1	67.9	± 3.0
0.04	49.7	± 2.2	58.5	± 1.0	68.9	± 2.2
0.06	50.8	± 1.7	58.3	± 1.9	67.0	± 2.4

Table 4.6. Mean flexural resistance of the mortar samples containing the solution 1.

GO (%)	3 days		7 days		28 days	
	MPa	*dev%*	*MPa*	*dev%*	*MPa*	*dev%*
0	8.2	± 0.1	9.0	± 0.2	9.6	± 0.5
0.02	8.6	± 0.1	8.8	± 0.2	9.5	± 0.5
0.04	8.6	± 0.5	9.1	± 0.3	9.1	± 0.2
0.06	8.3	± 0.1	8.9	± 0.1	9.2	± 0.2

Table 4.7. Mean flexural resistance of the mortar samples containing the solution 2.

GO (%)	3 days		7 days		28 days	
	MPa	*dev%*	*MPa*	*dev%*	*MPa*	*dev%*
0	8.2	± 0.1	9.0	± 0.2	9.6	± 0.5
0.02	8.9	± 0.1	8.8	± 0.2	9.2	± 0.4
0.04	8.4	± 0.3	8.3	± 0.5	8.4	± 0.2
0.06	7.7	± 0.5	8.4	± 0.4	8.6	± 0.2

In the Paragraph 2.5 we reported the mechanical improvement observed by several authors [1], [29], [91], [92] and obtained by the adding of little amount of *GO* in cement. Considering the previous Table, no improvement neither in compression and nor in flexural resistance have been observed in

our study. Although, no net differences has been observed in mechanical resistance between the samples containing the two different solutions (1 and 2) with *GO* characterized by different content of oxygen. Trying to understand why the addition of *GO* never influenced the mechanical properties of the mortar sample as expected, we observed the microstructure of the hydration products with Scanning Electron Microscopy.

4.3.2 *SEM* analyses

Because the mechanical resistance measured for the composites sample with solution 1 and solution 2 are nearly the same we decide to analyzed only one series of mortars samples, the ones containing the solution 1. Our hypotheses is that the *GO* sheets are not well dispersed in the cement mortar, forming aggregate particles, which do not contribute to the reinforcing of the paste. First we analyzed the control sample, mortar without the addition of *GO*, after 3, 7 and 28 days of curing: the Figure 4.34, report the *SEM* micrograph obtained. In the following Figure are reported all the *SEM* micrographs obtained for the specimens with different content of *GO*: 0.02% *wt.* (Figure 4.35), 0.04% *wt.* (Figure 4.36) and 0.06% *wt.* (Figure 4.37), considering three different time of curing (3, 7 and 28 days).

We can affirm that the flower and polyhedron-like crystals that determine a more compact and less porous structure in the cement paste, observed by Shenghua et al. [91], [1], [92], are not present in our samples. This means that the *GO* does not influenced the cement hydration and so the formation of the crystals. Shenghua et al. [91] used *GO* sheets of some hundreds of nanometer (from 430 to 72 *nm*), ours were in the range of 100 *μm*: we supposed that in their case the *GO* sheets remain planar in the cement paste, instead our sheets tend to deformed and lose planarity.

a)

b)

c)
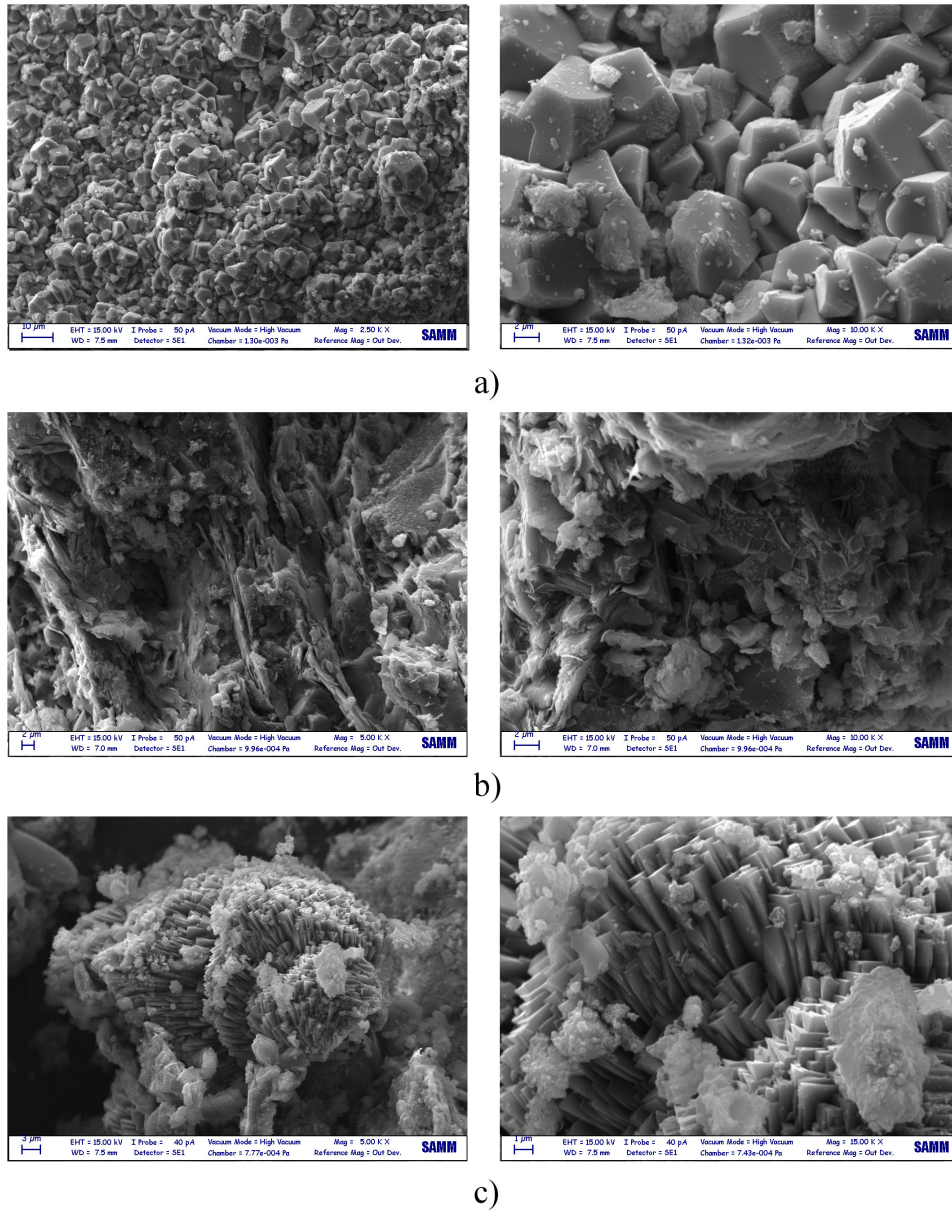
Figure 4.34. *SEM* micrographs of the control mortar samples at: a) 3 days; b) 7 days; c) 28 days.
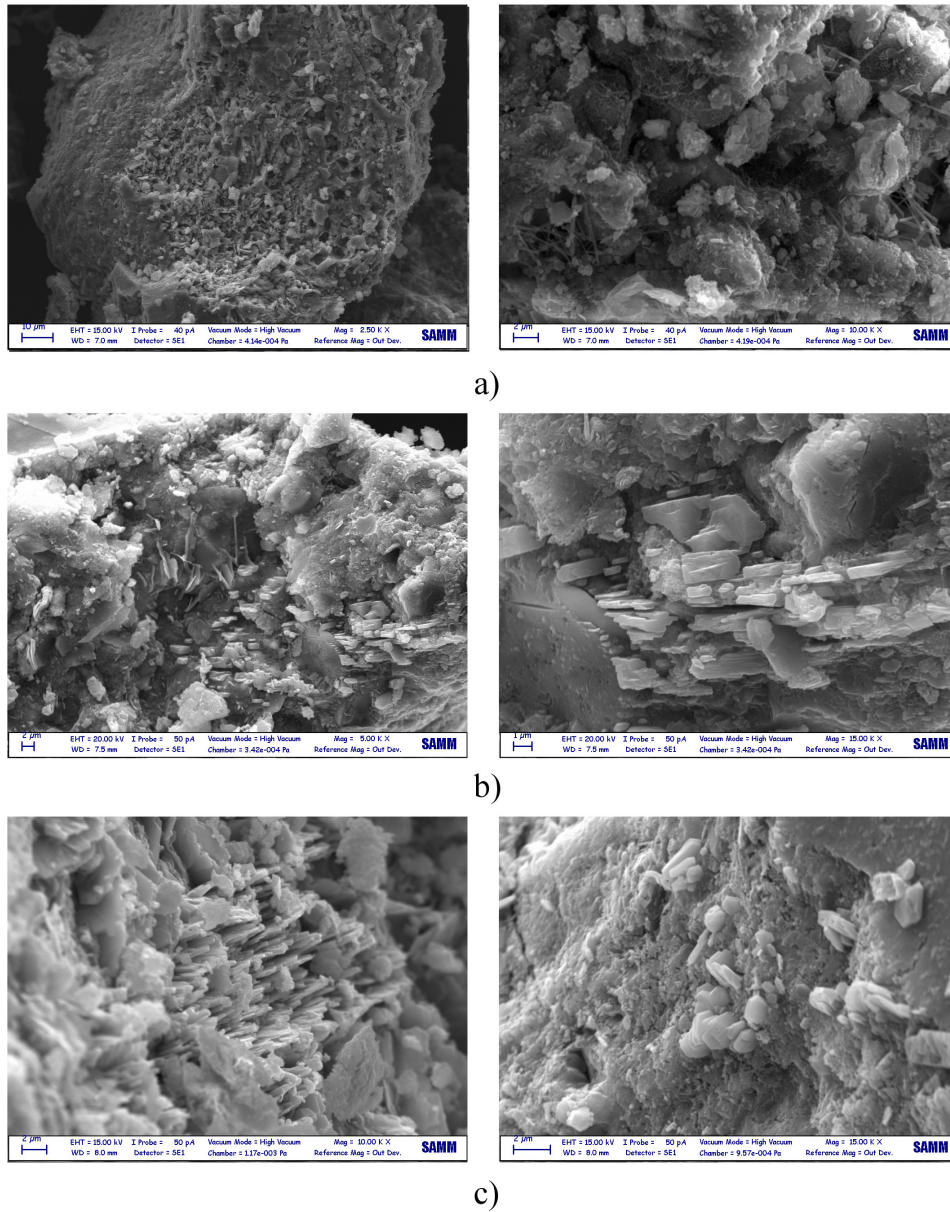
Figure 4.35. *SEM* micrographs of the mortar samples containing 0.02% of *GO* at:
a) 3 days; b) 7 days; c) 28 days.

a)

b)

c)
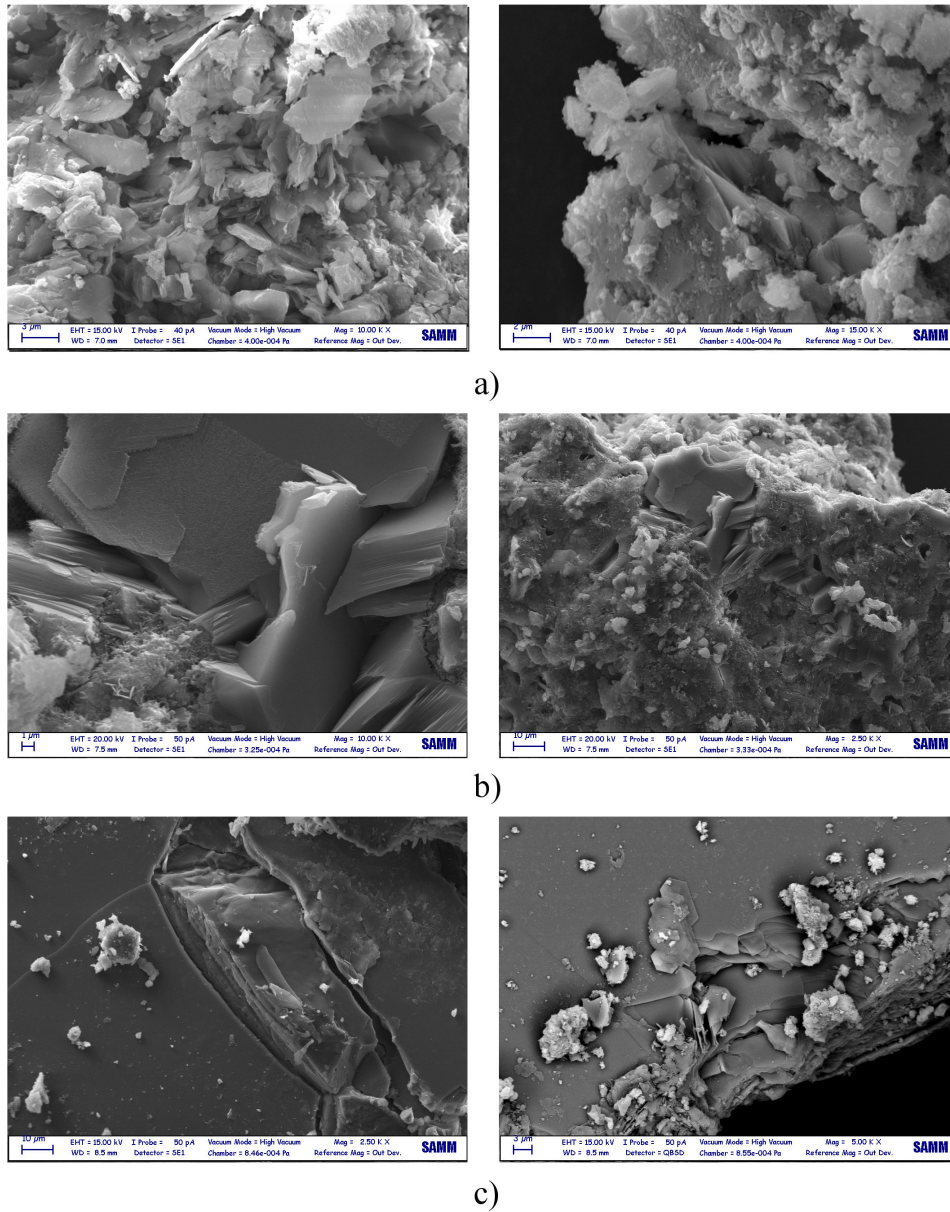
Figure 4.36. *SEM* micrographs of the mortar samples containing 0.04% of *GO* at:
a) 3 days; b) 7 days; c) 28 days.
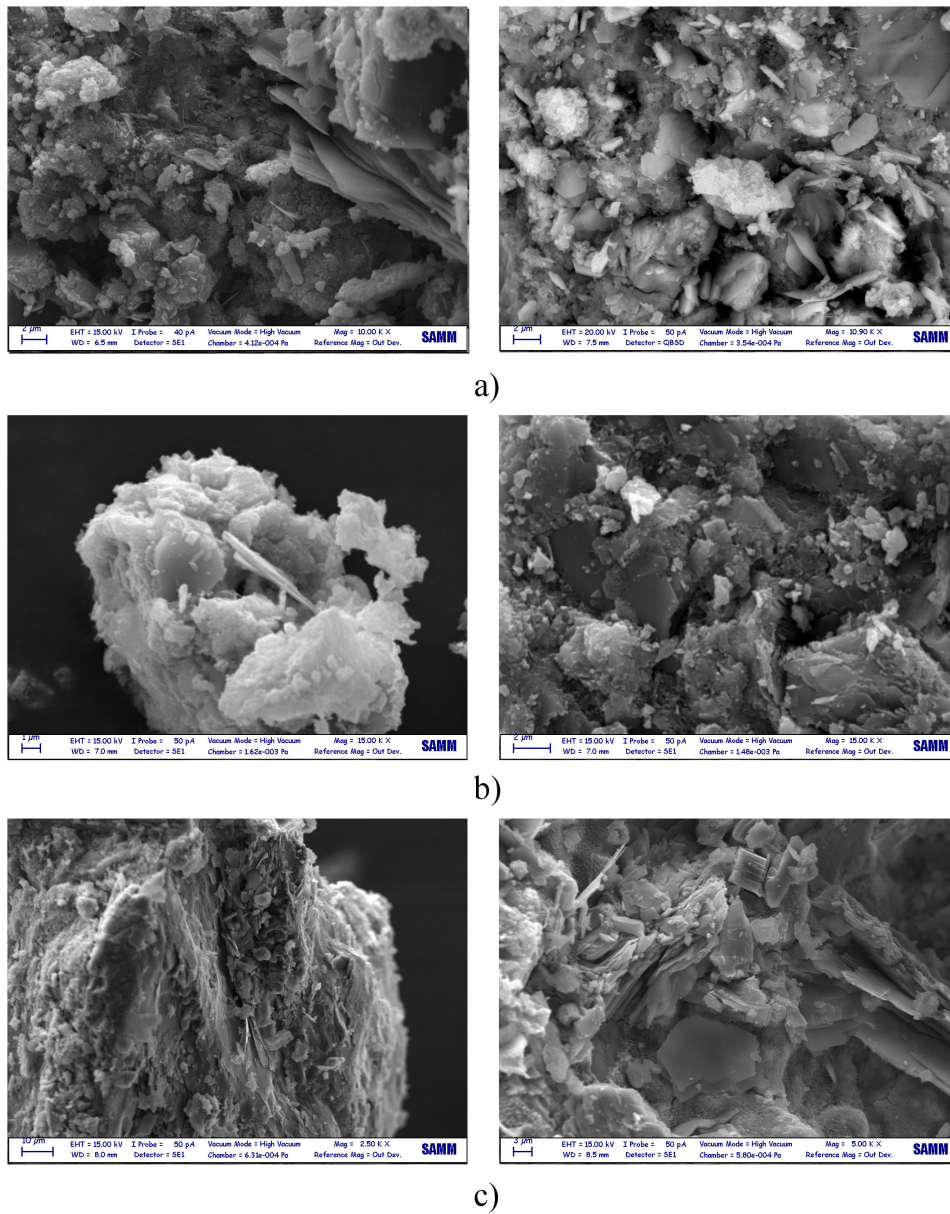
Figure 4.37. *SEM* micrographs of the mortar samples containing 0.06% of *GO* at:
a) 3 days; b) 7 days; c) 28 days.

Although, in all the *SEM* micrograph reported no aggregation of graphene oxide has been observed. In particular, only in one sample the *GO* sheets were exposed to the fracture surface (Figure 4.38): void between the *GO* and the cement paste is present (not compact structure) and no interaction between the hydration product and the *GO* is present.
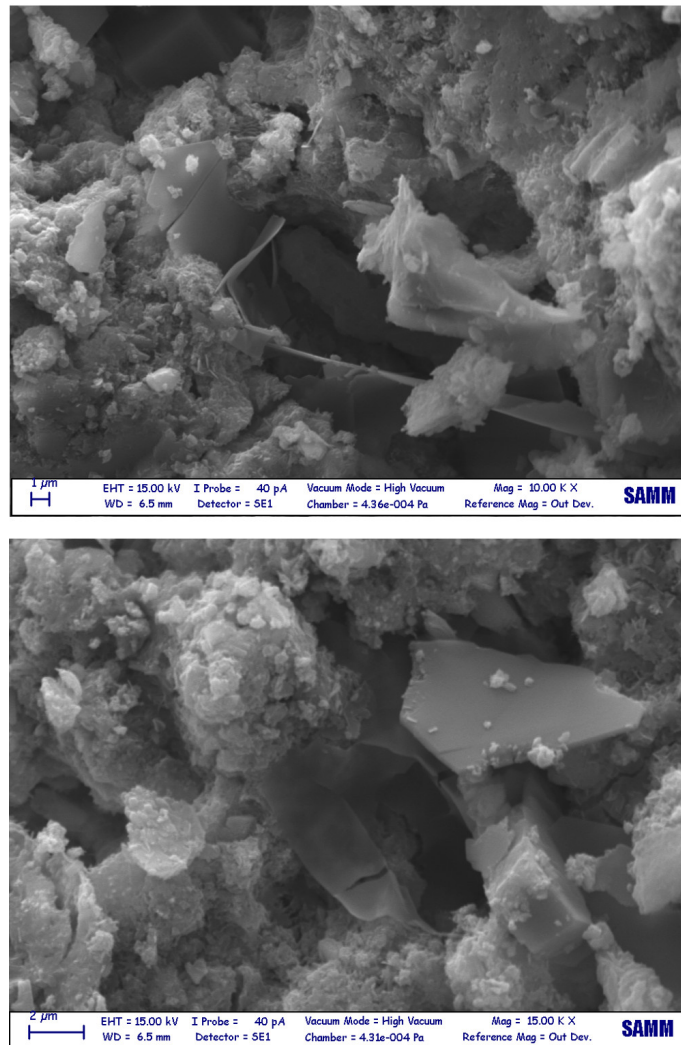
Figure 4.38. *SEM* micrographs of the mortar samples containing 0.02% of *GO* at 3 days of curing.

4.3.3 *EDS* analyses

We performed *EDS* analyses in order to ascertain the *GO* distribution in the samples: the mean value of the obtained result for the specimens of mortar containing 0.02% *wt.*, 0.04% *wt.* and 0.06 % *wt.* are reported respectively in Table 4.8, 4.9 and 4.10. In Figure 4.39 are reported the *EDS* maps observed for the mortar sample containing 0.06% of *GO*.

We not succeed to discerner the contribution of graphene oxide from the carbon content of the carbonate. Further studies are necessary.

Table 4.8. Elemental analyses performed on mortar sample containing 0.02% *wt* of *GO*.

C		O		Na		Mg		Al	
%wt.	dev%	%wt.	dev%	%wt.	dev%	%wt.	dev%	%wt.	dev%
6.78	±1.91	40.46	±2.13	0.31	±0.17	0.64	±0.18	1.18	±0.05

Si		S		K		Ca		Fe	
%wt.	dev%	%wt.	dev%	%wt.	dev%	%wt.	dev%	%wt.	dev%
5.90	±0.36	0.37	±0.16	1.55	±0.37	41.15	±2.36	1.67	±0.81

Table 4.9. Elemental analyses performed on mortar sample containing 0.04% *wt* of *GO*.

C		O		Na		Mg		Al	
%wt.	dev%	%wt.	dev%	%wt.	dev%	%wt.	dev%	%wt.	dev%
5.47	±2.1	49.33	±2.54	0.37	±0.1	1.12	±0.61	1.29	±0.77

Si		S		K		Ca		Fe	
%wt.	dev%	%wt.	dev%	%wt.	dev%	%wt.	dev%	%wt.	dev%
6.13	±0.35	0.47	±0.06	0.86	±0.21	33.87	±1.99	1.10	±0.09

Table 4.10. Elemental analyses performed on mortar sample containing 0.06% *wt* of *GO*.

C		*O*		*Na*		*Mg*		*Al*	
%*wt.*	dev%	%*wt.*	dev%	%*wt.*	dev%	%*wt.*	dev%	%*wt.*	dev%
6.90	±1.09	35.93	±2.44	0.30	±0.06	0.36	±0.16	3.48	±2.21

Si		*S*		*K*		*Ca*		*Fe*	
%*wt.*	dev%	%*wt.*	dev%	%*wt.*	dev%	%*wt.*	dev%	%*wt.*	dev%
6.96	±1.69	1.28	±0.89	1.11	±0.49	41.40	±5.73	2.27	±0.84
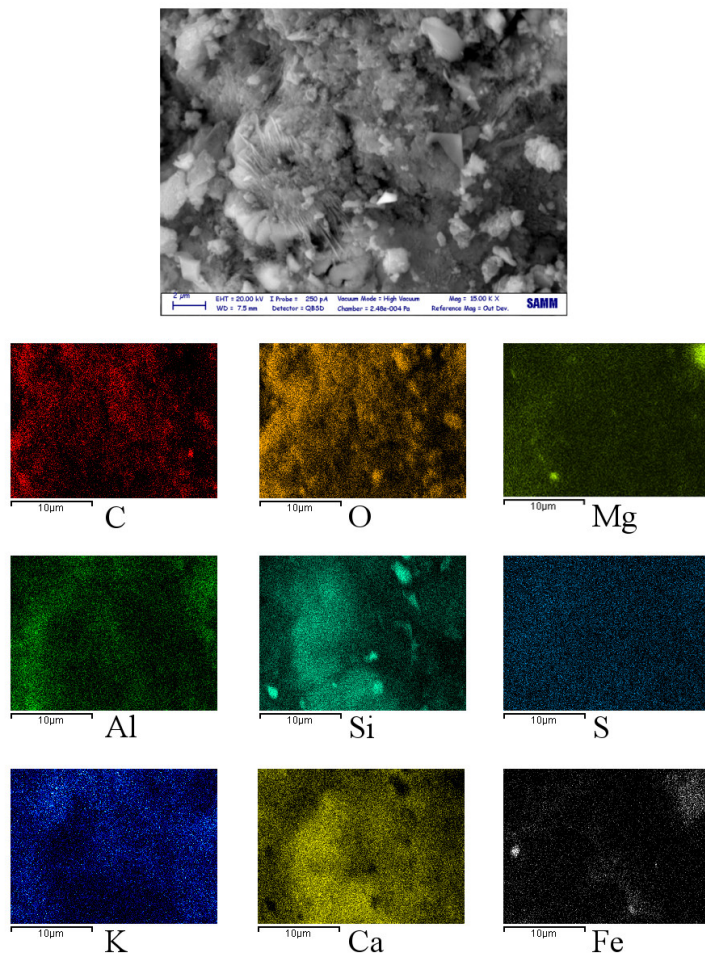
Figure 4.39. *EDS* maps of mortar sample containing 0.06% of *GO* at 7 days of curing.

Chapter 5

Conclusion

In this work graphene oxide has been prepared starting from graphite powder via the Hummer's method and fully characterized with several techniques (Infrared and Raman spectroscopy, *TGA*, *XRD*, *ICP*, *EA*, *TEM* and *SAED*). Water solutions containing different *GO* samples were prepared and used for the packing of the mortar samples with 0.02% *wt.*, 0.04% *wt.* and 0.06% *wt.* *GO* content. Compression and flexural test has been performed on the specimens to determine the mechanical resistance of the samples and *SEM* and *EDS* analyses were carried out to observe the effect of *GO* on the morphology of the hydration crystals. The reaction of the *GO* with the *Jeffamine M600* has been performed, and the product (*GO-Jeffamine M600*) has been characterized using Infrared spectroscopy and Thermogravimetric analyses.

Overall, the results can be summarized as following:

- The Hummer's method is an efficient approach to produce graphene oxide with a high content of oxygen as demonstrated with Infrared spectroscopy and with Elemental analyses.

- Raman spectroscopy is a powerful tool to study the graphene related material. With this technique, we confirm that oxidation introduces disorder in the carbon backbone: defects and edges on the sp^2 carbon structure as evidenced by the higher I_D/I_G ratio in the graphene oxide sample respect to one observed in the raw graphite.

- The sonication stage after the purification of the product is fundamental to achieve the exfoliation of the systems, as demonstrate with *TEM* image and the *SAED* pattern.

- The storage of the *GO* in water determines the adsorption of water molecules which show strong *-OH* stretching and *H-O-H* bending peaks in the infrared spectrum.

- Thermal treatment of graphene oxide reduce the amount of water adsorbed on the platelets, but until $70°C$ does not induce significant reduction of the oxygen functionalities.

- Thermal treatment at $140°C$ determines the reduction of the oxygen functionality and a partial reconstruction of the sp^2 carbon backbone, as demonstrated by the presence of the two strong bands at 1590 cm^{-1} and 1240 cm^{-1} of the *GO 140* assigned respectively to the *G* and *D* peaks *IR* activated by the presence of the *C=O* group that polarized the partially reconstructed sp^2 carbon backbone.

- The effect of thermal treatment has been also studied with the Raman spectroscopy: we observed a progressively reduction of the base line profile and a decreases of the Raman signal placed between the *D* and the *G* peaks, which is associated to amorphous sp^3 carbon structures. This observation suggests that reduction processes preferentially starts on the sp^3 carbon fraction of the *GO* promoting a partial reconstruction of the sp^2 carbon system, as demonstrated by the I_D/I_G ratio measured for this two samples.

- Different oxidation times determine a changing in the proportion of the oxygen functionalities on the *GO* allowing the possibility to control the properties of the graphene oxide itself. Some small variation in in the sp^2 carbon backbone have been observed with Raman spectroscopy.

- The effect of different oxidation time has been observed also with Elemental analyses demonstrating that the kinetic of the oxidation reaction is very fast.

- No improvement in mechanical properties, compression and flexural resistance, has been observed in the mortar sample containing *GO* in the range of 0.02% and 0.06% *wt.*: this failure is attributed to the big dimension of the *GO* platelets that, in the cement paste, tend to lose planarity and does not have any influences on the formation of the hydration product.

As general conclusion we have examined the most suitable materials and procedure for the syntheses and the characterization of the *GO* and of the cement base composite.

Future works:

- Further studies are recommended on cement base composites reinforced with *GO* characterized with very small lateral dimension (less than 500 *nm*).

- The production procedure of mortar specimens require adjustment, in particular in the dispersion stage of the *GO* in the cement composite.

- Further studies are needed for the comprehension of the reaction mechanism between the *Jeffamine M600* and the *GO*.

- The syntheses procedure of the *GO-Jeffamine M600* must be optimized in term of reaction time and yield.

Bibliography

[1] Shenghua Lv, Sun Ting, Jingjing Liu, and Qingfang Zhou. Use of graphene oxide nanosheets to regulate the microstructure of hardened cement paste to increase its strength and toughness. *CrystEngComm*, 16(36):8508–8516, 2014.

[2] Astm c219 14a: Standard terminology relating to hydraulic cement, 2012.

[3] Paulo J. M. Monteiro P. Kumar Mehta. *Concrete: Microstructure, Properties, and Materials*. McGraw Hill, 2013, 4th edition.

[4] Pietro Pedeferri Luca Bertolini. *Tecnologia dei materiali: Leganti e calcestruzzo*. 2000.

[5] Luigi Coppola. *Concretum*. McGraw Hill, 2007.

[6] Henry le Chatelier. Crystalloids against colloids in the theory of cements. *Trans. Faraday Soc.*, 14(0):8–11, 1919.

[7] Treval Clifford Powers and Theodore Lucius Brownyard. Studies of the physical properties of hardened portland cement paste. 43(9), 1946.

[8] JD Bernal, JW Jeffery, and HFW Taylor. Crystallographic research on the hydration of portland cement. a first report on investigations in progress. *Magazine of Concrete research*, 4(11):49–54, 1952.

[9] H. F. W. Taylor. 726. hydrated calcium silicates. part i. compound formation at ordinary temperatures. *J. Chem. Soc.*, (0):3682–3690, 1950.

[10] Helen D Megaw and CH Kelsey. Crystal structure of tobermorite. 1956.

[11] IG Richardson. Tobermorite/jennite-and tobermorite/calcium hydroxide-based models for the structure of csh: applicability to hardened pastes of tricalcium silicate, β-dicalcium silicate, portland cement, and blends of portland cement with blast-furnace slag, metakaolin, or silica fume. *Cement and Concrete Research*, 34(9):1733–1777, 2004.

[12] R.F. Feldman and P.J. Sereda. A model for hydrated portland cement paste as deduced from sorption-length change and mechanical properties. *Matriaux et Construction*, 1(6):509–520, 1968. cited By 0.

[13] IG Richardson. The nature of csh in hardened cements. *cement and concrete research*, 29(8):1131–1147, 1999.

[14] E Bonaccorsi, S Merlino, and HFW Taylor. The crystal structure of jennite, ca 9 si 6 o 18 (oh) 6· 8h 2 o. *Cement and Concrete Research*, 34(9):1481–1488, 2004.

[15] Paul D Tennis and Hamlin M Jennings. A model for two types of calcium silicate hydrate in the microstructure of portland cement pastes. *Cement and Concrete Research*, 30(6):855–863, June 2000.

[16] Jeffrey J Chen, Jeffrey J Thomas, Hal FW Taylor, and Hamlin M Jennings. Solubility and structure of calcium silicate hydrate. *Cement and Concrete Research*, 34(9):1499–1519, 2004.

[17] Jeffrey J Thomas and Hamlin M Jennings. A colloidal interpretation of chemical aging of the csh gel and its effects on the properties of cement paste. *Cement and Concrete Research*, 36(1):30–38, 2006.

[18] Yun-Yong Kim, Kwang-Myung Lee, Jin-Wook Bang, and Seung-Jun Kwon. Effect of w/c ratio on durability and porosity in cement mortar with constant cement amount. *Advances in Materials Science and Engineering*, 2014, 2014.

[19] M. Hoshino. Difference of the w/c ratio, porosity and microscopical aspect between the upper boundary paste and the lower boundary paste of the aggregate in concrete. *Materials and Structures*, 21(5):336–340, 1988.

[20] Karen L Scrivener, Alison K Crumbie, and Peter Laugesen. The interfacial transition zone (itz) between cement paste and aggregate in concrete. *Interface Science*, 12(4):411–421, 2004.

[21] JP Ollivier, JC Maso, and B Bourdette. Interfacial transition zone in concrete. *Advanced Cement Based Materials*, 2(1):30–38, 1995.

[22] Kuo-Yu Liao, Ping-Kun Chang, Yaw-Nan Peng, and Chih-Chang Yang. A study on characteristics of interfacial transition zone in concrete. *Cement and Concrete Research*, 34(6):977–989, 2004.

[23] G Prokopski and J Halbiniak. Interfacial transition zone in cementitious materials. *Cement and Concrete Research*, 30(4):579–583, 2000.

[24] Wu Xueqan, Li Dongxu, Wu Xiun, and Tang Minshu. Modification of the interfacial zone between aggregate and cement paste. In *MRS Proceedings*, volume 114, page 35. Cambridge Univ Press, 1987.

[25] Ye Qing, Zhang Zenan, Kong Deyu, and Chen Rongshen. Influence of nano-sio 2 addition on properties of hardened cement paste as compared with silica fume. *Construction and Building Materials*, 21(3):539–545, 2007.

[26] Meral Oltulu and Remzi ahin. Effect of nano-sio2, nano-al2o3 and nano-fe2o3 powders on compressive strengths and capillary water absorption of cement mortar containing fly ash: A comparative study. *Energy and Buildings*, 58:292 – 301, 2013.

[27] Shiho Kawashima, Pengkun Hou, David J. Corr, and Surendra P. Shah. Modification of cement-based materials with nanoparticles. *Cement and Concrete Composites*, 36:8 – 15, 2013. Special issue: Nanotechnology in Construction.

[28] Rafat Siddique and Ankur Mehta. Effect of carbon nanotubes on properties of cement mortars. *Construction and Building Materials*, 50:116 – 129, 2014.

[29] Samuel Chuah, Zhu Pan, Jay G Sanjayan, Chien Ming Wang, and Wen Hui Duan. Nano reinforced cement and concrete composites and new perspective from graphene oxide. *Construction and Building Materials*, 73:113–124, 2014.

[30] Andrzej M. Brandt. Fibre reinforced cement-based (frc) composites after over 40 years of development in building and civil engineering. *Composite Structures*, 86(13):3 – 9, 2008. Fourteenth International Conference on Composite StructuresICCS/14.

[31] Andrzej M Brandt. *Cement-based composites: materials, mechanical properties and performance*. CRC Press, 2009.

[32] Byung-Wan Jo, Chang-Hyun Kim, Ghi-ho Tae, and Jong-Bin Park. Characteristics of cement mortar with nano-sio 2 particles. *Construction and building materials*, 21(6):1351–1355, 2007.

[33] KL Lin, WC Chang, DF Lin, HL Luo, and MC Tsai. Effects of nano-sio 2 and different ash particle sizes on sludge ash–cement mortar. *Journal of Environmental Management*, 88(4):708–714, 2008.

[34] Hui Li, Hui-gang Xiao, Jie Yuan, and Jinping Ou. Microstructure of cement mortar with nano-particles. *Composites Part B: Engineering*, 35(2):185–189, 2004.

[35] Thanongsak Nochaiya and Arnon Chaipanich. Behavior of multi-walled carbon nanotubes on the porosity and microstructure of cement-based materials. *Applied Surface Science*, 257(6):1941 – 1945, 2011.

[36] Baomin Wang, Yu Han, and Shuai Liu. Effect of highly dispersed carbon nanotubes on the flexural toughness of cement-based composites. *Construction and Building Materials*, 46:8 – 12, 2013.

[37] Maria S. Konsta-Gdoutos, Zoi S. Metaxa, and Surendra P. Shah. Highly dispersed carbon nanotube reinforced cement based materials. *Cement and Concrete Research*, 40(7):1052 – 1059, 2010.

[38] Kostya S Novoselov, Andre K Geim, SV Morozov, D Jiang, Y Zhang, SV Dubonos, , IV Grigorieva, and AA Firsov. Electric field effect in atomically thin carbon films. *science*, 306(5696):666–669, 2004.

[39] Antonio Castro Neto, Francisco Guinea, and Nuno Miguel Peres. Drawing conclusions from graphene. *Physics World*, 19(11):33, 2006.

[40] Annalisa Fasolino, JH Los, and Mikhail I Katsnelson. Intrinsic ripples in graphene. *Nature materials*, 6(11):858–861, 2007.

[41] Jannik C Meyer, Andre K Geim, MI Katsnelson, KS Novoselov, TJ Booth, and S Roth. The structure of suspended graphene sheets. *Nature*, 446(7131):60–63, 2007.

[42] Jayeeta Lahiri, Travis S Miller, Andrew J Ross, Lyudmyla Adamska, Ivan I Oleynik, and Matthias Batzill. Graphene growth and stability at nickel surfaces. *New Journal of Physics*, 13(2):025001, 2011.

[43] Francesco Bonaccorso, Antonio Lombardo, Tawfique Hasan, Zhipei Sun, Luigi Colombo, and Andrea C Ferrari. Production and processing of graphene and 2d crystals. *Materials Today*, 15(12):564–589, 2012.

[44] Sasha Stankovich, Dmitriy A Dikin, Richard D Piner, Kevin A Kohlhaas, Alfred Kleinhammes, Yuanyuan Jia, Yue Wu, SonBinh T Nguyen, and Rodney S Ruoff. Synthesis of graphene-based nanosheets via chemical reduction of exfoliated graphite oxide. *Carbon*, 45(7):1558–1565, 2007.

[45] Helen R Thomas, Stephen P Day, William E Woodruff, Cristina Valles, Robert J Young, Ian A Kinloch, Gavin W Morley, John V Hanna, Neil R Wilson, and Jonathan P Rourke. Deoxygenation of graphene oxide: reduction or cleaning? *Chemistry of Materials*, 25(18):3580–3588, 2013.

[46] Cristina Botas, Patricia Álvarez, Patricia Blanco, Marcos Granda, Clara Blanco, Ricardo Santamaría, Laura J Romasanta, Raquel Verdejo, Miguel A López-Manchado, and Rosa Menéndez. Graphene materials with different structures prepared from the same graphite by the hummers and brodie methods. *Carbon*, 65:156–164, 2013.

[47] O Akhavan. The effect of heat treatment on formation of graphene thin films from graphene oxide nanosheets. *Carbon*, 48(2):509–519, 2010.

[48] Tapas Kuilla, Sambhu Bhadra, Dahu Yao, Nam Hoon Kim, Saswata Bose, and Joong Hee Lee. Recent advances in graphene based polymer composites. *Progress in Polymer Science*, 35(11):1350 – 1375, 2010.

[49] U Hofmann and R Holst. The acid nature and methylation of graphitic oxide. *Ber. Dtsc. Chem. Ges*, 72:754–771, 1939.

[50] G Ruess. Zur wasserbindung im halloysit. *Monatshefte für Chemie/Chemical Monthly*, 76(2):168–173, 1946.

[51] Daniel R Dreyer, Sungjin Park, Christopher W Bielawski, and Rodney S Ruoff. The chemistry of graphene oxide. *Chemical Society Reviews*, 39(1):228–240, 2010.

[52] Alexander Clause, Reinhold Plass, H-P Boehm, and Ulrich Hofmann. Untersuchungen zur struktur des graphitoxyds. *Zeitschrift für anorganische und allgemeine Chemie*, 291(5-6):205–220, 1957.

[53] W Scholz and HP Boehm. Studies on graphite vi considerations on the structure of graphite. *Anorg. Allg. Chem*, 369:327–340, 1969.

[54] T Nakajima, A Mabuchi, and R Hagiwara. A new structure model of graphite oxide. *Carbon*, 26(3):357–361, 1988.

[55] Tsuyoshi Nakajima and Yoshiaki Matsuo. Formation process and structure of graphite oxide. *Carbon*, 32(3):469–475, 1994.

[56] Heyong He, Thomas Riedl, Anton Lerf, and Jacek Klinowski. Solid-state nmr studies of the structure of graphite oxide. *The Journal of physical chemistry*, 100(51):19954–19958, 1996.

[57] Anton Lerf, Heyong He, Michael Forster, and Jacek Klinowski. Structure of graphite oxide revisited——. *The Journal of Physical Chemistry B*, 102(23):4477–4482, 1998.

[58] Tamás Szabó, Ottó Berkesi, Péter Forgó, Katalin Josepovits, Yiannis Sanakis, Dimitris Petridis, and Imre Dékány. Evolution of surface functional groups in a series of progressively oxidized graphite oxides. *Chemistry of materials*, 18(11):2740–2749, 2006.

[59] Benjamin C Brodie. On the atomic weight of graphite. *Philosophical Transactions of the Royal Society of London*, pages 249–259, 1859.

[60] L Staudenmaier. Method for the preparation of graphitic acid. *Ber Dtsch Chem Ges*, 31:1481–1487, 1898.

[61] William S Hummers Jr and Richard E Offeman. Preparation of graphitic oxide. *Journal of the American Chemical Society*, 80(6):1339–1339, 1958.

[62] Hossein Roghani-Mamaqani, Vahid Haddadi-Asl, Khezrollah Khezri, and Mehdi Salami-Kalajahi. Polystyrene-grafted graphene nanoplatelets with various graft densities by atom transfer radical polymerization from the edge carboxyl groups. *RSC Advances*, 4(47):24439–24452, 2014.

[63] Ji Chen, Bowen Yao, Chun Li, and Gaoquan Shi. An improved hummers method for eco-friendly synthesis of graphene oxide. *Carbon*, 64:225–229, 2013.

[64] Malgorzata Wojtoniszak and Ewa Mijowska. Controlled oxidation of graphite to graphene oxide with novel oxidants in a bulk scale. *Journal of Nanoparticle Research*, 14(11):1–7, 2012.

[65] Daniela C Marcano, Dmitry V Kosynkin, Jacob M Berlin, Alexander Sinitskii, Zhengzong Sun, Alexander Slesarev, Lawrence B Alemany, Wei Lu, and James M Tour. Improved synthesis of graphene oxide. *ACS nano*, 4(8):4806–4814, 2010.

[66] Leila Shahriary and ANJALI A Athawale. Graphene oxide synthesized by using modified hummers approach. *IJREEE*, 2:58–63, 2014.

[67] Fakhim Babak, Hassani Abolfazl, Rashidi Alimorad, and Ghodousi Parviz. Preparation and mechanical properties of graphene oxide: cement nanocomposites. *The Scientific World Journal*, 2014, 2014.

[68] Hae-Kyung Jeong, Yun Pyo Lee, Mei Hua Jin, Eun Sung Kim, Jung Jun Bae, and Young Hee Lee. Thermal stability of graphite oxide. *Chemical physics letters*, 470(4):255–258, 2009.

[69] Neil R Wilson, Priyanka A Pandey, Richard Beanland, Robert J Young, Ian A Kinloch, Lei Gong, Zheng Liu, Kazu Suenaga, Jonathan P Rourke, Stephen J York, et al. Graphene oxide: structural analysis and application as a highly transparent support for electron microscopy. *ACS nano*, 3(9):2547–2556, 2009.

[70] Isaac Childres, Luis A Jauregui, Wonjun Park, Helin Cao, and Yong P Chen. Raman spectroscopy of graphene and related materials. *Developments in photon and materials research*, pages 978–981, 2013.

[71] Andrea C Ferrari. Raman spectroscopy of graphene and graphite: disorder, electron–phonon coupling, doping and nonadiabatic effects. *Solid state communications*, 143(1):47–57, 2007.

[72] Weiwei Cai, Richard D Piner, Frank J Stadermann, Sungjin Park, Medhat A Shaibat, Yoshitaka Ishii, Dongxing Yang, Aruna Velamakanni, Sung Jin An, Meryl Stoller, et al. Synthesis and solid-state nmr structural characterization of 13c-labeled graphite oxide. *Science*, 321(5897):1815–1817, 2008.

[73] Abhijit Ganguly, Surbhi Sharma, Pagona Papakonstantinou, and Jeremy Hamilton. Probing the thermal deoxygenation of graphene oxide using high-resolution in situ x-ray-based spectroscopies. *The Journal of Physical Chemistry C*, 115(34):17009–17019, 2011.

[74] Tanesh Bansal, Aditya D Mohite, Hemant M Shah, Charudatta Galande, Anchal Srivastava, Jacek B Jasinski, Pulickel M Ajayan, and Bruce W Alphenaar. New insights into the density of states of graphene oxide using capacitive photocurrent spectroscopy. *Carbon*, 50(3):808–814, 2012.

[75] M Acik, G Lee, C Mattevi, M Chhowalla, K Cho, and YJ Chabal. Unusual infrared-absorption mechanism in thermally reduced graphene oxide. *Nature materials*, 9(10):840–845, 2010.

[76] Cristina Gómez-Navarro, R Thomas Weitz, Alexander M Bittner, Matteo Scolari, Alf Mews, Marko Burghard, and Klaus Kern. Electronic transport properties of individual chemically reduced graphene oxide sheets. *Nano letters*, 7(11):3499–3503, 2007.

[77] Kris Erickson, Rolf Erni, Zonghoon Lee, Nasim Alem, Will Gannett, and Alex Zettl. Determination of the local chemical structure of graphene oxide and reduced graphene oxide. *Advanced Materials*, 22(40):4467–4472, 2010.

[78] Da Chen, Hongbin Feng, and Jinghong Li. Graphene oxide: preparation, functionalization, and electrochemical applications. *Chemical reviews*, 112(11):6027–6053, 2012.

[79] Sasha Stankovich, Richard D Piner, Xinqi Chen, Nianqiang Wu, Son-Binh T Nguyen, and Rodney S Ruoff. Stable aqueous dispersions of graphitic nanoplatelets via the reduction of exfoliated graphite oxide in the presence of poly (sodium 4-styrenesulfonate). *Journal of Materials Chemistry*, 16(2):155–158, 2006.

[80] Owen C Compton, Dmitriy A Dikin, Karl W Putz, L Catherine Brinson, and SonBinh T Nguyen. Electrically conductive alkylated graphene paper via chemical reduction of amine-functionalized graphene oxide paper. *Advanced Materials*, 22(8):892–896, 2010.

[81] Jinhee Jang, Viet Hung Pham, Balasubramaniyan Rajagopalan, Seung Hyun Hur, and Jin Suk Chung. Effects of the alkylamine functionalization of graphene oxide on the properties of polystyrene nanocomposites. *Nanoscale research letters*, 9(1):1–6, 2014.

[82] Jintao Yang, Minjie Wu, Feng Chen, Zhengdong Fei, and Mingqiang Zhong. Preparation, characterization, and supercritical carbon dioxide foaming of polystyrene/graphene oxide composites. *The Journal of Supercritical Fluids*, 56(2):201–207, 2011.

[83] Horacio J Salavagione, Marian A Gomez, and Gerardo Martínez. Polymeric modification of graphene through esterification of graphite oxide and poly (vinyl alcohol). *Macromolecules*, 42(17):6331–6334, 2009.

[84] Fabienne Barroso-Bujans, Felix Fernandez-Alonso, Jose A Pomposo, Eduardo Enciso, Jose Luis G Fierro, and Juan Colmenero. Tunable uptake of poly (ethylene oxide) by graphite-oxide-based materials. *Carbon*, 50(14):5232–5241, 2012.

[85] Yeun-Jin Park, Sung Young Park, and Insik In. Preparation of water soluble graphene using polyethylene glycol: Comparison of covalent approach and noncovalent approach. *Journal of Industrial and Engineering Chemistry*, 17(2):298–303, 2011.

[86] Yan-Jun Wan, Long-Cheng Tang, Li-Xiu Gong, Dong Yan, Yi-Bao Li, Lian-Bin Wu, Jian-Xiong Jiang, and Guo-Qiao Lai. Grafting of epoxy chains onto graphene oxide for epoxy composites with improved mechanical and thermal properties. *Carbon*, 69:467–480, 2014.

[87] Kian Ping Loh, Qiaoliang Bao, Priscilla Kailian Ang, and Jiaxiang Yang. The chemistry of graphene. *Journal of Materials Chemistry*, 20(12):2277–2289, 2010.

[88] Bernhard Neises and Wolfgang Steglich. Simple method for the esterification of carboxylic acids. *Angewandte Chemie International Edition in English*, 17(7):522–524, 1978.

[89] http://www.organic-chemistry.org/namedreactions/steglich-esterification.shtm.

[90] Z. Pan, W. DUAN, D. Li, and F. Collins. Graphene oxide reinforced cement and concrete wo patent app. pct/au2012/001,582, July 4 2013. WO Patent App. PCT/AU2012/001,582.

[91] Shenghua Lv, Yujuan Ma, Chaochao Qiu, Ting Sun, Jingjing Liu, and Qingfang Zhou. Effect of graphene oxide nanosheets of microstructure and mechanical properties of cement composites. *Construction and building materials*, 49:121–127, 2013.

[92] Shenghua Lv, Jingjing Liu, Ting Sun, Yujuan Ma, and Qingfang Zhou. Effect of go nanosheets on shapes of cement hydration crystals and their formation process. *Construction and Building Materials*, 64:231–239, 2014.

[93] Uni en 196-1: Methods of testing cement. determination of mechanical strength., 2005.

[94] R Kostić, M Mirić, T Radić, M Radović, R Gajić, and ZV Popović. Optical characterization of graphene and highly oriented pyrolytic graphite. *Acta Physica Polonica A*, 116(4):718–721, 2009.

[95] Alexa Sadezky, Harald Muckenhuber, Hinrich Grothe, R Niessner, and Ulrich Pöschl. Raman microspectroscopy of soot and related carbonaceous materials: spectral analysis and structural information. *Carbon*, 43(8):1731–1742, 2005.

[96] George Socrates. *Infrared and Raman characteristic group frequencies: tables and charts*. John Wiley & Sons, 2004.